

University of Windsor

Scholarship at UWindor

Electronic Theses and Dissertations

Theses, Dissertations, and Major Papers

2010

Improving corrosion performance by surface patterning

Majid Karimi Bigdeli
University of Windsor

Follow this and additional works at: <https://scholar.uwindsor.ca/etd>

Recommended Citation

Bigdeli, Majid Karimi, "Improving corrosion performance by surface patterning" (2010). *Electronic Theses and Dissertations*. 8075.

<https://scholar.uwindsor.ca/etd/8075>

This online database contains the full-text of PhD dissertations and Masters' theses of University of Windsor students from 1954 forward. These documents are made available for personal study and research purposes only, in accordance with the Canadian Copyright Act and the Creative Commons license—CC BY-NC-ND (Attribution, Non-Commercial, No Derivative Works). Under this license, works must always be attributed to the copyright holder (original author), cannot be used for any commercial purposes, and may not be altered. Any other use would require the permission of the copyright holder. Students may inquire about withdrawing their dissertation and/or thesis from this database. For additional inquiries, please contact the repository administrator via email (scholarship@uwindsor.ca) or by telephone at 519-253-3000ext. 3208.

Improving corrosion performance by surface patterning

by
Majid Bigdeli Karimi

*A Thesis
Submitted to Faculty of Graduate Studies
through Materials Engineering
in partial fulfilment of the requirements for
the degree of Master of Applied Science at the
University of Windsor*

*Windsor, Ontario, Canada
2010
© 2010 Majid Bigdeli Karimi*



Library and Archives
Canada

Published Heritage
Branch

395 Wellington Street
Ottawa ON K1A 0N4
Canada

Bibliothèque et
Archives Canada

Direction du
Patrimoine de l'édition

395, rue Wellington
Ottawa ON K1A 0N4
Canada

Your file *Votre référence*
ISBN: 978-0-494-80229-8
Our file *Notre référence*
ISBN: 978-0-494-80229-8

NOTICE:

The author has granted a non-exclusive license allowing Library and Archives Canada to reproduce, publish, archive, preserve, conserve, communicate to the public by telecommunication or on the Internet, loan, distribute and sell theses worldwide, for commercial or non-commercial purposes, in microform, paper, electronic and/or any other formats.

The author retains copyright ownership and moral rights in this thesis. Neither the thesis nor substantial extracts from it may be printed or otherwise reproduced without the author's permission.

AVIS:

L'auteur a accordé une licence non exclusive permettant à la Bibliothèque et Archives Canada de reproduire, publier, archiver, sauvegarder, conserver, transmettre au public par télécommunication ou par l'Internet, prêter, distribuer et vendre des thèses partout dans le monde, à des fins commerciales ou autres, sur support microforme, papier, électronique et/ou autres formats.

L'auteur conserve la propriété du droit d'auteur et des droits moraux qui protègent cette thèse. Ni la thèse ni des extraits substantiels de celle-ci ne doivent être imprimés ou autrement reproduits sans son autorisation.

In compliance with the Canadian Privacy Act some supporting forms may have been removed from this thesis.

While these forms may be included in the document page count, their removal does not represent any loss of content from the thesis.

Conformément à la loi canadienne sur la protection de la vie privée, quelques formulaires secondaires ont été enlevés de cette thèse.

Bien que ces formulaires aient inclus dans la pagination, il n'y aura aucun contenu manquant.


Canada

Declaration of Co-Authorship

I hereby declare that this thesis incorporates material that is a result of joint research under the supervision of professors Vesselin Stoilov and Derek O. Northwood. The research collaboration is covered in Chapters 3, 4 and 5 of the thesis. In all cases, the key ideas, primary contributions, experimental designs, data analysis and interpretation, were performed by the author, and the contributions of the co-authors was primarily in the capacity of supervision of the research in the form of technical advice and suggestions.

I am aware of the University of Windsor Senate Policy on Authorship and I certify that I have properly acknowledged the contribution of other researchers to my thesis, and have obtained written permission from each of the co-author(s) to include the above material(s) in my thesis.

I certify that, with the above qualification, this thesis, and the research to which it refers, is the product of my own work.

Author's Declaration of Originality

I hereby certify that I am the sole author of this thesis and that no part of this thesis has been published or submitted for publication. I certify that, to the best of my knowledge, my thesis does not infringe upon anyone's copyright nor violate any proprietary rights and that any ideas, techniques, quotations, or any other material from the work of other people included in my thesis, published or otherwise, are fully acknowledged in accordance with the standard referencing practices.

Furthermore, to the extent that I have included copyrighted material that surpasses the bounds of fair dealing within the meaning of the Canada Copyright Act, I certify that I have obtained a written permission from the copyright owner(s) to include such material(s) in my thesis and have included copies of such copyright clearances to my appendix. I declare that this is a true copy of my thesis, including any final revisions, as approved by my thesis committee and the Graduate Studies office, and that this thesis has not been submitted for a higher degree to any other University or Institution.

Abstract

In this research, the effect of surface patterning on the corrosion behaviour of a metal (nickel) was investigated. The idea originates from the fact that hydrophobic (low or non wettable) surfaces can decrease the contact area between a corrosive solution and a surface. In the current work, special surface patterns were created on pure nickel sheets. The corrosion behaviour of those surfaces was studied using a dynamic polarization method in 0.5M H₂SO₄. It was found that there is a trend or dependency between the hole size (D), the hole distance (L), and the corrosion current density (I_{corr}). The higher the (D/L)² ratio, the higher the corrosion current density (I_{corr}). The corrosion potential (E_{corr}) of all samples was lower than that of the reference sample in all the tests. SEM images showed that after the first corrosion test some local corroded regions were created on the surfaces but in the samples with the lowest I_{corr} there was a slight change in the surface.

To My Lovely Family

*Mehdi,
Narges,
Saeed*

Acknowledgement

First, I am heartily thankful to my thesis advisors Dr. Vesselin Stoilov and Dr. Derek O. Northwood for their thoughtful supervision, encouragement, and consistent support in my study period. It was a great pleasure in my academic life to have their guidance and attention and my study has been challenging and productive.

In addition, I would like to express my sincere gratitude to my committee members Dr. Daniel Green, Dr. David Ting and Dr. Henry Hu for their invaluable comments and time.

I warmly thank to Dr. X. Nie and Dr. A. Alpas for their kindness in granting permission to use the corrosion test equipment and profilometry instrument, respectively. Also, I appreciate the assistance of engineering technologists: Mr. John Robinson for all technical assistance in the different laboratories, and Mr. Andy Jenner and Mr. Matt St. Louis for their assistance in sample preparation for this research.

Table of contents

Declaration of Co-Authorship	iii
Author's Declaration of Originality	iii
Abstract	iv
Dedication	v
Acknowledgements	vi
List of Tables	ix
List of Figures	x
Chapter 1: Introduction	1
Chapter 2: Literature review	4
2.1. <i>Effect of surface roughness on corrosion behavior</i>	4
2.1.1. <i>Surface roughness of steels</i>	4
2.1.2. <i>Relationship between surface roughness and pitting corrosion</i>	7
2.1.3. <i>Surface roughness of coatings</i>	9
2.2. <i>Hydrophobicity: concepts, properties and applications</i>	11
2.2.1. <i>Hydrophobicity of metals</i>	14
2.2.1.1. <i>Hydrophobic surfaces on steel</i>	15
2.2.1.2. <i>Hydrophobic surfaces on nickel</i>	17
2.2.1.3. <i>Hydrophobic surfaces on copper</i>	19
2.2.1.4. <i>Hydrophobic surfaces on aluminum</i>	22
2.2.1.5. <i>Hydrophobic surfaces on other materials</i>	25
2.3. <i>Laser surface patterning</i>	27
2.3.1. <i>Laser interface metallurgy method</i>	28
2.3.2. <i>Laser patterning on stainless steel</i>	30
2.3.3. <i>Laser operations on different materials</i>	31
Chapter 3: Experimental procedures	33
3.1. <i>Material</i>	33
3.2. <i>Specimen preparation</i>	33
3.3. <i>Laser ablation</i>	34
3.4. <i>Scanning electron microscopy (SEM) and EDS analysis</i>	35

3.5. Profilometry test	36
3.6. Corrosion tests	36
3.7. X-ray diffraction (XRD)	38
Chapter 4: Results and discussion	39
4.1. SEM images of the patterned samples	39
4.2. EDS analysis of the patterned samples	44
4.3. Roughness of the patterned samples	46
4.4. Corrosion tests	53
4.5. SEM images after corrosion tests	72
4.6. Roughness data after corrosion tests	82
4.7. EDS after the first corrosion test	89
Chapter 5: Conclusions and recommendations	91
5.1. Conclusions	91
5.2. Recommendations	92
References	93
VITAE AUCTORIS	99

List of Tables

Chapter 2: Literature review

<i>Table 2-1. Pitting potentials after various surface treatments [26]</i>	5
--	---

Chapter 3: Experimental procedures

<i>Table 3-1. The hole sizes and their distances of the textures created on the nickel sheet surfaces</i>	35
---	----

<i>Table 3-2. Sample coding system</i>	35
--	----

Chapter 4: Results and discussions

<i>Table 4-1. The roughness values from profilometry test for all samples</i>	47
---	----

<i>Table 4-2. The corrosion data for all samples after the first test</i>	57
---	----

<i>Table 4-3. The corrosion data for all samples after the second test</i>	57
--	----

<i>Table 4-4. The corrosion data for all samples after the third test</i>	57
---	----

<i>Table 4-5. Dependence of I_{corr} of all samples and different parameters</i>	66
---	----

<i>Table 4-6. Dependence of E_{corr} of all samples and different parameters</i>	66
---	----

<i>Table 4-7. The roughness value obtained from profilometry for some corroded samples</i>	83
--	----

List of Figures

Chapter 2: Literature review

- Fig. 2-1. Dependence of pitting potential of the 316LVM surface on the surface roughness; the modified sample went through CCP method [24]. 5
- Fig. 2-2. Anodic polarization curves of smooth and rough steel substrates (AISI 4340), α -Ta coatings deposited on these substrates and of Ta foil, in 0.5 M H_2SO_4 deaerated with N_2 at room temperature [27]. 6
- Fig. 2-3. Potentiodynamic polarization curves for HNS in aerated 0.05M H_2SO_4 + 0.5M NaCl solution at ambient temperature with different surface roughness [25]. 7
- Fig. 2-4. The pitting potential, E_p , of 304L stainless steel measured in 0.6 M NaCl as a function of the surface finish [1]. 8
- Fig. 2-5. (a) Potentiodynamic polarisation behavior of the specimens PEO coated at different current densities for 15 min (test electrolyte: 0.1 M NaCl solution), (b) average thickness and roughness of the specimens PEO coated at different current densities for 15 min [31]. 9
- Fig. 2-6. Potentiodynamic polarization curves obtained in the 3.5% NaCl solution at a scanning rate of 1 mV/s: the oxide coating with roughness of (a) 1.6 μm ; (b) 4.2 μm ; and (c) 6.3 μm [32]. 10
- Fig. 2-7. Polarization curves of various Ti–Si–N coatings tested in 3.5 wt% NaCl solution [33]. 10
- Fig. 2-8. SEM images of the surface of a lotus leaf [8]. 11
- Fig. 2-9. The schematic illustration of surface tensions on a solid surface in contact with a water droplet, where γ_{sv} is the solid–vapor surface energy, γ_{sl} is the solid–liquid interfacial energy and γ_{lv} is the liquid–vapor surface energy. 13
- Fig. 2-10. (a) Photo of water droplets on the phosphating film and superhydrophobic film, (b) SEM image of the superhydrophobic film which was fabricated by silicon sol [21]. 15
- Fig. 2-11. Top (left), side (308) (middle) and profile view (right) SEM micrographs of AISI 316L type austenitic stainless steel-based [12]. 16
- Fig. 2-12. Schematic illustration of laser–induced periodic surface structure (LIPSS) covered with nanoparticles formed at fluences 0.08 J/cm². (a) The alternating array of LIPSS and nanoparticles. (b) The local interaction of the sort water interface with the top of LIPSS [12]. 16
- Fig. 2-13. Surface and microstructure of Ni; SEM images: (a) left, overview, (b) middle, pentagon, (c) right, pore [39]. 17
- Fig. 2-14. Fabricated nickel micromesh sheet: (a) photograph of a nickel micromesh prototype unit, (b) & (c) magnified SEM images of the micromesh [8]. 18
- Fig. 2-15. A PFPE solution treatment of the surface created a nanotextured layer on the “Ni crowns” [4]. 18

<i>Fig. 2-16. Wetting of an acid-activated nickel surface by water after treatment with Betatec gold post-dip, $\theta=92^\circ$ [38].</i>	19
<i>Fig. 2-17. SEM images of the formation of the superhydrophobic metal surface and an image of a water drop on this surface: (a) the as-deposited copper surface; (b) High magnification image of the copper surface after electrochemical reaction with sulfur gas at 150°C for 10 min; (c) Low magnification image of (b); (d) Schematic diagram of the formation of the micro- and nanostructured metal surface; (e) Optical image of a water drop on the surface in (b) [9].</i>	20
<i>Fig. 2-18. SEM images of the copper surfaces with different produced at different current densities: (a) current density = 0.04 A/cm^2, contact angle = 125°. (b) Current density = 0.08 A/cm^2, Contact angle = 153.5° (c) Enlarged SEM image on surface b. (d) Current density = 0.10 A/cm^2, Contact angle = 132.5° [41].</i>	21
<i>Fig. 2-19. Model of the interface between super-hydrophobic surface and sterile seawater [13].</i>	21
<i>Fig. 2-20. FE-SEM images of the textured aluminum sheet: (a) top view and (b) tilted view. The scale bar is $1\ \mu\text{m}$ [20].</i>	22
<i>Fig. 2-21. The change in thickness of the aluminum layer versus time for samples protected by films of varying contact angle and a sample with only native Al_2O_3 layer (without protective film) [15].</i>	23
<i>Fig. 2-22. Potentiodynamic polarization curves of untreated, anodized and superhydrophobic samples for 34 h in sterile seawater at 2mVs^{-1} [7].</i>	24
<i>Fig. 2-23. SEM images of (a) the untreated aluminum and (b) the superhydrophobic aluminum surfaces [17].</i>	24
<i>Fig. 2-24. A schematic of a rough surface immersed in seawater [18].</i>	25
<i>Fig. 2-25. (a) Typical SEM images of the laser-etched PDMS surface with the convex width of about 25 μm, showing the regular arrays of microconvexes; (b) magnified image of (a), showing the submicro structures on each convex; (c) high-resolution image of a single convex of (b), showing the nanoparticles composed of each submicro block; (d) high resolution image of a single convex with width of about 50 μm (left) and a flat PDMS surface (right) [10].</i>	27
<i>Fig. 2-26. Scanning electron micrographs of the structured surfaces irradiated with low and high laser intensities. Line-like structures: low (a) and (b) high laser fluence; Dot-like structures: low (c) and (d) high laser fluence; Cross-like structures: low (e) and (g) high laser fluence. Tilt: 52° [49].</i>	29
<i>Fig. 2-27. SEM micrographs of three laser beams irradiated stainless steel substrates (period = 8.00 mm): (a) 2.15 J/cm^2; (b) 2.41 J/cm^2. The insert in (a) shows the three laser beams configuration and the calculated interference pattern. Tilt: 52° [50].</i>	30
<i>Fig. 2-28. SEM images (view tilt 30°) of the surface at incident beam angles of (a) 75°, (b) 60°, and (c) 45° using the following parameters: Laser wavelength 1064 nm, intensity 0.43 GW/cm^2, and 5000 pulses/spot [54].</i>	30
<i>Fig. 2-29. Structure induced in a steel surface [52].</i>	31

Fig. 2-30. SEM image of the micro-raster structure; b Side view of micro-raster structure [19]. 32

Chapter 3: Experimental procedure

Fig. 3-1. Flowchart of experimental procedures. 33

Fig. 3-2. (a) Diamond suspension and (b) alumina powder water suspension polishing machines. 34

Fig. 3-3. 34

Fig. 3-4. Schematic presentation of the proposed surface texture model; D assigns to the hole diameter and L assigns to the distance between the holes. The gray area is the laser ablated region. 36

Fig. 3-5. JEOL 5800 scanning electron microscope. 36

Fig. 3-6. The Wyko NT1100 profilometry machine. 37

Chapter 4: Results and discussions

Fig. 4-1. The SEM micrographs of the initial smooth sample after final polishing with 0.05 μm -alumina particles suspension. 40

Fig. 4-2. The SEM micrographs of samples (a) and (b) D5L5; (c) and (d) D5L10; (e) and (f) D5L20 after laser ablation process. 41

Fig. 4-3. The SEM micrographs of samples (a) and (b) D10L10; (c) and (d) D10L20; (e) and (f) D10L30 after laser ablation process. 42

Fig. 4-4. The SEM micrographs of samples (a) and (b) D20L20; (c) and (d) D20L30; (e) and (f) D20L40 after laser ablation process. 43

Fig. 4-5. EDS analysis spectra of samples (a) REF, (b) D5L5; surface, (c) D5L20; surface, (d) D5L20; hole, and (e) D20L40; surface (continued). 44

Fig. 4-6. Sample D5L5 (a) 3D roughness, (b) X-profile, (c) Y-profile and (d) histogram curve. 48

Fig. 4-7. Sample D5L20 (a) 3D roughness, (b) X-profile, (c) Y-profile and (d) histogram curve. 49

Fig. 4-8. Sample D10L20 (a) 3D roughness, (b) X-profile, (c) Y-profile and (d) histogram curve. 50

Fig. 4-9. Sample D20L20 (a) 3D roughness, (b) X-profile, (c) Y-profile and (d) histogram curve. 51

Fig. 4-10. Sample D20L40 (a) 3D roughness, (b) X-profile, (c) Y-profile and (d) histogram curve. 52

Fig. 4-11. Potentiodynamic corrosion curves for sample REF in 0.5M H_2SO_4 . 58

Fig. 4-12. Potentiodynamic corrosion curves for sample D5L5 in 0.5M H ₂ SO ₄ after different tests.	58
Fig. 4-13. Potentiodynamic corrosion curves for sample D5L10 in 0.5M H ₂ SO ₄ after different tests.	59
Fig. 4-14. Potentiodynamic corrosion curves for sample D5L20 in 0.5M H ₂ SO ₄ after different tests.	59
Fig. 4-15. Potentiodynamic corrosion curves for sample D10L10 in 0.5M H ₂ SO ₄ after different tests.	60
Fig. 4-16. Potentiodynamic corrosion curves for sample D10L20 in 0.5M H ₂ SO ₄ after different tests.	60
Fig. 4-17. Potentiodynamic corrosion curves for sample D10L30 in 0.5M H ₂ SO ₄ after different tests.	61
Fig. 4-18. Potentiodynamic corrosion curves for sample D20L20 in 0.5M H ₂ SO ₄ after different tests.	61
Fig. 4-19. Potentiodynamic corrosion curves for sample D20L30 in 0.5M H ₂ SO ₄ after different tests.	62
Fig. 4-20. Potentiodynamic corrosion curves for sample D20L40 in 0.5M H ₂ SO ₄ after different tests.	62
Fig. 4-21. Corrosion data of sample D5L5 (a) I _{corr} and R _p curves, (b) E _{corr} curve.	63
Fig. 4-22. Corrosion data of sample D5L20 (a) I _{corr} and R _p curves, (b) E _{corr} curve.	63
Fig. 4-23. Corrosion data of sample D20L40 (a) I _{corr} and R _p curves, (b) E _{corr} curve.	63
Fig. 4-24. The I _{corr} values versus hole diameters (D) for all samples with $(\frac{D}{L})^2 = 1$ and sample REF (D/L)=0 after the first corrosion test.	67
Fig. 4-25. The I _{corr} values versus hole diameters (D) for all samples with $(\frac{D}{L})^2 = 0.25$ and sample REF (D/L)=0 after the first corrosion test.	67
Fig. 4-26. The E _{corr} values versus hole diameters (D) for all samples with $(\frac{D}{L})^2 =$ and sample REF (D/L)=0 after the first corrosion test.	67
Fig. 4-27. The E _{corr} values versus hole diameters (D) for all samples with $(\frac{D}{L})^2 = 0.25$ and sample REF.	68
Fig. 4-28. I _{corr} values for all samples versus roughness.	69
Fig. 4-29. I _{corr} values for all samples versus roughness.	69
Fig. 4-30. The SEM micrographs of sample REF after the first corrosion test.	72

<i>Fig. 4-31. The SEM micrographs of sample D5L5 after: (a) and (b) the first; (c) and (d) the second; (e) and (f) the third corrosion tests in 0.5M H₂SO₄.</i>	73
<i>Fig. 4-32. The SEM micrographs of sample D5L10 after: (a) and (b) the first; (c) and (d) the second; (e) and (f) the third corrosion tests in 0.5M H₂SO₄.</i>	74
<i>Fig. 4-33. The SEM micrographs of sample D5L20 after: (a) and (b) the first; (c) and (d) the second; (e) and (f) the third corrosion tests in 0.5M H₂SO₄.</i>	75
<i>Fig. 4-34. The SEM micrographs of sample D10L10 after: (a) and (b) the first; (c) and (d) the second; (e) and (f) the third corrosion tests in 0.5M H₂SO₄.</i>	76
<i>Fig. 4-35. The SEM micrographs of sample D10L20 after: (a) and (b) the first; (c) and (d) the second; (e) and (f) the third corrosion tests in 0.5M H₂SO₄.</i>	77
<i>Fig. 4-36. The SEM micrographs of sample D10L30 after: (a) and (b) the first; (c) and (d) the second; (e) and (f) the third corrosion tests in 0.5M H₂SO₄.</i>	78
<i>Fig. 4-37. The SEM micrographs of sample D20L20 after: (a) and (b) the first; (c) and (d) the second; (e) and (f) the third corrosion tests in 0.5M H₂SO₄.</i>	79
<i>Fig. 4-38. The SEM micrographs of sample D20L30 after: (a) and (b) the first; (c) and (d) the second; (e) and (f) the third corrosion tests in 0.5M H₂SO₄.</i>	80
<i>Fig. 4-39. The SEM micrographs of sample D20L40 after: (a) and (b) the first; (c) and (d) the second; (e) and (f) the third corrosion tests in 0.5M H₂SO₄.</i>	81
<i>Fig. 4-40. Sample D5L5 (a) 3D roughness, (b) X-profile, (c) Y-profile and (d) histogram curve after the second corrosion test.</i>	84
<i>Fig. 4-41. Sample D5L20 (a) 3D roughness, (b) X-profile, (c) Y-profile and (d) histogram curve after the second corrosion test.</i>	85
<i>Fig. 4-42. Sample D10L20 (a) 3D roughness, (b) X-profile, (c) Y-profile and (d) histogram curve after the second corrosion test.</i>	86
<i>Fig. 4-43. Sample D20L20 (a) 3D roughness, (b) X-profile, (c) Y-profile and (d) histogram curve after the second corrosion test.</i>	87
<i>Fig. 4-44. Sample D20L40 (a) 3D roughness, (b) X-profile, (c) Y-profile and (d) histogram curve after the second corrosion test.</i>	88
<i>Fig. 4-45. EDS analysis spectra of samples (a) REF, (b) D5L20; surface, (c) D5L20; pit, (d) D20L40; surface, and (e) D20L40; hole (continued).</i>	89

List of Abbreviations

BTESPT	<i>bis-[triethoxysilylpropyl] tetrasulfide</i>
CPP	<i>cyclic potentiodynamic passivation</i>
E_{corr}	<i>corrosion potential</i>
EDM	<i>electrical discharge machining</i>
EDS	<i>energy dispersive spectroscopy</i>
E_m	<i>pit potential</i>
EWf	<i>electron work function</i>
FAS	<i>fluoroalkylsilane</i>
GTM	<i>golf-tee shaped micropillar</i>
HNS	<i>high nitrogen bearing stainless steel</i>
I_{corr}, i_{corr}	<i>corrosion current density</i>
LIST	<i>laser interference surface treatment</i>
MEMS	<i>micro-electro-mechanical systems</i>
MIC	<i>microbially influenced corrosion</i>
OCP	<i>open circuit potential</i>
PDMS	<i>polydimethylsiloxane</i>
PEI	<i>polyethyleneimine</i>
PEM	<i>proton exchange membrane</i>
PEO	<i>plasma electrolytic oxidation</i>
PPFC	<i>plasma polymerized fluorocarbon coating</i>
SAM	<i>self-assembled monolayers</i>
SCE	<i>standard calomel electrode</i>
SEM	<i>scanning electron microscopy</i>
SLM	<i>selected laser melting</i>
XRD	<i>X-ray diffraction</i>

1. Introduction

The corrosion resistance is one of the important properties of metals and their alloys. In many applications metallic structures are in contact with corrosive media and failure can occur in relatively short times. Hence, improving the corrosion resistance of metallic alloys can be of paramount importance.

Surface roughness of materials especially metals affects their corrosion resistance. The pitting potential, which is the minimum potential at which stable pits are observed to propagate, is lower for rougher surfaces [1,2] than for smoother ones. Pits initiate at specific sites on the surface (usually inclusions) and rougher surfaces generally provide sites with a more occluded geometry. It is easier to maintain a concentrated local chemistry at these occluded sites, and so rougher surfaces tend to support a higher frequency of pit initiation [3]. Although it has been found that a higher surface roughness can decrease the corrosion resistance, in some applications having special surface pattern (topography or geometry) can be useful. It has been found that hydrophobic surfaces are useful in applications involving wear, self cleaning, and corrosion [4-7].

Many terrestrial plants and animals are water-repellent due to hydrophobic surface components with microscopic roughness. It has been shown that these surfaces provide a very effective anti-adhesive property against particulate contamination. This self-cleaning mechanism, called the "Lotus-Effect", is an important function of many microstructured biological surfaces [5]. The surface of the lotus leaf is covered with micro-protrusions, which are themselves covered nano-protrusions. The nano-protrusions are composed of epicuticular wax crystalloids that are hydrophobic [8].

The unusual wetting characteristics of superhydrophobic surfaces are governed by both their surface chemical composition and surface geometric microstructure [9,10]; their wettability can be decreased by creating a local geometry with a large geometric area relative to the projected area [9]. The origin of the self-cleaning property of lotus leaves has been revealed to be a cooperative effect of micro- and nano-scale structures on their surfaces [10].

Many methods have recently been developed to fabricate surfaces with controlled roughness through various approaches such as the sol–gel process, generation of a fibrillar structure, creation of a rough surface covered with low surface energy molecules, and the phase separation of a polymer in a mixed solvent system, etc [9]. “Etch and coat” methods are potentially useful for large scale production of superhydrophobic surfaces on metals. Despite the diversity of approaches, which have been applied to creating superhydrophobic metal surfaces there are just two factors which dominate the overall performance. One is the roughness or texture of the surface, the second is the nature of the surface modifying layer [11]. It is said that the fraction of air between the water droplet and the double-scale (patterned) surface is the important reason of superhydrophobicity of the surface [12].

Some studies have shown that creation of hydrophobic surfaces on such metals as aluminum and copper can increase the corrosion resistance in different corrosive media [7, 13-18].

A surface with a rough structure can be fabricated by many techniques, such as chemical vapor deposition, anodization, soft etching, and optical lithography. The laser fabrication technique provides an effective tool to fabricate periodic structures on any material surface due to its ultrahigh peak power [19]. Some hydrophobic surfaces have been created on different metals and alloys such as stainless steel, nickel, aluminum, copper and etc [4,9,20,21]. In all of these studies, hydrophobicity was achieved using a roughness on a surface along with a material to decrease surface energy. However, some new research [22,23] has shown that it is possible to create hydrophobic properties on a surface whether it is naturally hydrophilic or hydrophobic.

In this research nickel was selected as model metal because no work had been done on surface patterning of this metal thus far. The aim of this work was to create special surface patterns (topography) on a pure nickel surface and study the corrosion behavior of the patterned surfaces. In fact in this research the novelty was first to select pure nickel and second to create a hydrophobic surface using laser ablation method on pure nickel sheet without using any materials to

decrease the surface energy. In other words, it was targeted to fabricate a hydrophobic surface solely by surface patterning or topography.

2. Literature review

This review covers four general topics, namely: effect of surface roughness on corrosion behavior; hydrophobicity; laser surface patterning and polymer exchange membrane fuel cells. In each section, the relevant research is summarized to provide a background for the current research.

2.1. Effect of surface roughness on corrosion behavior

Several researchers have investigated the effect of surface roughness on the corrosion behavior of steels. These have induced studies on surface roughness on cyclic potentiodynamic passivation [24], electrochemical behavior [25] and the effect of surface roughness on pitting corrosion resistance [26].

2.1.1. Surface roughness of steels

The influence of surface roughness on the efficiency of a cyclic potentiodynamic passivation (CPP) method on stainless steel was investigated by Shahryari and his colleagues [24]. They showed that a decrease in surface roughness of stainless steel 316LVM on which a passive film is naturally formed, results in an increase in the alloy's resistance to pitting corrosion. However for the surface on which the passive film is formed using the CPP method, an increase in both general and pitting corrosion resistance was observed. It was also demonstrated that the CPP method is highly effective in increasing the general and pitting corrosion resistance of 316LVM in the entire surface roughness range, thus further supporting its potential use in a wide range of biomedical and industrial applications. Fig. 2-1 shows the E_{pit} as a function of surface roughness for the 316LVM stainless steel.

Girija and his collaborators [26] studied the effect of mechanical and chemical treatments of the surface on the pitting corrosion resistance of type 316LN stainless steel in 0.5M sodium chloride (NaCl) solution. When the surface roughness is greater, it is more likely that an electrochemically active inclusion is associated with a concavity in the surface that is deep enough to support pit initiation by generation of the diffusion barrier (the depression which acts as a

barrier to diffusion of dissolved corrosion products, protons and ions from the pit site). When the surface roughness is lower, the inclusions can not act as pit sites because their depression into the surface is not great enough to provide a sufficient diffusion barrier. Anyhow, they found that surface roughness has no significant effect on the pitting potentials after chemical treatment. Table 2-1 presents the Grijja's results for pitting potentials in different conditions.

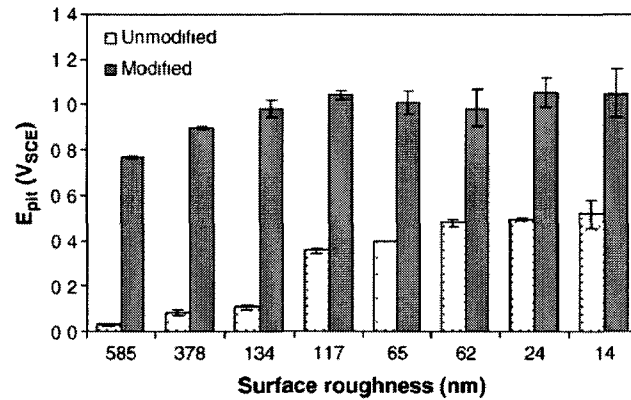


Fig 2-1. Dependence of pitting potential of the 316LVM surface on the surface roughness; the modified sample went through CCP method [24]

Table 2-1. Pitting potentials after various surface treatments [26]

Surface finish method	Surface Roughness (μm)	Mechanical treatment	Pickling	Pickling followed by passivation
Diamond cloth finish	0.009	394 mV	672 mV	1114 mV
600 grit SiC abrasive polishing	0.05	326 mV	651 mV	1040 mV
320 grit SiC abrasive polishing	0.07	307 mV	637 mV	1000 mV
Lathe finish	0.5	152 mV	631 mV	865 mV

In another research [27], deposited α -Ta coatings on smooth and rough AISI 4340 steel substrates were studied in terms of porosity and corrosion behavior.

Maeng et al.'s research objective was to study the corrosion behavior of the coatings deposited on smooth and rough steel surfaces. The coatings deposited on both substrates showed almost identical anodic polarization behavior although the corrosion current density was slightly higher in the case of the coating on the rough substrate. Fig. 2-2 shows the potentiodynamic corrosion curves for those coated and uncoated surfaces.

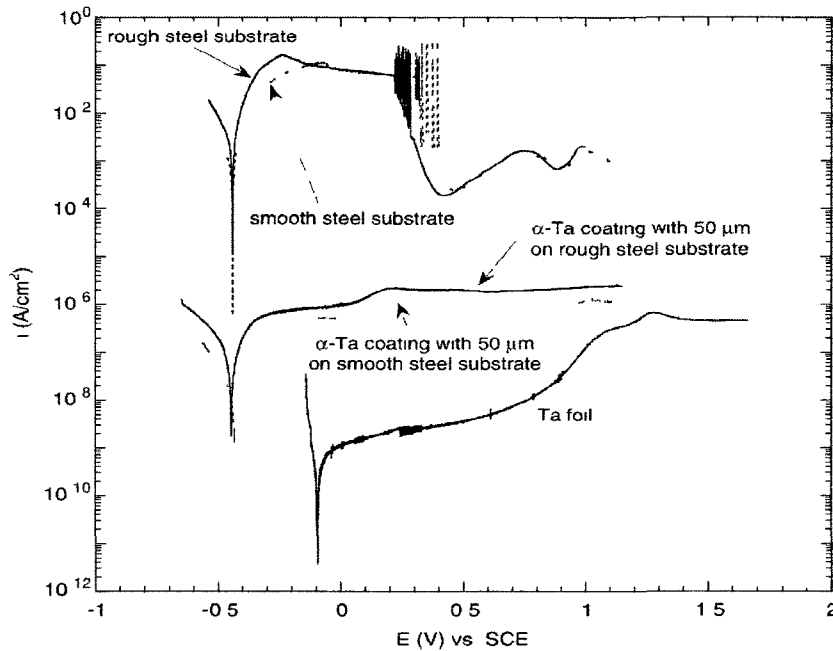


Fig 2-2 Anodic polarization curves of smooth and rough steel substrates (AISI 4340), α -Ta coatings deposited on these substrates and of Ta foil, in 0.5 M H_2SO_4 deaerated with N_2 at room temperature [27]

The effects of oxygen, H_2SO_4 concentration and surface roughness on the electrochemical behavior of high nitrogen bearing stainless steel (HNS) in 0.05 H_2SO_4 + 0.5M NaCl solution was studied by Qiao and his co-workers [25]. They observed three corrosion potentials (active, active-passive and passive regions) in the potentiodynamic polarization curve which is probably due to hydrogen evolution reaction and even generation of metal cations [28]. The surface roughness has no noticeable effect on the number of corrosion potential but increases the values of the corrosion potentials and passivation current densities with increase in the surface roughness (Fig. 2-3). The surface roughness has no evident effects on the cathodic process but acceleration of the anodic corrosion

rate with increased surface roughness could be assumed to be due to the reduction in the average electron work function (EWF) with surface roughness [25].

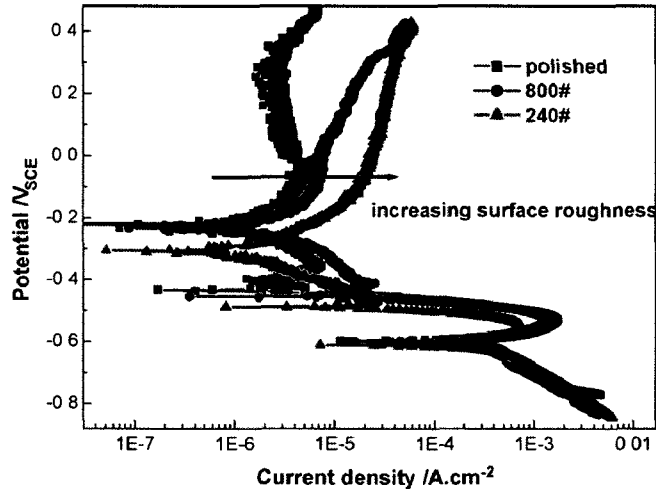


Fig. 2-3. Potentiodynamic polarization curves for HNS in aerated 0.05M H_2SO_4 + 0.5M NaCl solution at ambient temperature with different surface roughness [25].

Celik et al. researched the corrosion behavior of grit-blasted AISI 304L stainless steel substrates coated with Al_2O_3 in 1 N H_2SO_4 solution. The results showed that the corrosion resistance of plasma-sprayed coatings is reduced with increasing surface roughness [29].

2.1.2. Relationship between surface roughness and pitting corrosion

Some works have examined the role of surface roughness in pitting corrosion. The pitting potential, which is the minimum potential at which stable pits are observed to propagate, is lower for rougher surfaces [1,2] than for smoother ones, a phenomenon which is in qualitative agreement with the known diffusion control of the rate of metastable and stable pit propagation [1]. Pits initiate at specific sites on the surface (usually inclusions) and rougher surfaces generally provide sites with a more occluded geometry. It is easier to maintain a concentrated local chemistry at these occluded sites, and so rougher surfaces tend to support a higher frequency of pit initiation [3]. A smoother surface shows

a smaller frequency of metastable pitting in comparison with a rougher one. The surface with the smoother finish, however, also shows a far higher frequency of nucleation events. This apparently paradoxical phenomenon is attributed to the repetitive nucleation of pits from individual sites of pitting [30]. The potential (E_m) at which the metastable pit or pits start to grow on the surface depends on surface roughness.

The nucleation of corrosion pits on stainless steel was researched by Burstein and Vines [30] in chloride solution at constant potential through observation of minute current transients. The nucleation of pits is a process that is apparently random in time, and its frequency of occurrence decays with time at constant potential with first-order kinetics. The time-constant associated with this is a function of the surface finish and reflects the ability of nucleated sites to propagate as metastable pits or to repassivate. A smoother surface finish makes propagation more difficult and allows more repetitive nucleations from the same site. In another work, Sasaki and Burstein [1] focused on the effect of created surface roughnesses on the pitting potential during slurry erosion-corrosion in 304L stainless steel. Their results confirm that surface roughness is a critical parameter in determining the pitting potential of 304L stainless steel. The pitting potential is easily changed by several tenths of a volt by appropriate surface roughening. For surfaces finished by grinding on silicon carbide paper, the pitting potential falls linearly with increase in the reciprocal grit number (Fig. 2-4), implying a linear relationship with the particle size.

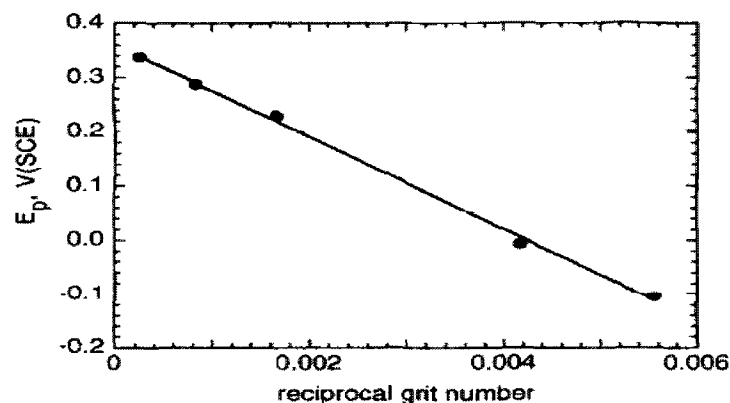


Fig. 2-4. The pitting potential, E_p , of 304L stainless steel measured in 0.6 M NaCl as a function of the surface finish [1].

2.1.3. Surface roughness of coatings

Srinivasan and his collaborators produced some coatings on AM50 magnesium alloy using plasma electrolytic oxidation (PEO) in a silicate-based electrolyte using a DC power source. The anti-corrosion ability of an oxide coating on AZ91D alloy is decreased with the increasing porosity. The results reveal that the roughness level of the coatings increase with increase in current density for a given processing duration and corrosion resistance decreases as well. Thus, the thicker (more porosity) and rougher the coating, the higher the corrosion (See Fig. 2-5) [31].

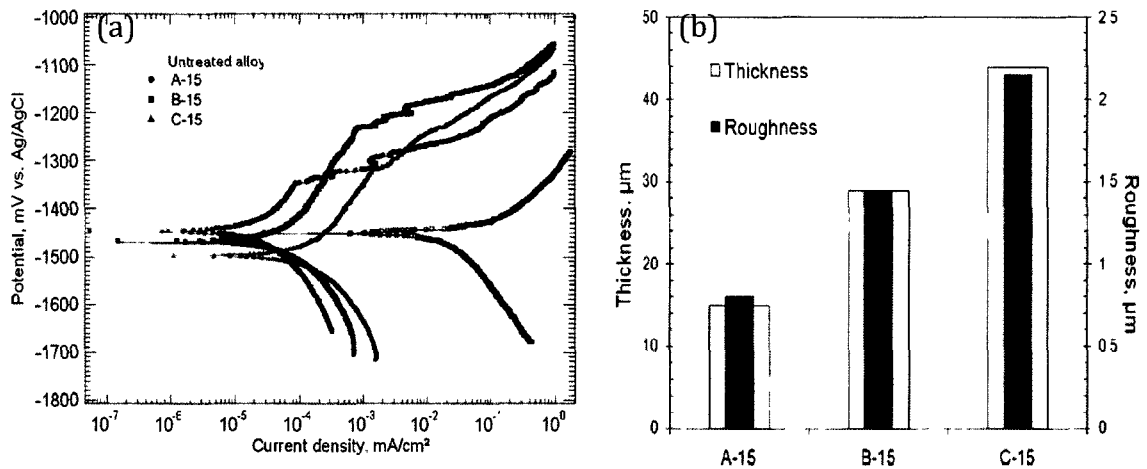


Fig. 2-5. (a) Potentiodynamic polarisation behavior of the specimens PEO coated at different current densities for 15 min (test electrolyte: 0.1 M NaCl solution), (b) average thickness and roughness of the specimens PEO coated at different current densities for 15 min. [31].

Fig. 2-6 shows the potentiodynamic corrosion curve of some coatings with different roughnesses. Bai's research [32] confirms that an oxide coating (on AZ91D Mg alloy) with the minimum roughness value, exhibits the maximum corrosion resistance. Bai contends that the roughness (proportional to porosity) value of an oxide coating is the predominant factor promoting the anti-corrosion ability. Thus, the corrosion resistance of an oxide coating has a dependency to the roughness of the coating. On the other hand, the dense oxide coating with less porosity could show a better corrosion resistance.

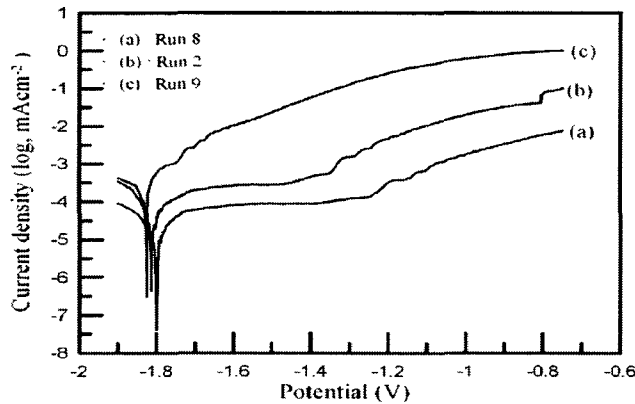


Fig. 2-6. Potentiodynamic polarization curves obtained in the 3.5% NaCl solution at a scanning rate of 1 mV/s: the oxide coating with roughness of (a) 1.6 μm ; (b) 4.2 μm ; and (c) 6.3 μm [32].

Chang et al. [33] deposited a nano-composite Ti-Si-N films on tungsten carbide substrates by a filtered cathodic arc deposition using TiSi-alloy as arc sources. It was clearly proved that corrosion resistance in 1 N H_2SO_4 and 3.5% NaCl solutions increased with reduced surface roughness. The reason is that the dense (less porosity) or amorphous structure makes the films less permeable by the corrosion medium. The Ti-Si-N film exhibits superior corrosion resistance as the number of microparticles or surface roughness is reduced. Fig. 2-7 shows the polarization curves of various Ti-Si-N coatings tested in 3.5 wt.% NaCl solutions. It was established that the corrosion potential (E_{corr}) is reduced with increasing surface roughness.

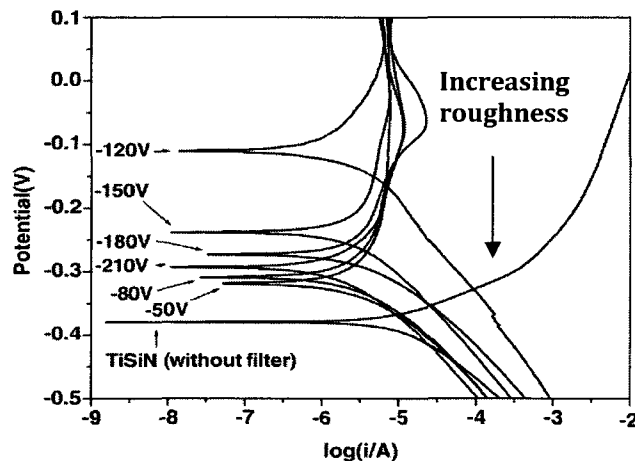


Fig. 2-7. Polarization curves of various Ti-Si-N coatings tested in 3.5 wt.% NaCl solution [33].

2.2. Hydrophobicity: concepts, properties and applications

Many terrestrial plants and animals are water-repellent due to hydrophobic surface components with microscopic roughness. It has been shown that these surfaces provide a very effective anti adhesive property against particulate contamination. This self-cleaning mechanism, called the “Lotus-Effect”, is an important function of many microstructured biological surfaces [5]. It is now recognized that the fascinating fluid behaviors observed for the lotus plant, like the rolling and bouncing of liquid droplets and self-cleaning of particle contaminants, arise from a combination of the low interfacial energy and the rough surface topography of waxy deposits covering their leaves [15]. As shown in Fig. 2-8, the surface of the lotus leaf is covered with micro-protrusions, which are clothed in nano-protrusions. The nano-protrusions are composed of epicuticular wax crystalloids that are hydrophobic [8].

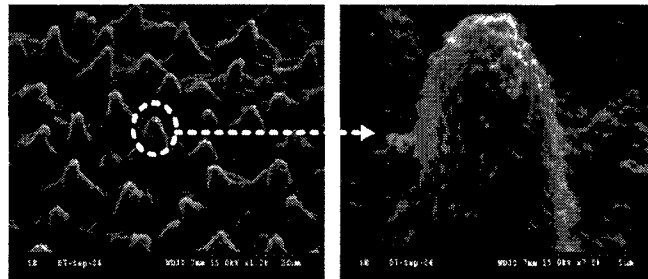


Fig. 2-8. SEM images of the surface of a lotus leaf [8].

The unusual wetting characteristics of superhydrophobic surfaces are governed by both their surface chemical composition and surface geometric microstructure [9,10]; their wettability can be decreased by creating a local geometry with a large geometric area relative to the projected area [9]. The origin of the self-cleaning property of lotus leaves has been revealed to be a cooperative effect of micro- and nano-scale structures on their surfaces [10]. Cheng and his colleagues emphasized the importance of the lotus leaf’s nanoscale hair-like structure on its self-cleaning ability [34]. Barthlott et al. assumed that “Lotus effect” can be transferred to artificial surfaces (e.g. cars, facades, foils) and hence find a huge technical application [5]. As the surface free

energy of a solid surface decreases, hydrophobicity increases. To decrease the surface free energy, rough surfaces formed either etching or by fabrication of micro/nanostructures, can be useful [8].

Wetting properties are defined by the magnitude of contact angle. If the contact angle is lower than 90° , a material is hydrophilic (wetable), otherwise it is hydrophobic (non or low wettable). The contact angle is not only material property dependent, but it changes with the surrounding conditions, time and it also depends on the history of wetting [36].

The apparent contact angle (θ) between a rough surface and a liquid droplet can be determined using:

$$\cos \theta = r \cos \theta_T, \quad (2-1)$$

where r is the roughness ratio (the actual surface area divided by the apparent surface area) and θ_T is the thermodynamic contact angle defined by:

$$\cos \theta_T = (\gamma_{sv} - \gamma_{sl}) / \gamma_{lv}, \quad (2-2)$$

where γ_{sv} is the solid–vapor surface energy, γ_{sl} is the solid–liquid interfacial energy and γ_{lv} is the liquid–vapor surface energy (see Fig. 2-9). As roughness increases, air can be locally trapped underneath the liquid, resulting in the formation of a composite surface with a large contact angle, a phenomenon that is described using the following theoretical equation:

$$\cos \theta = f_S \cos \theta_T - f_{air} \quad (2-3)$$

Where f_S is the fractional contact area between the liquid and the solid surface, and f_{air} is the fractional contact area between the liquid and the air underneath the droplet [4].

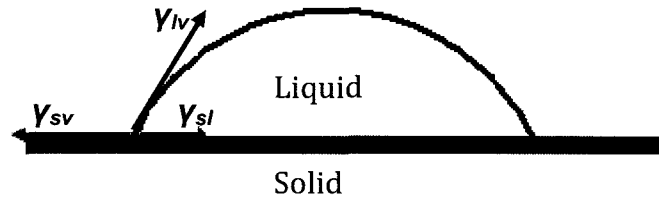


Fig. 2-9. The schematic illustration of surface tensions on a solid surface in contact with a water droplet, where γ_{sv} is the solid–vapor surface energy, γ_{sl} is the solid–liquid interfacial energy and γ_{lv} is the liquid–vapor surface energy.

The successful advancement of micro-electro-mechanical systems (MEMS and NEMS [4,8]) with miniature moving parts, including micromotors, gears and transmissions, mechanical discriminators and optical microswitches, relies on the development of new wear resistant materials and surfaces with high hydrophobicity (water repellency) and low adhesion and friction. Other possible applications for durable water repellent surfaces range from micro-fluidic devices to bipolar plates in proton exchange membrane (PEM) fuel cells [4,6]. This effect may inspire thinking about a similar mechanism in the solid-water-corrosive matters system, namely, prevention of corrosion by repelling corrosive matters from a surface, making them easily roll off by an external force [7].

Because of superhydrophobic surfaces' interesting properties and important applications in fundamental research and industrial applications, they have attracted significant attention, and various fabrication methods have been reported [36]. Many methods have recently been developed to fabricate surfaces with controlled roughness through various approaches such as the sol–gel process, generation of a fibrillar structure, creation of a rough surface covered with low surface energy molecules, and the phase separation of a polymer in a mixed solvent system. Most of the methods unveiled to date, however, are not suitable for the fabrication of protective coatings on metal substrates with complex shapes [9]. The formation of self-assembled monolayers (SAMs) using monomeric compounds that bear a surface-reactive group has been known to be a simple and practical technique for controlling wettability, corrosion, and adhesion of solid surfaces [20].

2.2.1. Hydrophobicity of metals

Superhydrophobic surfaces are of great importance for many industrial applications, and may present a solution to the long-standing problems of environmental contamination and corrosion of metals [7]. The prospect of producing surfaces that repel water suggests huge opportunities in the area of corrosion inhibition for metal components, chemical and biological agent protection for clothing, antifouling for marine vehicles, among many other applications [34].

Generally metals are hydrophilic or wettable. To create a hydrophobic surface on a metal there are some methods such as creation of surface patterns, using some chemicals and a combination of surface patterns and chemicals. The two main methods of applying sufficient pattern are etching a metal substrate and electroless deposition of a metal coating onto the substrate. Other methods which produce metal-based superhydrophobic surfaces include sulfur treatment, either with sulfur gas or direct mixing of a thiol solution with a metal (Cd or Zn) salt solution. Electrochemical methods to provide roughness have also been reported for indium tin oxide (ITO)-coated glass and doped silicon. A range of techniques, including anodization has been successfully applied to Al. Between presented reports; there are two different approaches to lowering the surface energy of the roughened surfaces: use of fluorinated silanes or of fluorinated thiols. For metals the range of compounds that could be used to lower the surface energy is much larger since there are numerous functional groups that bind to metals. Despite the diversity of approaches, which have been applied to creating superhydrophobic metal surfaces there are just two factors, which dominate the ultimate performance. One is the roughness or texture of the surface, the second is the nature of the surface modifying layer [34]. Generally, metal oxides are more hydrophobic than the metal, so the wettability may become lower with increase in the amount of metal oxide [37]. The weaker wetting properties of aluminum, brass and stainless steel can be explained by the process of passivation, e.g. covering with the thin layer of oxide. The zinc,

aluminum or chromium oxides are hydrophobic. The passivation of copper is not such a rapid process as it is in the case of aluminum, zinc or chromium, so the surface of copper plate remains hydrophilic [36].

Wang and Kido studied the wetting characteristics of natural mica, polished, air oxidized and water immersed pure chromium, nickel, iron and SUS304 steel surfaces. They found that the wettability of natural mica and each metal surface differs from the others and the nano-size wettability is higher than the millimeter-size even for the same metal surface [37]. It was found that copper has the best wettability properties, followed by: aluminum, brass and stainless steel. Aluminum and stainless steel lose their hydrophobic properties during the dropping procedure while copper and brass remain hydrophilic or hydrophobic [34].

2.2.1.1. Hydrophobic surfaces on steel

A convenient method to prepare a water-soluble hydrophobic agent and create a super-hydrophobic film on the base material is by use of a film or electroless Ni-P composite coating on carbon steels (Fig. 2-10) as shown by Zhu and Jin [21]. That super-hydrophobic film, has good stability in the air at room temperature and good corrosion resistance in 5 wt.% NaCl solution, neutral salt spray test and water erosion test.

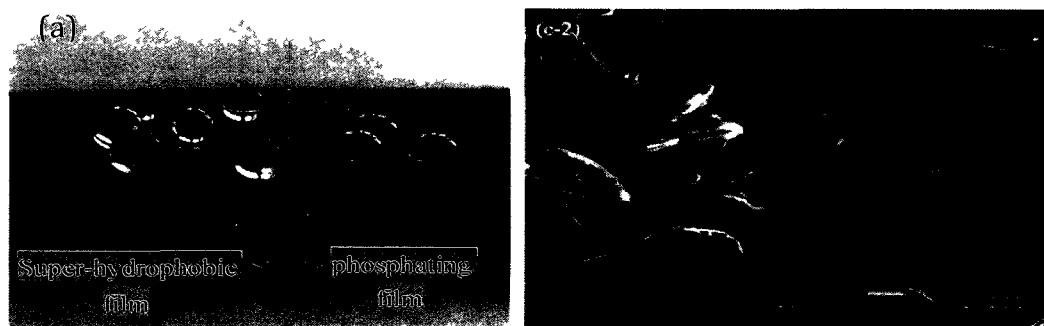


Fig. 2-10. (a) Photo of water droplets on the phosphating film and superhydrophobic film, (b) SEM image of the superhydrophobic film which was fabricated by silicon sol [21].

Wu and his collaborators fabricated stainless steel-based superhydrophobic surfaces by microstructuring using a femtosecond laser and the method of Silanization [12]. Fig. 2-11 shows SEM images of their created surfaces. They proved that these micro- and submicron double-scale structure surfaces yield apparent contact angles higher than those on single scale structure surfaces, and the maximum value was 166.3° . Also their results confirm that the fraction of air between the water droplet and the double-scale surface was large, which is the important reason of superhydrophobicity of the surface. This provides a simple and easily-controlled method for fabricating stainless steel-based superhydrophobic surfaces [12]. Fig. 2-12 is a schematic illustration of their laser work.

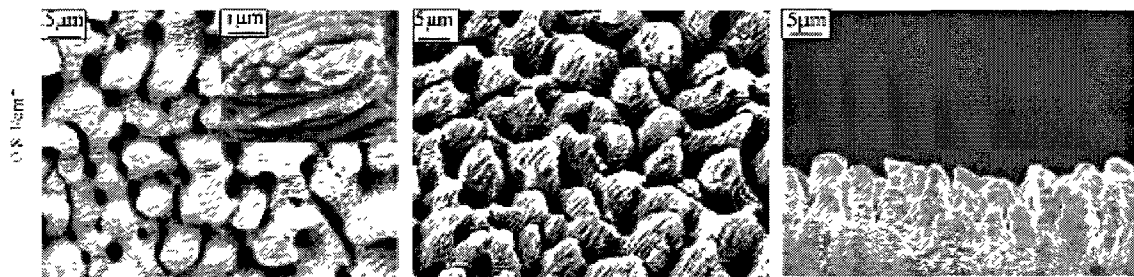


Fig. 2-11. Top (left), side (308) (middle) and profile view (right) SEM micrographs of AISI 316L type austenitic stainless steel-based [12].

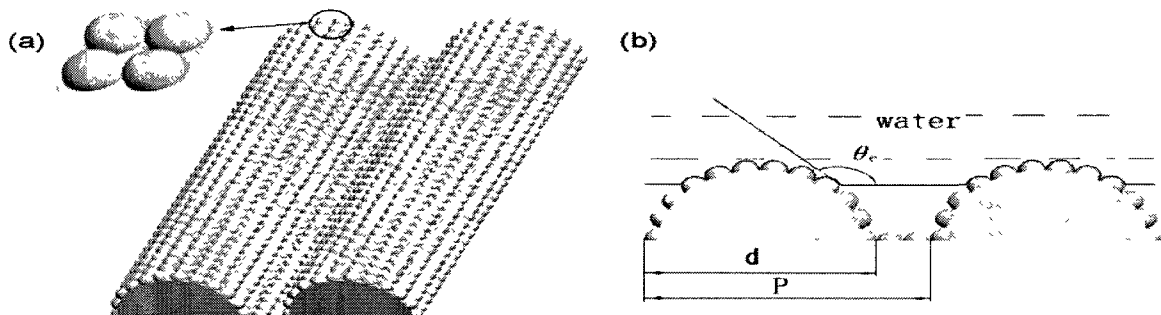


Fig. 2-12. Schematic illustration of laser-induced periodic surface structure (LIPSS) covered with nanoparticles formed at fluences 0.08 J/cm^2 . (a) The alternating array of LIPSS and nanoparticles. (b) The local interaction of the sort water interface with the top of LIPSS [12].

Larmour and his collaborators [11] worked on improving thiol-modified systems. No combinations of etching, Au coating and thiol modification were capable of producing surfaces at the higher ends of the superhydrophobic range for Ti, Zn

and Fe. Application of a sacrificial copper layer followed by an electroless galvanic deposition method can produce a good hydrophobic surface. This general method for the preparation of superhydrophobic surfaces on metals is sufficiently simple and inexpensive to be suitable for application on an industrial scale, for example in marine or aeronautical engineering. “Etch and coat” methods are potentially useful for large scale production of superhydrophobic surfaces on metals [11]. Kurtz et al. described such an aqueous post-dip treatment (Betatec), providing corrosion resistance for various types of metal surfaces without impairing the contact resistance and other technical properties [38]. The Betatec post-dip can impart beneficial hydrophobic properties to the gold surface with subsequent blocking of pores. This beneficial post-treatment has no adverse effects on electrical, solderability, or bonding properties of the gold electrodeposits.

2.2.1.2. Hydrophobic surfaces on nickel

Nickel-based alloys have been studied and used as biomaterials due to their corrosion resistance and excellent metallurgical compatibility with alloying elements. Shi et al. have studied the tribochemical behavior of nickel sheets on exposure to a mixture of biomaterial solutions (cell culture media). The nickel sheets used in this research were designed as filters (see Fig. 2-13). They found that the droplet contact angle of the Ni sample is 128.3° , which shows the dry nickel samples are hydrophobic [39].



Fig. 2-13. Surface and microstructure of Ni; SEM images: (a) left, overview, (b) middle, pentagon, (c) right, pore [39].

Hexagonal-shaped nickel micromeshes (see Fig. 2-14) were designed and fabricated and their water-repellent and water-proofing abilities were investigated by Lee and his collaborators [8]. By the effect of the micromesh and PPFC coating, the contact angles were increased sharply from 63° of the non-coated flat nickel to 140° of the PPFC-coated micromesh to modify the surface from hydrophilic to superhydrophobic. The hole size and increasing the lattice width of the micromesh are necessary to improve the water-proofing ability. The proposed nickel micromesh sheets can be applied to many application areas that require water-blocking yet must allow passage of gases or sound waves. Examples include water-proof phones/speakers and water-proof gas detectors [8].

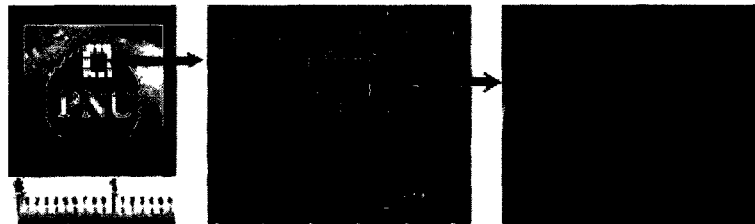


Fig. 2-14. Fabricated nickel micromesh sheet: (a) photograph of a nickel micromesh prototype unit, (b) & (c) magnified SEM images of the micromesh [8].

Lotus leaf surface-textured nanocrystalline (NC) Ni films, developed by replicating the original biotexture, modified using a selective electrodeposition and a PFPE solution treatment were fabricated by Shafiei and Alpas (see Fig. 2-15). The superhydrophobicity of the NC Ni films is attributed to successful development of a multi-level surface roughness (where a nanoscale surface texture was superimposed on a microscale structure of protuberances) with a low surface energy [4].

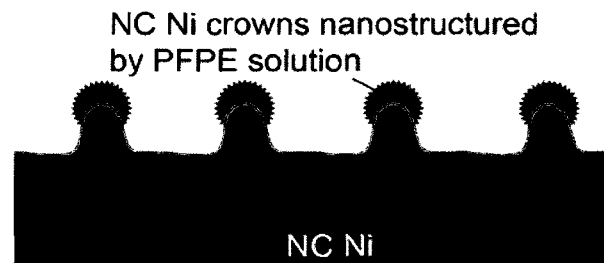


Fig. 2-15. A PFPE solution treatment of the surface created a nanotextured layer on the "Ni"

crowns" [4].

The hydrophobic and protective mechanism has been evaluated [38] by water contact angle measurements on pure copper, nickel, and gold deposits together with nickel/gold plating on copper (before and after treatment with the gold post-dip). The tests for a nickel surface (surface energy of nickel is 2.45 J/m^2) showed a contact angle of approximately 92° after treatment with the post-dip. Hence, despite nickel possessing considerably higher surface energy, thereby making it more hydrophilic, Beratec post-dip treatment was very effective at imparting hydrophobic surface properties (Fig. 2-16).

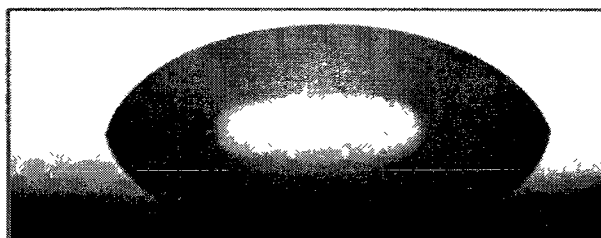


Fig. 2-16. Wetting of an acid-activated nickel surface by water after treatment with Betatec gold post-dip, $\theta=92^\circ$ [38].

2.2.1.3. Hydrophobic surfaces on copper

Han et al. [9] attempted to mimick nature by combining the features of metallic and organic coatings in the protective coating of a metal surface. According to their results, nanostructured copper sulfide was formed on the micro-structured copper surfaces, and the hydrophobization was successfully performed with a perfluorosilane compound via a solution process, resulting in the formation of ultra water-repellent metal surfaces. The obtained surface structure is shown in Fig. 2-17. Superhydrophobic surfaces composed of interconnected $\text{Cu}(\text{OH})_2$ nanowires were constructed on copper plates via a simple immersion process in an aqueous solution by Pan et al [40]. They claimed this method is easy, fast, inexpensive and environmentally friendly. Since copper can easily be coated on the surfaces of various engineering metals, their results introduced a new pathway for the fabrication of superhydrophobic surfaces on engineering metals with many industrial applications. Xi and his collaborators [41] prepared copper surfaces via electroplating of different current densities to produce various

roughnesses. Some of the prepared copper surfaces behaved hydrophobic without chemical modification. When the surface configuration was properly fabricated, super-hydrophobicity could be obtained even on a hydrophilic substrate. Fig. 2-18 shows the SEM images of the copper surfaces where spherical grains are observed.

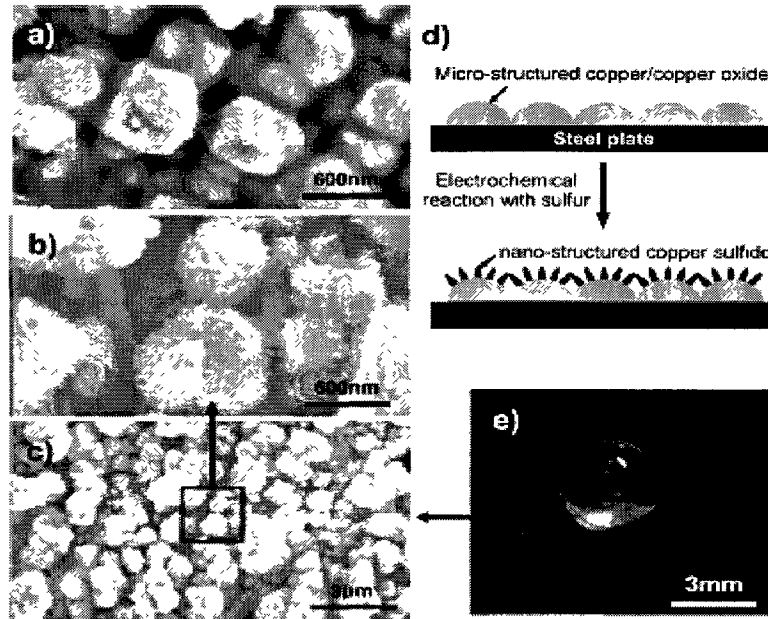


Fig. 2-17. SEM images of the formation of the superhydrophobic metal surface and an image of a water drop on this surface: (a) the as-deposited copper surface; (b) High magnification image of the copper surface after electrochemical reaction with sulfur gas at 150 °C for 10 min; (c) Low magnification image of (b); (d) Schematic diagram of the formation of the micro- and nanostructured metal surface; (e) Optical image of a water drop on the surface in (b) [9].

Liu et al. created a novel super-hydrophobic film by *n*-tetradecanoic acid chemically adsorbed onto the copper sample. They suggested that a composite interface formed by the flower-like surface nanostructures, water droplet and air trapped in the crevices is responsible for the superior water-repellent property (Fig. 2-19). Their findings show that hydrophobicity plays an important role in corrosion behavior compared to the film thickness. Corrosion of copper was effectively inhibited by formation of a super-hydrophobic film [13]. In another similar work, *n*-tetradecanoic acid ($\text{CH}_3(\text{CH}_2)_{12}\text{COOH}$) etch, the super-hydrophobic film was formed on the fresh copper surface [14]. The

microstructural results showed that the film is similar to haulm (a plant) or flower and the seawater contact angle is larger than 150° . The results prove that the super-hydrophobic surface can significantly improve the corrosion resistance of copper. As said, this method is a simple and inexpensive one to create superhydrophobic surfaces on copper. However, The interaction of pure *n*-tetradecanoic acid and copper surface was very weak, so bis-[triethoxysilylpropyl]tetrasulfide (BTESPT) was used to link *n*-tetradecanoic acid and copper surface in order to enhance their interaction [42].

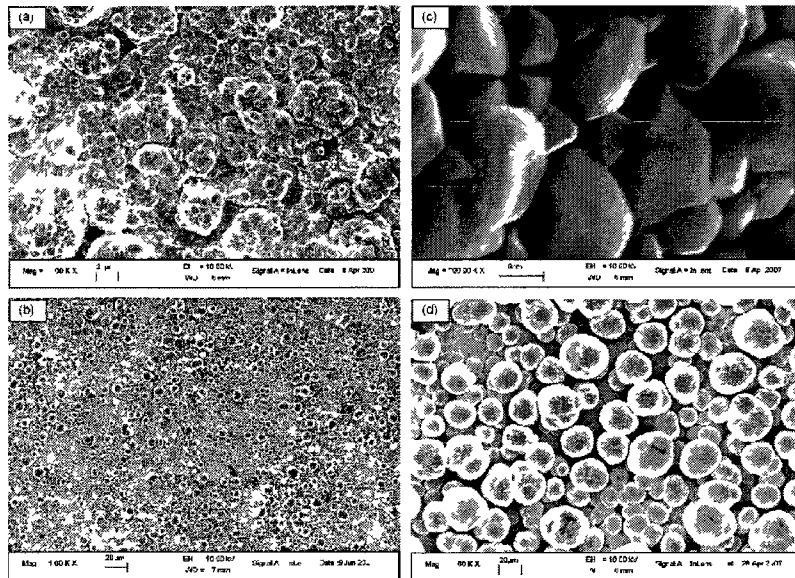


Fig 2-18. SEM images of the copper surfaces with different produced at different current densities: (a) current density = 0.04 A/cm^2 , contact angle = 125° (b) Current density = 0.08 A/cm^2 , Contact angle = 153.5° (c) Enlarged SEM image on surface b (d) Current density = 0.10 A/cm^2 , Contact angle = 132.5° [41]

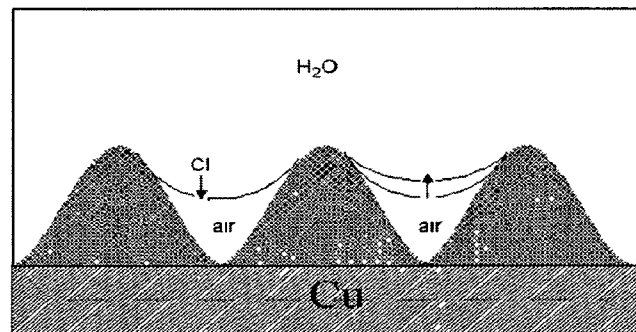


Fig 2-19 Model of the interface between super-hydrophobic surface and sterile seawater [13]

Wu and Shi [43] fabricated a lotus-like micro-nanoscale binary structure surface of copper phosphate dihydrite using galvanic cell corrosion of a copper foil with aqueous phosphorus acid solution droplets. They showed that the surface wettability can be changed from superhydrophilic to highly hydrophobic or superhydrophobic by just heating or modify it with an *n*-dodecanethiol monolayer. This method can be easily scaled up and has potential applications in industry for producing superhydrophobic materials and it is able to be applicable for making other interesting micro–nanoscale structures using a different electrolyte or changing the substrate to another metal or alloy.

2.2.1.4. Hydrophobic surfaces on aluminum

Cho et al. designed and synthesized a new random copolymer, poly (TMSMA-*r*-fluoroMA), with the aim of fabricating superhydrophobic surfaces on oxide-based substrates. As a model substrate, they fabricated aluminum substrates with varying roughnesses by controlled anodic oxidation. A superhydrophobic surface was generated with the polymer coated nanoporous anodic aluminum oxide (AAO) substrate (Fig. 2-20). They suggested that poly (TMSMA-*r*-fluoroMA) could be applied to the coating of a variety of hydroxyl-presenting materials, such as glass, Si wafers, polymers, and other metals [20].

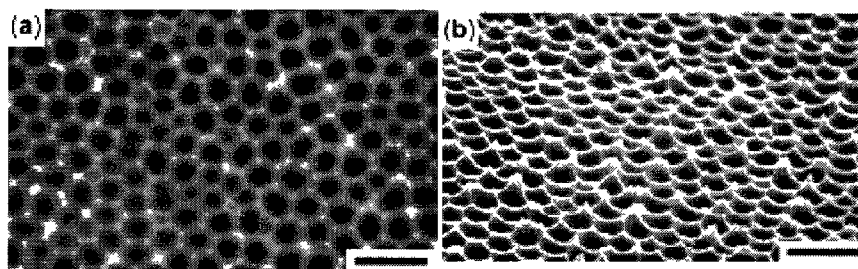


Fig. 2-20. FE-SEM images of the textured aluminum sheet: (a) top view and (b) tilted view. The scale bar is 1 μm [20].

Barkhudarov and his co-workers investigated the effectiveness of superhydrophobic films as corrosion inhibitors. They concluded that the extreme case of a superhydrophobic coating with a contact angle of $>160^\circ$ decreases the rate of corrosion roughly tenfold compared to the unprotected aluminum. Fig. 2-21 shows the changes in aluminum thickness after the test with different surface

conditions. More importantly, making the protective layer superhydrophobic rather than hydrophilic improved corrosion by a factor of six [15].

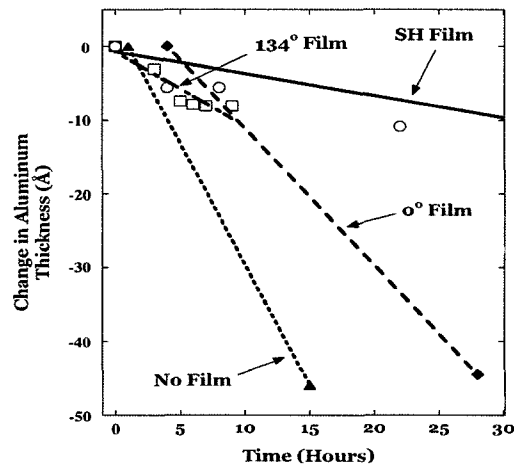


Fig. 2-21. The change in thickness of the aluminum layer versus time for samples protected by films of varying contact angle and a sample with only native Al_2O_3 layer (without protective film) [15].

Liu and his collaborators have successfully created a superhydrophobic surface on aluminum surface by an anodization process and chemical modification using myristic acid. The electrochemical measurements showed that the superhydrophobic surface significantly improves the corrosion resistance of aluminum in sterile seawater. The superhydrophobic surface affects mainly on the aluminum anodic reaction, whose currents (I_{corr}) are reduced by about three orders of magnitude, the corrosion potential (E_{corr}) shifts positively by 0.2 V when the anodized aluminum is covered with the myristic acid (Fig. 2-22). It is believed that this method can be easily applied to large scale production of superhydrophobic engineering materials with ocean industrial applications [7].

In another research Liu et al. [16] studied the use of superhydrophobic surfaces on aluminum as a method for inhibition of microbially influenced corrosion (MIC). Their study claims that the superhydrophobic film does not only decrease the corrosion current densities (I_{corr}), but also microbially influencing corrosion acceleration inhibition (MICI) due to preventing colonization of microorganisms [16]. The analysis of potentiodynamic polarization, EIS and appropriate equivalent circuit models reveal that the aluminum corrosion is effectively

inhibited by the formation of a stable super-hydrophobic film [17]. Fig. 2-23 shows the untreated and treated surfaces of aluminum prepared by myristic acid in Yin et al.'s research.

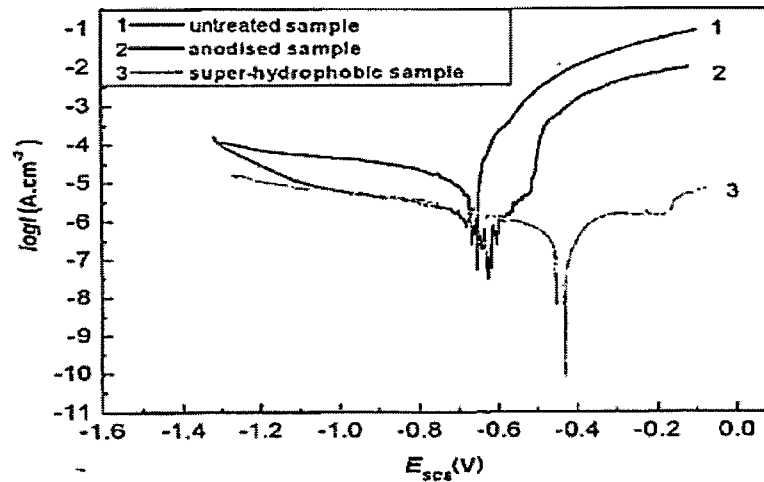


Fig. 2-22. Potentiodynamic polarization curves of untreated, anodized and superhydrophobic samples for 34 h in sterile seawater at 2mVs^{-1} [7].

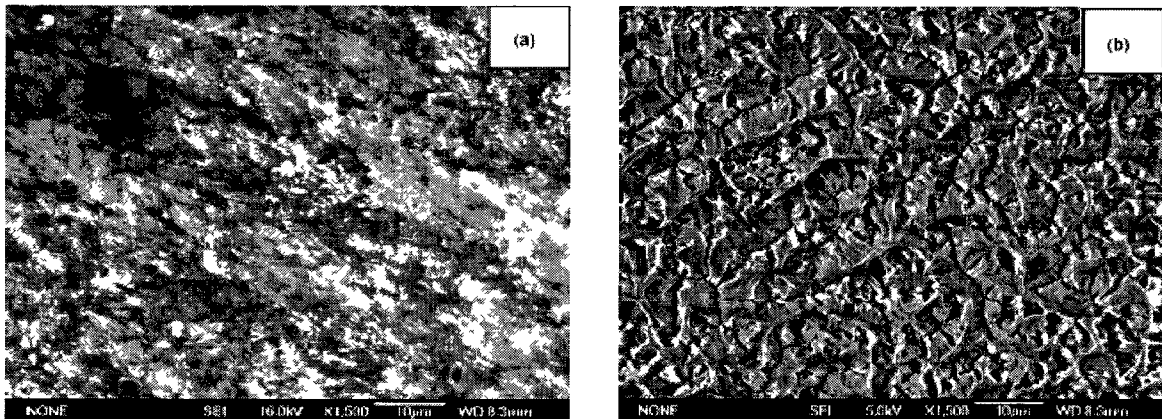


Fig. 2-23. SEM images of (a) the untreated aluminum and (b) the superhydrophobic aluminum surfaces [17].

The electrochemical measurements [18] showed that the super-hydrophobic surface significantly improves the corrosion resistance of aluminum in sterile seawater. The proposed mechanism of the underwater superhydrophobic surface applied in the corrosion resistance is presented by He and co-workers in a schematic figure (Fig. 2-24). The figure shows a surface with roughness of $2\ \mu\text{m}$ which is plunged in seawater. As it is seen the water could not wet all parts of

the surface and because of the roughness a portion (white areas) of the surface is unwetted.

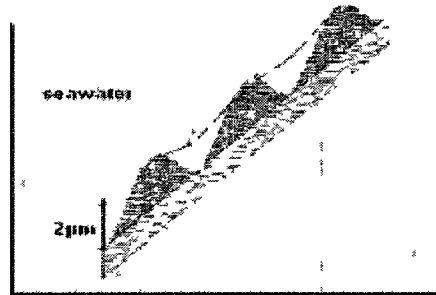


Fig 2-24 A schematic of a rough surface immersed in seawater [18]

2.2.1.5. Hydrophobic surfaces on other materials

A superhydrophobic film was prepared by myristic acid chemically absorbed onto the polyethyleneimine (PEI) coated Fe_3Al -type intermetallic wafer. Liu et al. demonstrated a simple and inexpensive method to create superhydrophobic surface on Fe_3Al [36]. Anodic films were prepared on the AZ91D magnesium alloy in the electrolyte of 1.0 M Na_2SiO_3 with and without the addition of silica sol by Li's group [44]. The addition of silica sol increases the thickness of the anodic film and improves the roughness of the film surface. As a result, such anodic films reveal some hydrophobic property. Moreover, the anodic film formed with a sol addition reveals higher hydrophobicity and provides higher corrosion resistance for AZ91D Mg alloy than the anodic films formed in the base electrolyte with more or less silica sol addition [44].

Narhe and collaborators [45] studied the water condensation on a metallic zinc surface, regularly used as anticorrosive surface. The zinc surface was coated with hydroxide zinc carbonate by chemical bath deposition. The results show that, on such surfaces, water condensation, although a complex and challenging process, is similar to smooth planar surfaces. As the nucleation events occur at a much smaller length scale than the surface texture scales, the surface chemistry dominates the texture effects during condensation and therefore leads to similar results as on a smooth surface. In particular, it is noticeable in view of corrosion effects that the water surface coverage remains on order of 55%. This process is

a simple and powerful method to modify the surface roughness and wettability, from hydrophobic to superhydrophobic.

It is feasible to create a super-hydrophobic PDMS surface with ultra-low water adhesive force by a simple one step laser-cutting method, which can also be extended to fabricate other polymers. Jin et al. [10] demonstrated a facile one-step laser-etching method to fabricate rough polydimethylsiloxane (PDMS) surface containing micro-, submicro-, and nano composite structures. The SEM image of created microstructure is shown in Fig. 2-25. Spori et al. [46] analyzed four different (sandblasted glass slides as well as replicas of acid etched, sandblasted titanium, lotus leaves, and photolithographically manufactured golf-tee shaped micropillars [GTMs]), heavily structured over a wide range of surface energies via water contact angle measurements. With regard to superhydrophobic surfaces, the golf-tee-shaped (GTM) pillars show stable superhydrophobicity over a wide range of surface energies. This topography seems to be a very effective design for microstructured, superhydrophobic surfaces.

Wu et al. [47] studied the influence of chemical and morphological modifications on the hydrophobicity of a silica based sol-gel hard coating. The substrate was anodized aluminum alloy AA6061. They obtained a sol-gel coating material and process which provides a one-step and low-cost method to obtain hydrophobic coatings with hard and durable properties for industrial applications. Shen and his co-workers prepared nano-TiO₂ coatings on the surface of the type 316L stainless steel and improved its corrosion resistance. To increase the surface hydrophobic property, fluoroalkylsilane (FAS-13) was applied on the surface of nano-TiO₂ coating using a self-assembly method. Their electrochemical test results indicated that the hydrophobic coatings have an excellent corrosion resistance in oxygen-saturated Ringer solution (Ringer's solution technically refers only to the saline component, without lactate). The corrosion potentials shift positively, I_{corr} decreases by three orders of magnitude, and the corrosion resistance R_i increases by more than 1000 times; so surface

modification by TiO_2/FAS coatings might become a promising technique in significant improvement of the corrosion resistance of metals [48].

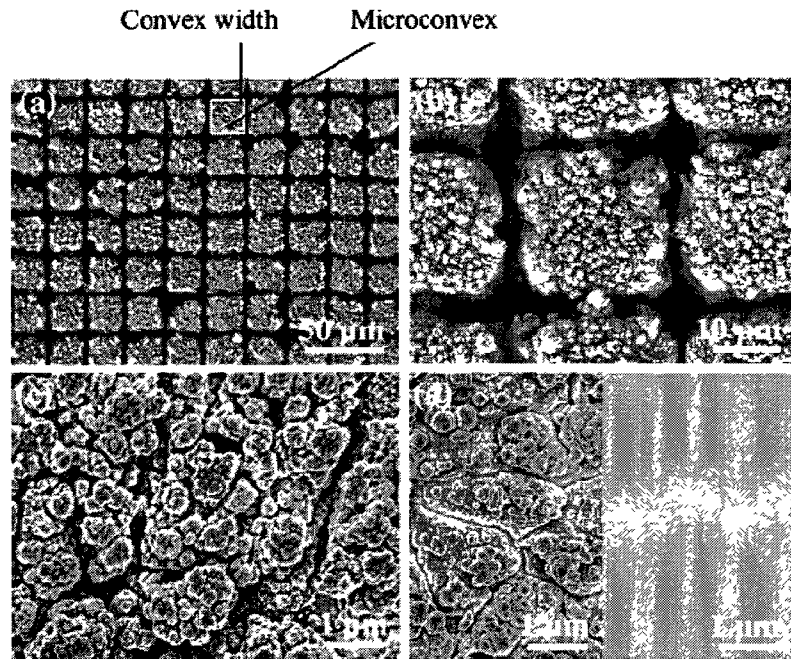


Fig. 2-25. (a) Typical SEM images of the laser-etched PDMS surface with the convex width of about 25 μm , showing the regular arrays of microconvexes; (b) magnified image of (a), showing the submicro structures on each convex; (c) high-resolution image of a single convex of (b), showing the nanoparticles composed of each submicro block; (d) high resolution image of a single convex with width of about 50 μm (left) and a flat PDMS surface (right) [10].

2.3. Laser surface patterning

The surfaces of different materials have been processed with different laser methods to create surface patterns.

Textured surfaces basically consist of an array of lines or dots with periods between 20 and 200 μm fabricated using direct laser writing technique which means that each dot or line must be written with the laser beam separately [49]. Interfering laser beams from a high-power pulsed laser provide the opportunity of applying a direct treatment of the surface microstructure of metals in micro/nano-scale based on photo-thermal mechanisms [50]. Selected laser melting (SLM) technology is able to meet the needs of manufacturing parts with the desired microstructure as well as macrostructure [51]. The “Laser Interference

Metallurgy” method permits the creation of periodic arrays with a well-defined long-range order on metallic surfaces from the sub-micrometer level up to micrometers. The principal advantage of Laser Interference Metallurgy is given by the fact that only a unique preparation step is required whereas other patterning methods (e.g., replica moulding, conventional lithography) comprise at least two different steps. Additionally, no masks are required and relatively large areas can be directly structured (in the order of cm^2) in a short time scale [50].

A laser beam can be focused on a solid surface producing removal of target material, or it can be expanded and an ablation mask used. The incident energy and the time of interaction between the laser radiation and the target surface determine the phenomena that occur: a wide area of processes can be induced, from local heating to a very accurate removal of material without affecting the surrounding zones when ultra short laser pulses are used [52].

A patterned surface can be fabricated by many techniques, such as chemical vapor deposition, anodization, soft etching, and optical lithography. The laser fabrication technique provides an effective tool to fabricate periodic structures on any material surface due to its ultrahigh peak power [19]. Currently, several methods exist for producing multi-scale textures on materials’ surfaces via microfabrication based on, but not limited to lasers, electron beams, and lithography. A relatively new method, interface method, takes advantage of the superposition of interfering beams of light to create a pattern of lines or dots, with significant long-range order, on the surface of a material. In order to accomplish this, properties of both the material being processed and the laser being used must be taken into account. The choice of laser has a large influence over the type of surface structure that is produced [53].

2.3.1. Laser interface metallurgy method

Duarte et al. [49] tested the tribological behavior and lifetime of the lubricating film improvements on material textured by means of laser interface metallurgy. They used a commercial 304 stainless steel substrates and a high power pulsed

Nd:YAG laser. Fig. 2-26 shows the different periodic arrays fabricated using 2 and 3 laser beam configurations in their work. They concluded that Laser Interference Metallurgy is a powerful and fast surface texturing method to fabricate several types of periodic arrays with a defined geometry on metallic substrates and these textured surfaces can be used to significantly improve tribological behavior of the target material especially under lubricant starvation conditions. Lasagni and co-workers [50] presented an alternative method to directly fabricate periodical structures on commercial metallic substrates with two and three laser beam configurations. Fig. 2-27 shows the fabricated surfaces on stainless steel substrates in different conditions.

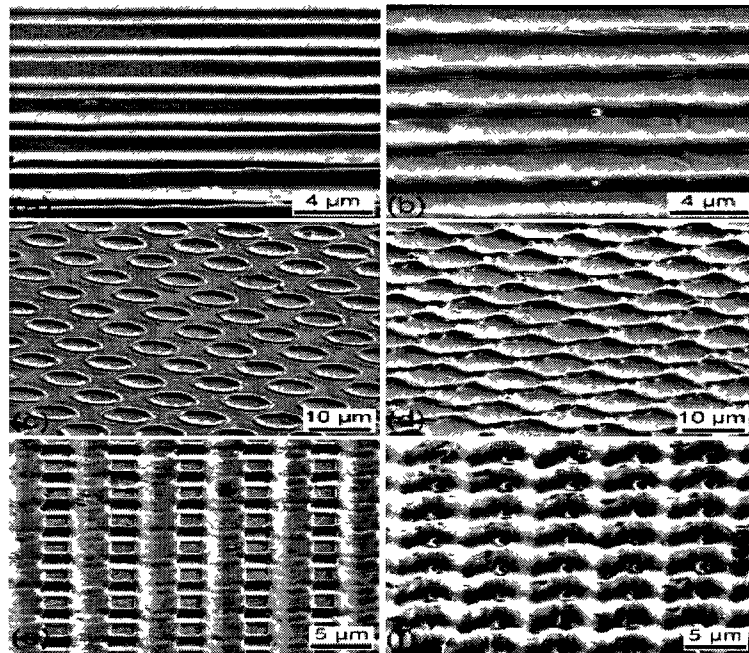


Fig. 2-26. Scanning electron micrographs of the structured surfaces irradiated with low and high laser intensities. Line-like structures: low (a) and (b) high laser fluence; Dot-like structures: low (c) and (d) high laser fluence; Cross-like structures: low (e) and (g) high laser fluence. Tilt: 52° [49].

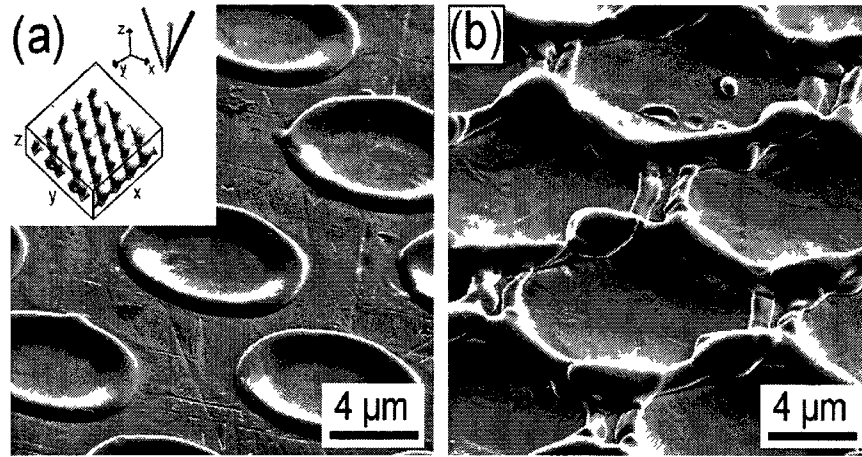


Fig 2-27 SEM micrographs of three laser beams irradiated stainless steel substrates (period = 8.00 mm) (a) 2.15 J/cm²; (b) 2.41 J/cm². The insert in (a) shows the three laser beams configuration and the calculated interference pattern Tilt: 52° [50]

2.3.2. Laser patterning on stainless steel

Lloyd and co-workers used two types of lasers to create a surface pattern on AISI 304 stainless steels. A cross hatched scanning method technique results in the production of highly regular arrays of microfeatures on the surface of a metallic sample (Fig. 2-28). Also, it was found that to avoid the reliance on self-assembly, it is possible to control not only the size but also the arrangement of microstructures by changing the way the laser beam is scanned over the target [54].

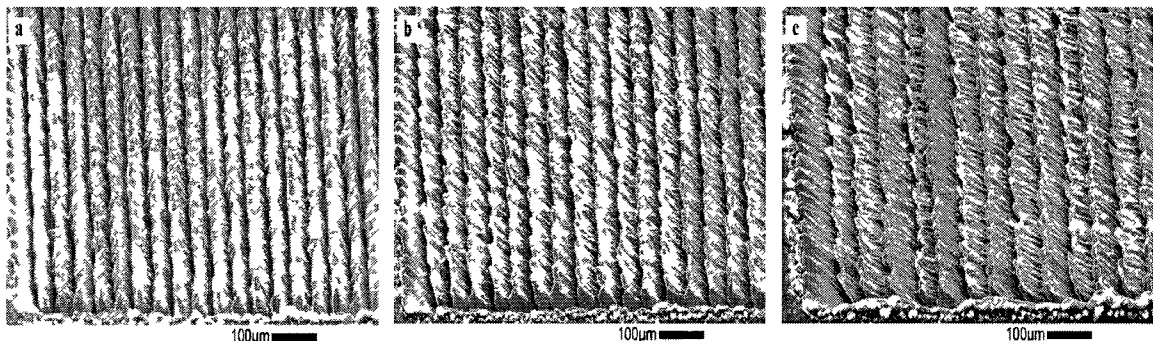


Fig 2-28 SEM images (view tilt 30°) of the surface at incident beam angles of (a) 75°, (b) 60°, and (c) 45° using the following parameters: Laser wavelength 1064 nm, intensity 0.43 GW/cm², and 5000 pulses/spot [54]

Dumitru and his colleagues [52] applied a commercial Nd:YAG laser to directly produce structures on steel surfaces (AISI 440C). The microstructure of laser induced surface is presented in Fig. 2-29. Their tribological tests showed that the lifetime of the laser-processed samples increases in comparison with unstructured ones.

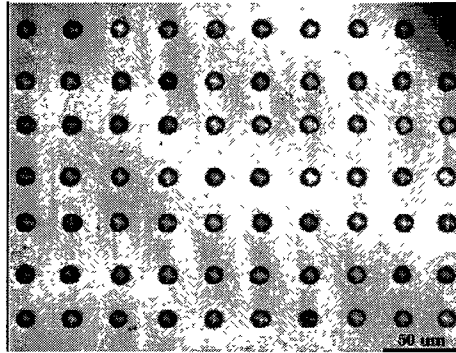


Fig. 2-29. Structure induced in a steel surface [52].

2.3.3. Laser operations on different materials

Engleman and et al. investigate the use of a writing laser and the development of laser interference surface treatment (LIST) to produce hierarchical surface microstructures and physical textures for use in biological and mechanical systems [53]. Yang et al. fabricated micro-grooves on sol-gel TiO₂ film surface by 355 nm pulse laser and investigated the relationship between wetting properties and the area of hydrophilic domain [19]. Yoon et al. created roughened PDMS surface in nano- and microscales. The modified surface showed superhydrophobicity with a contact angle higher than 170° [55]. Zhou et al. [19] used femtosecond laser to create double-scale structures on K9 glass surface. Fig. 2-30. shows the SEM image of micro-raster fabricated by femtosecond laser and the optical image of side view of micro-raster. Two types of submicron structures can be observed in the groove. They told that compared with single-scale raster, double scale structures are benefit for realizing superhydrophobicity.

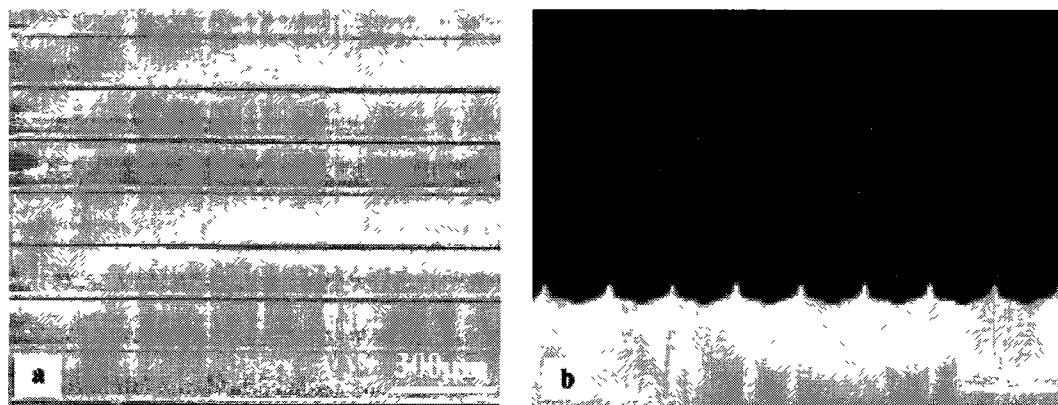


Fig. 2-30. SEM image of the micro-raster structure; b Side view of micro-raster structure [19].

3. Experimental procedures

In this chapter all the experimental steps are described sequentially. Fig. 3-1 presents a flowchart of the research procedures.

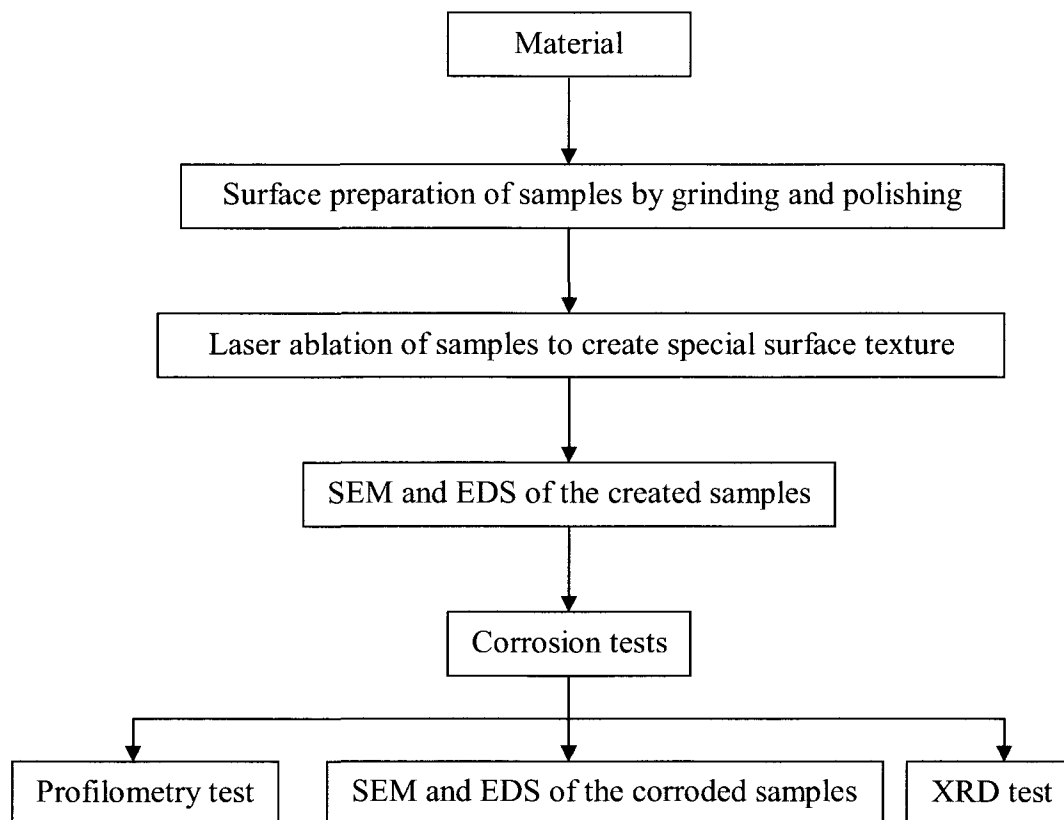


Fig. 3-1. Flowchart of experimental procedures.

3.1. Material

Pure nickel (99.7 Wt.%) was selected as model metal.

3.2. Specimen preparation

Samples of 1.5 cm × 1.5 cm size were cut from the sheet using wire electrical discharge machining (EDM) [Charmilles, model Robofil].

The surfaces of all cut samples were polished to a standard finish. All samples were first cold-mounted with a fiberglass resin and a hardener. The samples were then ground using different abrasive SiC grinding papers with grits of 180, 240, 400, 600, respectively. They were then rough polished with a 9 μm diamond suspension. Final polishing was done with alumina powder (Al₂O₃) suspensions

with particle sizes of 1 and 0.05 μm (Fig. 3-2). immediately after polishing, the samples were broken out of the cold mount and rapidly washed with ethanol alcohol and acetone and then dried.

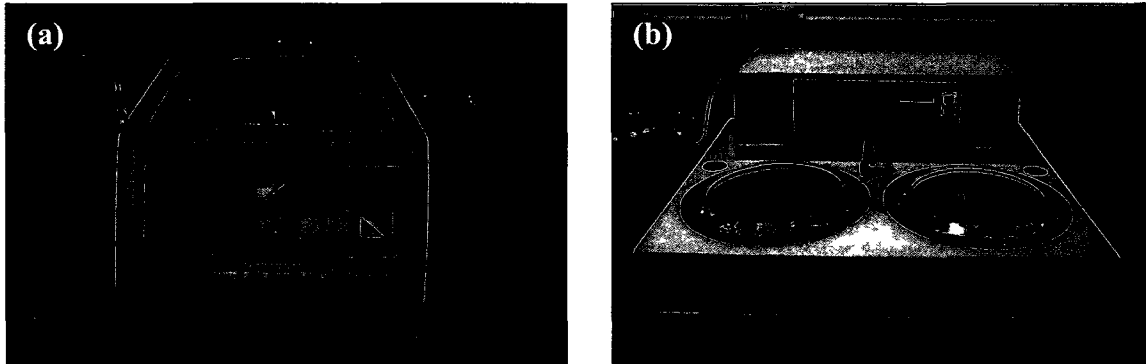


Fig. 3-2. (a) Diamond suspension and (b) alumina powder water suspension polishing machines.

3.3. Laser ablation

To create special surface textures on the surface of the samples, a laser ablation method was used. A copper bromide (CuBr) laser was used and single pulse was applied to create each hole. During laser ablation nitrogen gas (N_2) was blown to protect the surfaces from oxidation and also to clean melt splashes, and debris. The pulse duration was selected as 30 ns which is common in laser ablation processes. For each hole size a different laser power was used which ranged from 20-80 W. The laser process was completed in LMVL Bulgaria Academy of Science. The surface textures were created based on repetition of holes in form of an equilateral triangle in both X and Y directions on an area of 1.5 cm \times 1.5 cm. Fig. 3-3 shows a schematic shape of the holes and the laser ablated area on the samples.

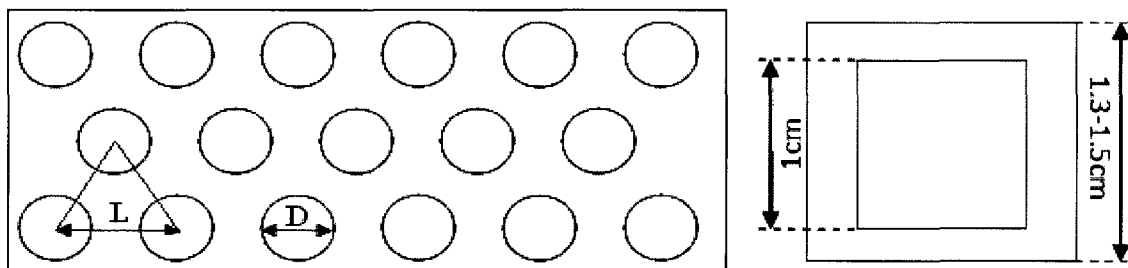


Fig. 3-3. Schematic presentation of the proposed surface texture model; D assigns to the hole diameter and L assigns to the distance between the holes. The gray area is the laser ablated region.

The size of holes and distances between them were variable to obtain different textures. Table 3-1 presents the hole size and their distances in this work. Hole distances are shown by L_1 , L_2 and L_3 . For easy identification of the samples a coding system was used; see Table 3-2.

Table 3-1. The hole sizes and their distances of the textures created on the nickel sheet surfaces

Hole diameter (D) μm	Holes' distance $L_1, \mu\text{m}$	Holes' distance $L_2, \mu\text{m}$	Holes' distance $L_3, \mu\text{m}$
5	5	10	20
10	10	20	30
20	20	30	40

Table 3-2. Sample coding system

Hole diameter (μm)	Hole distance (μm)	Code
Smooth Sample (with no hole)		REF
5	5	D5L5
5	10	D5L10
5	20	D5L20
10	10	D10L10
10	20	D10L20
10	30	D10L30
20	20	D20L20
20	30	D20L30
20	40	D20L40

3.4. Scanning electron microscopy (SEM) and EDS analysis

After surface texturing of the samples by laser ablation, the samples were examined by SEM. The EDS analysis was also used to check the chemical composition of the surfaces. The SEM instrument was JEOL 5800 which is shown in Fig. 3-4. In addition, after each corrosion test the samples were again examined by SEM to evaluate any changes in surface morphology or composition.

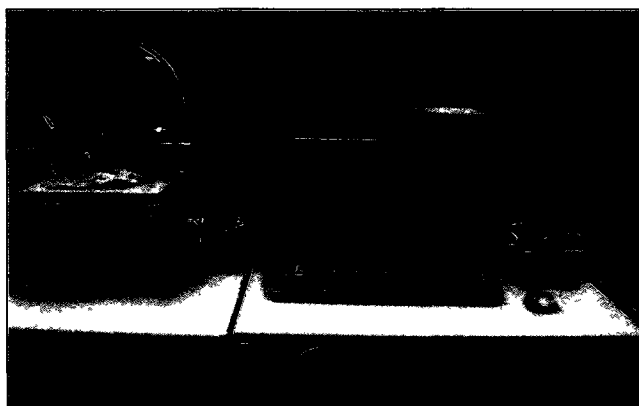


Fig. 3-4. JEOL 5800 scanning electron microscope.

3.5. Profilometry test

The roughness of the patterned surfaces after laser ablation was determined using a Wyko Surface Profiling System NT-1100. Using different magnifications from 10, 20 and 50X, the surface roughness of the samples were examined and the data were processed with the related software. Fig. 3-5 shows the profilometry instrument. The Wyko NT1100 provides high resolution 3D surface measurement, from sub-nanometer roughness to millimeter-high steps [56].

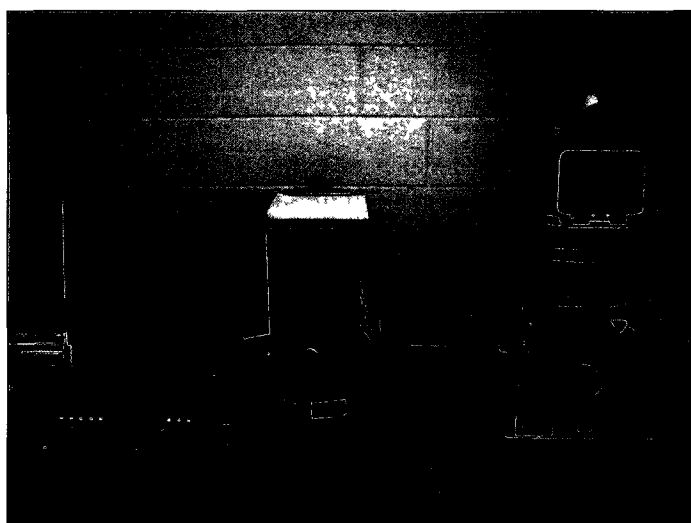


Fig. 3-5. The Wyko NT1100 profilometry machine.

3.6. Corrosion tests

The corrosion resistance of the samples was determined using a polarization method, wherein the samples were immersed into a 0.5M H_2SO_4 solution at room

temperature (24 °C). A conventional three-electrode system was used in which a standard calomel electrode (SCE) served as the reference electrode and a platinum as a cathode electrode. In the tests, potentials were applied from -0.7 to 1.5 V both versus SCE within a scan rate of 1.0 mV/s. In the corrosion tests the samples were stabilized at the open circuit potential (OCP) for 20 min and the potential-current curves were then measured. The instrument was BioLogic-SP150 equipped with EC-Lab data analysis software version 9.4x (Fig. 3-6). For each corrosion test, a fresh 0.5M H₂SO₄ solution was prepared. The Tafel slopes were calculated with the mentioned software. In some cases, the software-calculated values were not reasonable based on the curves, so in those cases the slopes were estimated using the curves in Excel Microsoft software. To calculate the linear polarization, Equation 3-1 was applied [57].

$$\frac{\Delta E}{\Delta i_{app}} = \frac{\beta_a \beta_c}{2.3(i_{corr})(\beta_a + \beta_c)} \quad (3-1)$$

Where β_a and β_c are the Tafel slopes of the anodic and cathodic reactions, respectively. i_{corr} is the corrosion current and the term $\frac{\Delta E}{\Delta i_{app}}$ is defined in ohms (volts/ampers or millivolts/milliampers).

In three corrosion tests were conducted for each sample. In each corrosion test the samples were examined using SEM, EDS and profilometry.

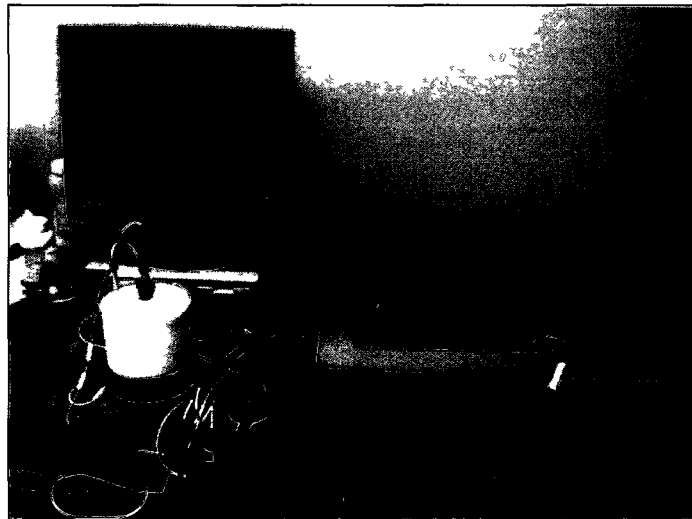


Fig. 3-6. BioLogic-SP150 instrument.

3.7. X-ray diffraction (XRD)

After the third corrosion test XRD was used to identify the phases in the samples whether they were the initial phase (f.c.c. Ni) or corrosion products. The XRD test was done using Rigaku-D Max 1200. The incident X-ray was Cu (K_{α}) with wavelength of 1.540 Å.

4. Results and discussion

In this chapter all results from SEM, energy dispersive spectroscopy (EDS), corrosion tests, profilometry test and X-ray diffraction (XRD) will be separately presented and discussed.

4.1. SEM images of the patterned samples

Fig. 4-1 shows the surface of the initial sample after final polishing. As can be seen, the surface is completely smooth and without any scratches or local rough regions. Because the final polishing was completed by $0.05\mu\text{m}$ -alumina powder particles, the maximum roughness is estimated to be around 50 nm.

Fig. 4-2 (a) and (b) show the surface of sample D5L5. The pattern on the surface is an array of attached holes. In fact because hole diameter (D) and the hole distance (L) are equal in this sample there is some overlap between holes and the pattern is difficult to see (in Fig. 3-3, imagine all holes are tangent to each other at their perimeters). The surface of sample D5L10 [Fig. 4-2 (c) and (d)] shows that there is a regular array of holes. However, in some regions one or two holes were misplaced but this is not significant. Sample D5L20 has the same hole diameter as samples D5L10 and D5L5 but the hole distance is larger than those samples by 2 and 4 times, respectively [Fig. 4-2 (e) and (f)].

Figs. 4-3 (a) and (b) present the surface of sample D10L10. This sample, like sample D5L5, has overlap between its holes. In the background of this pattern there are some horizontal and vertical lines that show the arrays of holes. In sample D10L20 the hole size is half of the hole distance (Fig. 4-3 (c) and (d)). The pattern is evident in this sample. Paying closer attention to the surface between the holes, it can be seen that there are some regions around the holes which have a different appearance compared with other areas. These regions are melt splashes which originated from the laser ablation. In fact, during laser ablation the laser locally evaporates the material within the hole regions to create the holes. So those melt splashes are due to local heating of the material. If pulse duration is decreased but with the same energy per pulse, melt splashes will decrease because the material will be sublimed rather than melted. In

addition, as it was pointed out in Chapter 3, during the laser ablation a flow of N_2 was used to remove splashes or foreign objects from the surface. Sample D10L30 [Fig. 4-3 (e) and (f)] has a regular array of holes. In this sample no misplaced holes are observed and any melt splashes are quite small. All samples with a hole diameter of $10\ \mu\text{m}$ had well-defined patterned surfaces.

Sample D20L20 has a similar appearance as samples D5L5 and D10L10 [Fig. 4-4 (a) and (b)]. In this sample, the hole diameter is larger, so the pattern is more observable. In sample D20L30 the pattern is not as clear as other samples although the hole diameter is larger. The reason is that this sample has more melt splashes due to the higher laser power used to create the holes in this sample (80 W). In fact, the larger the hole diameter or size, the more the required energy to create that hole. Sample D20L40 has almost the same surface condition as sample D20L30 but with larger hole distance. This set of samples had a regular pattern with a very low number of missed holes.

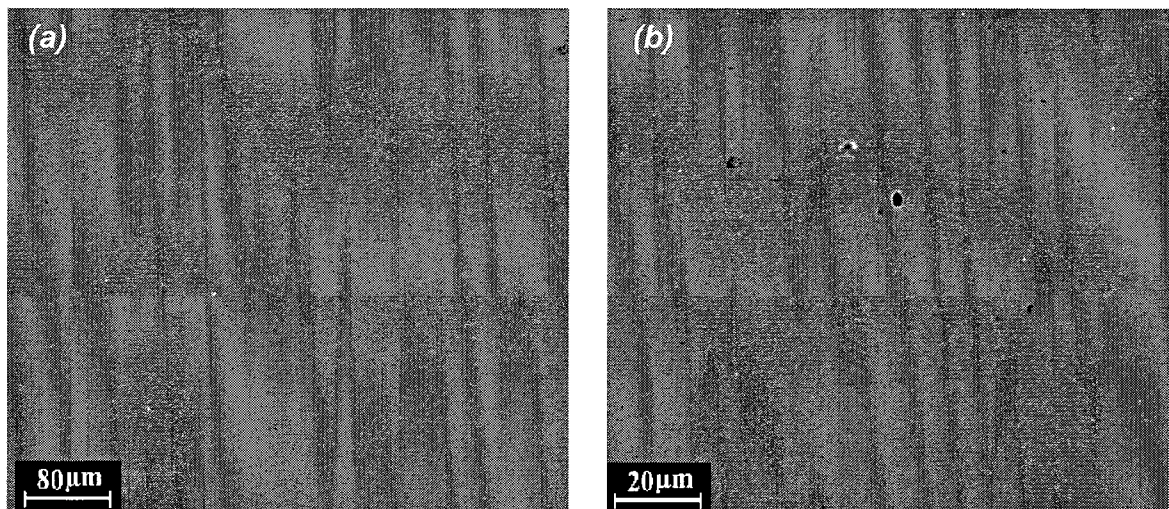


Fig. 4-1. The SEM micrographs of the initial smooth sample after final polishing with $0.05\ \mu\text{m}$ alumina particles suspension.

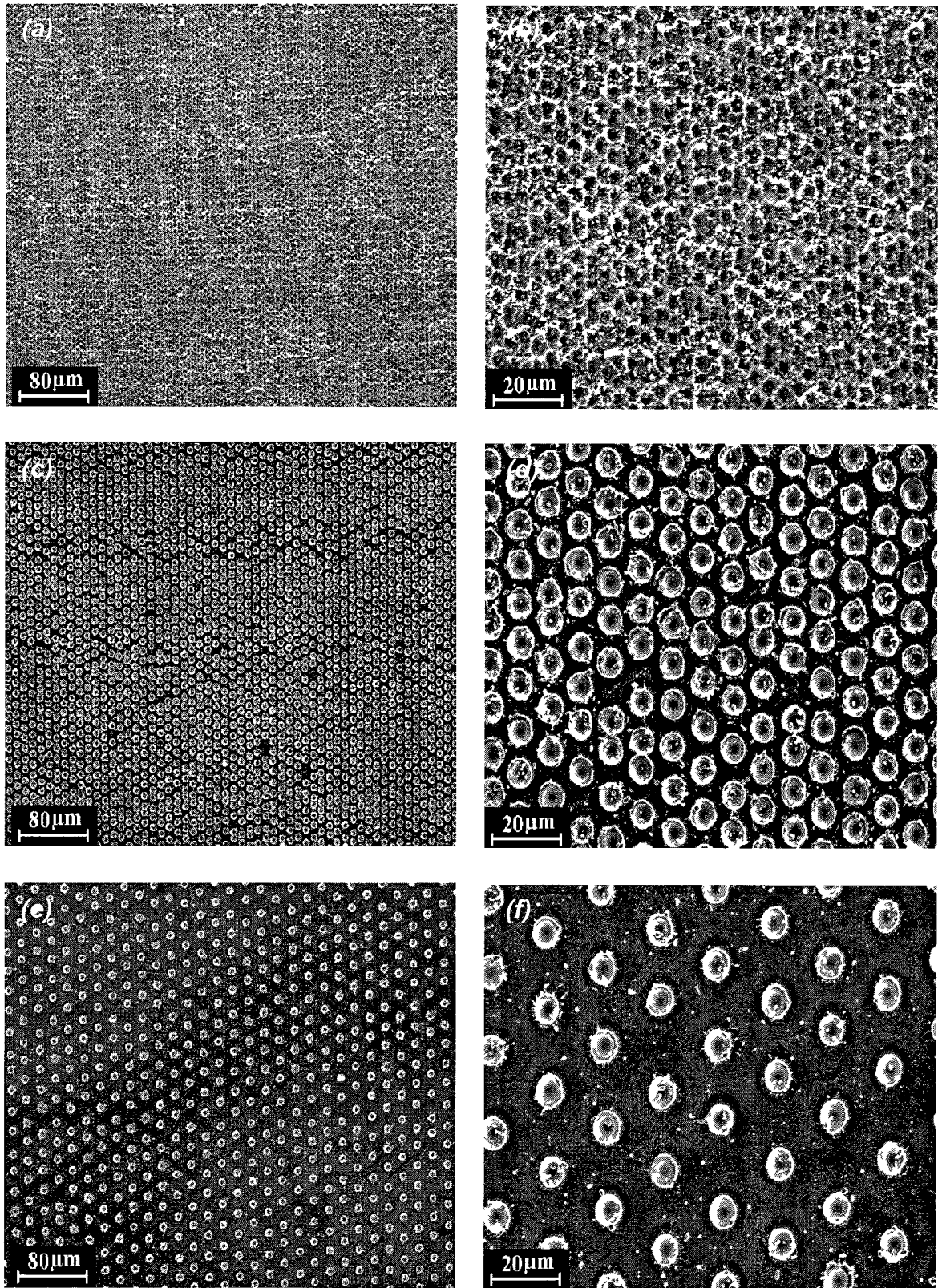


Fig 4-2 The SEM micrographs of samples (a) and (b) D5L5; (c) and (d) D5L10; (e) and (f) D5L20 after laser ablation process.

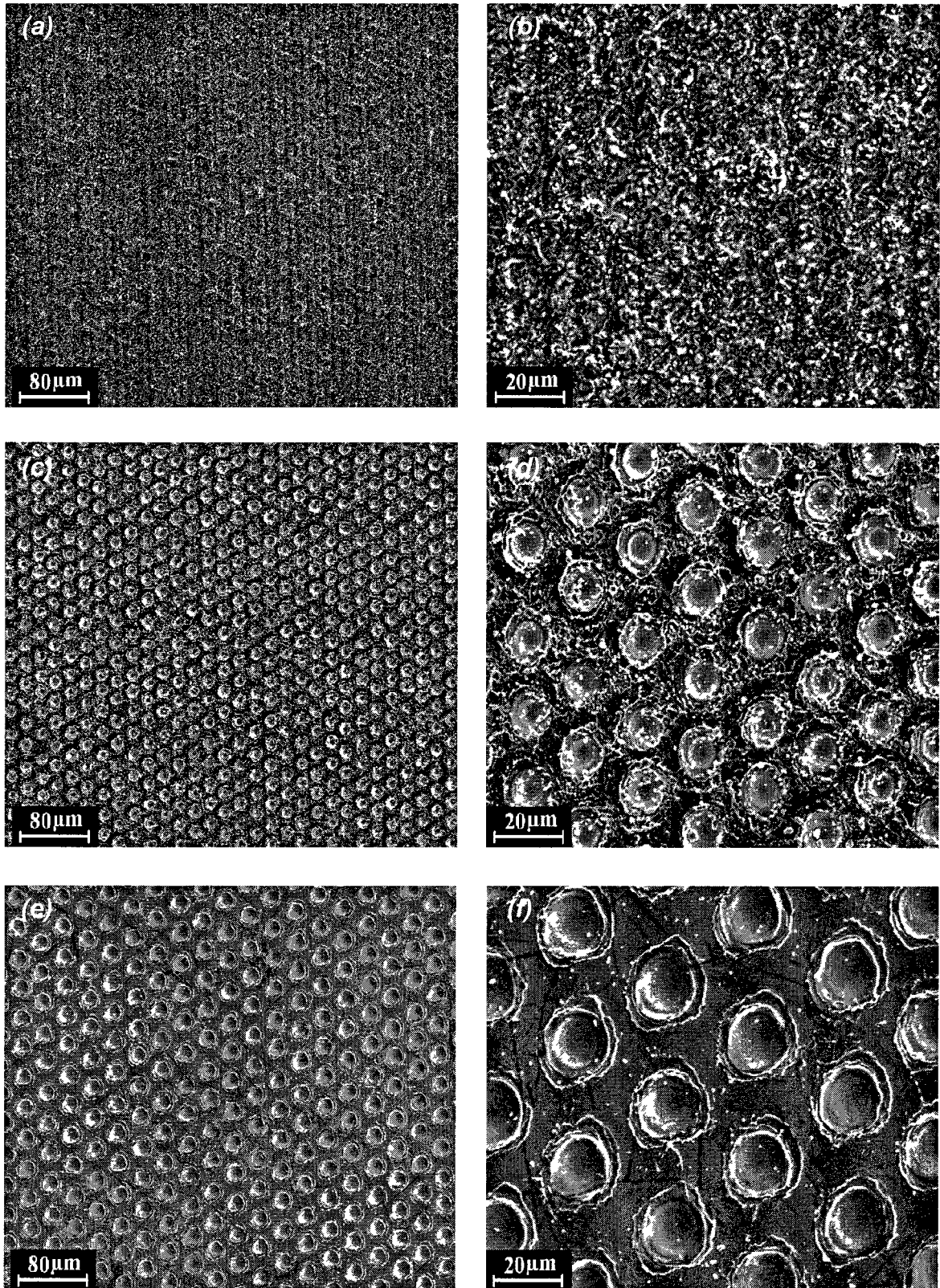


Fig. 4-3 The SEM micrographs of samples (a) and (b) D10L10; (c) and (d) D10L20; (e) and (f) D10L30 after laser ablation process.

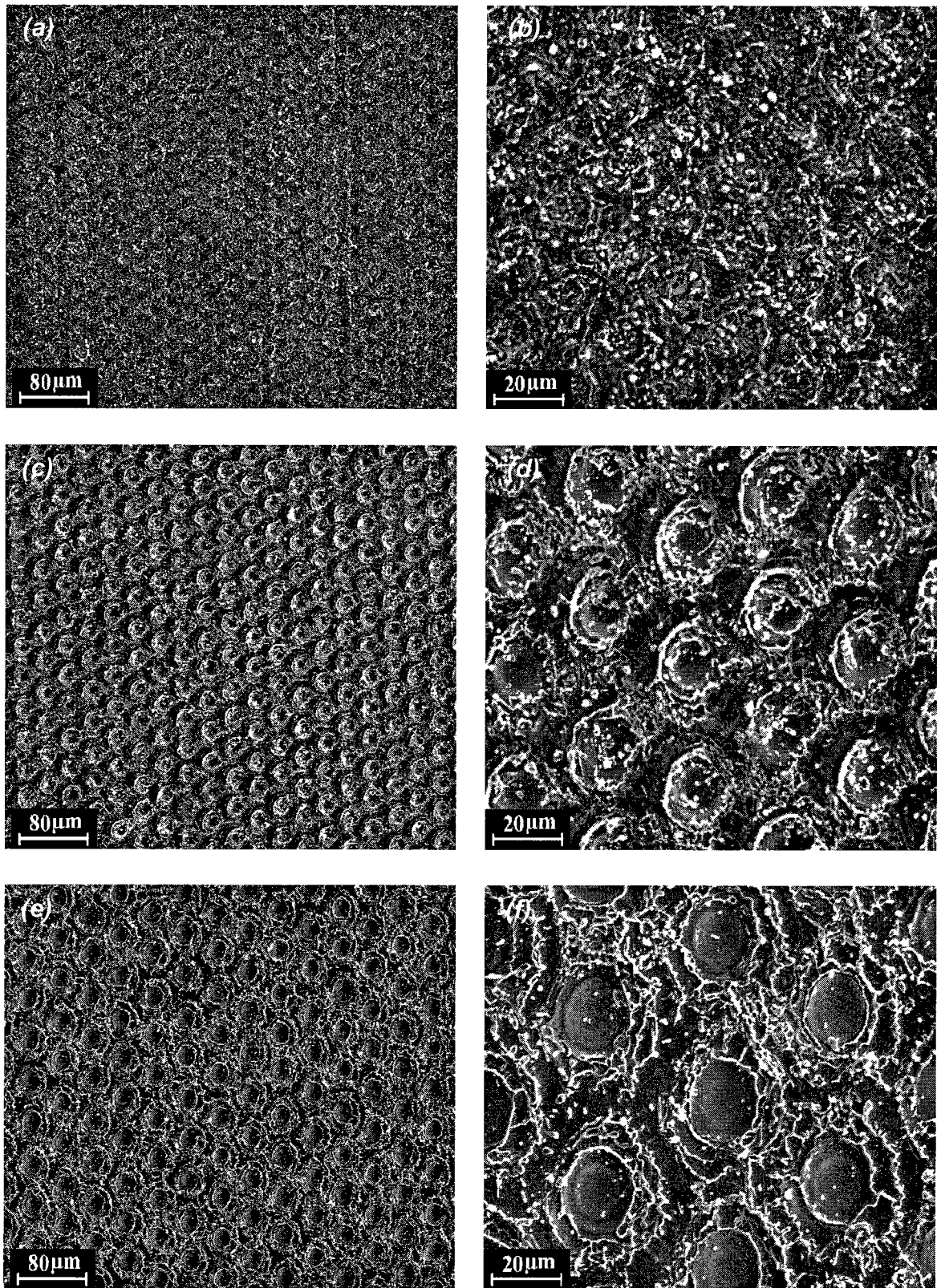


Fig. 4-4. The SEM micrographs of samples (a) and (b) D20L20; (c) and (d) D20L30; (e) and (f) D20L40 after laser ablation process.

4.2. EDS analysis of the patterned samples

Energy-dispersive x-ray spectrometry is perhaps the most useful elemental qualitative analytical tool. The technique can qualitatively identify elements from atomic number 11 to the end of the periodic table at levels from a few hundred nanograms in thin films to a few parts per million in bulk samples. The primary basis of the identification of elements in a sample is the energy and relative intensity of the K, L, or M spectral lines [58]. Fig. 4-5 (a) refers to sample REF. In this spectrum three elements, nickel (Ni), oxygen (O) and carbon (C) are observed. There are four peaks for Ni that show different X rays were scattered from different energy levels. The intensity of the most intense peaks (Ni: $L_{\alpha}=0.851$ and O: $K_{\alpha}=0.523$ KeV) was used to calculate the ratio of Ni/O (see the spectra). Other peaks refer to O and C. The origin of C can be the impurities that existed in the initial nickel sheet (as received). Oxygen's origin can be the impurities in the received nickel or oxidation during the laser ablation process. Anyhow a small amount of oxygen in the sample is predictable because of processing methods of metals or alloys. The EDS spectra of other samples are presented in Fig. 4-5 from (b) to (e). All samples have the same elemental peaks. The ratio of Ni/O is the same for the surface and inside the holes for all samples. These spectra prove that the chemical composition of samples did not change to any significant extent after the laser ablation process.

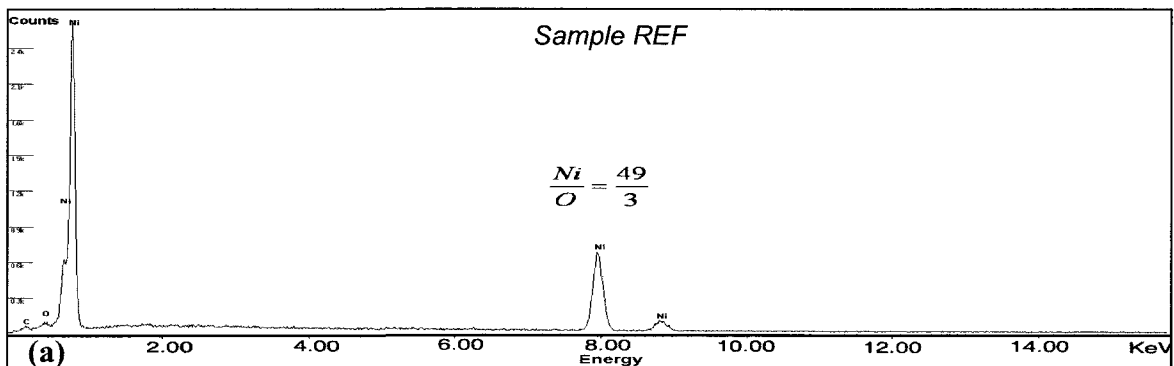
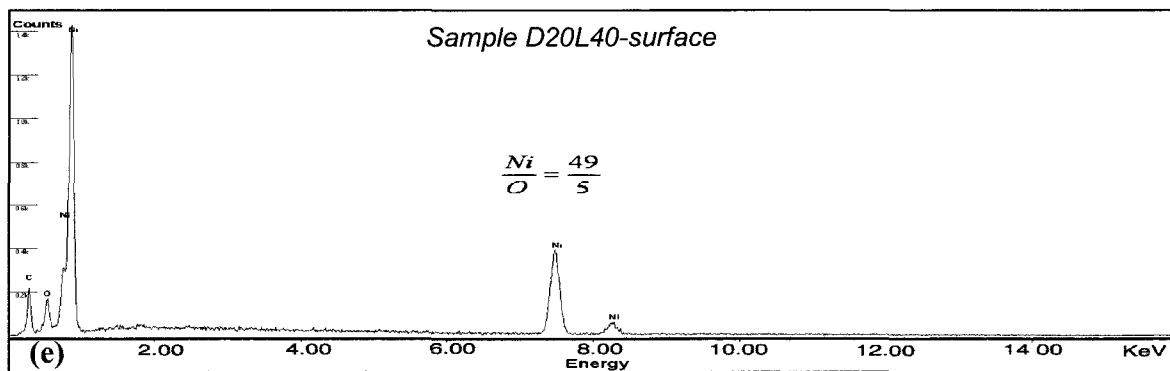
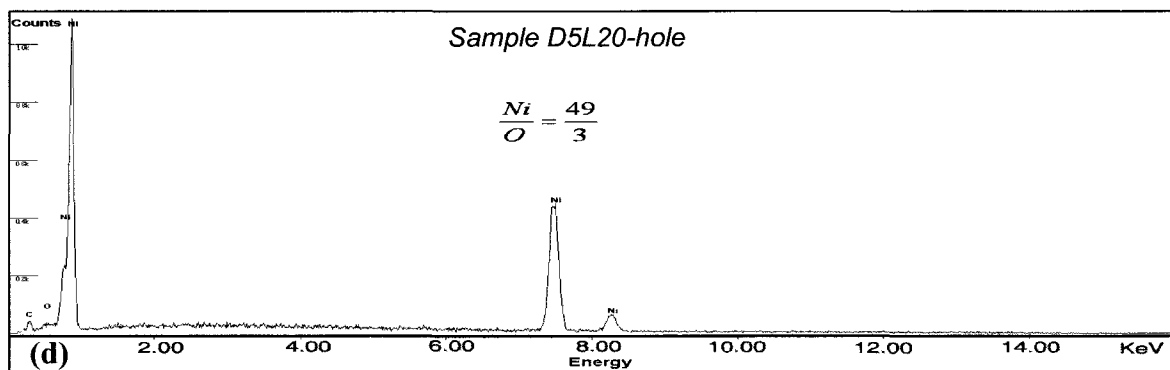
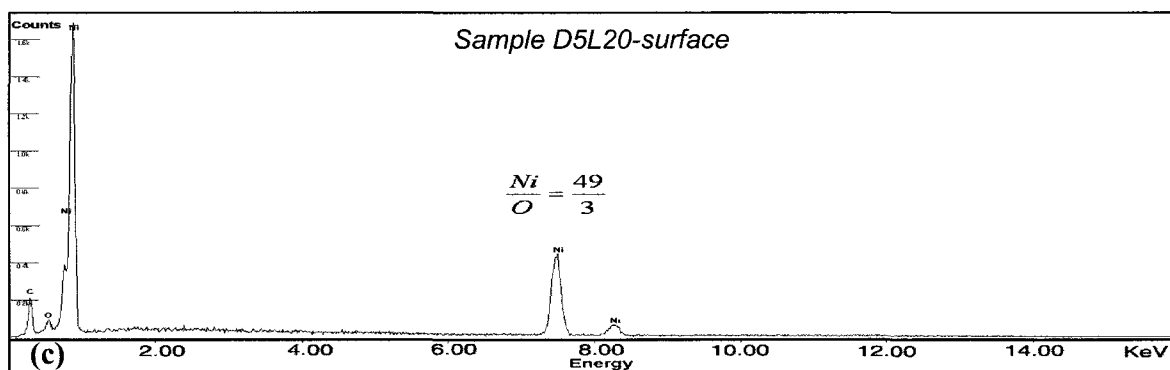
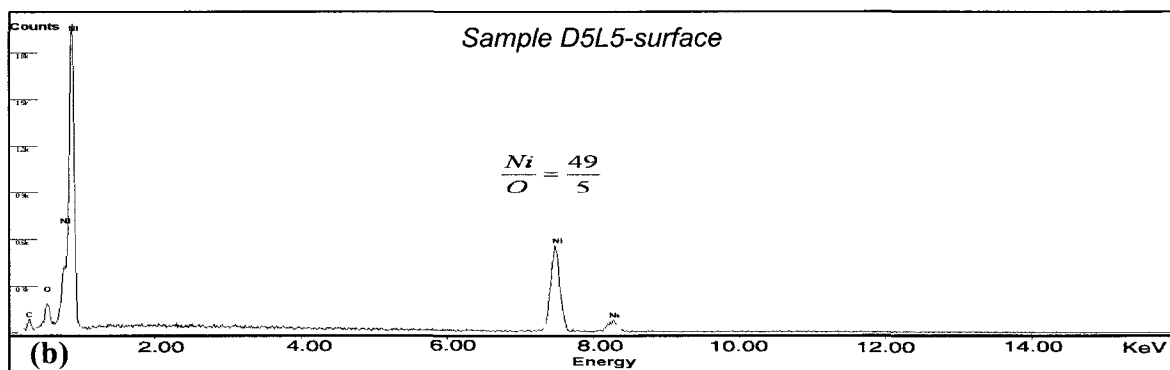


Fig. 4-5. EDS analysis spectra of samples (a) REF, (b) D5L5; surface, (c) D5L20; surface, (d) D5L20; hole, and (e) D20L40; surface (continued).



4.3. Roughness of the patterned samples

The profilometry test results for all samples are presented in Table 4-1. In addition, Figs. 4-6 to Fig. 4-10 shows the 3D roughness, X-profile, Y profile and histogram data for samples D5L5, D5L20, D10L20, D20L20 and D20L40.

Roughness parameters are as follows [59,60]:

Ra: average roughness

Rq: Root mean square roughness

Rt: Maximum peak to valley height

Rv: Maximum valley depth

Rp: Maximum peak height

Comparing all samples with $D=5\ \mu\text{m}$, shows that sample D5L10 had the highest roughness of all samples (see *Ra* value in both X and Y profiles in Table 4-1). Since in this research the goal was to decrease the contact area between the solution and the surface using a special surface pattern it seems reasonable to select a ratio related to areas of the holes and the overall surface. So, the ratio of the holes area to the overall surface area is proportional to $(D/L)^2$. Samples D5L5 and D5L20 are smoother than sample D5L10 [$(D/L)^2=0.25$]. Among samples with $D=10\ \mu\text{m}$, samples D10L20 [$(D/L)^2=0.25$] and D10L10 [$(D/L)^2=1$] are the roughest and the smoothest ones, respectively. In this set of samples it is seen that by increasing the hole distance the roughness increases. Generally the roughness of these samples is higher than that of samples with $D=5\ \mu\text{m}$ (compare values in the Table 4-1). In this set of samples, *Rt* values are higher than those of samples with $D=5\ \mu\text{m}$. To create larger holes more energy was used, as a result larger diameter holes are deeper than smaller diameter holes (compare *Rv* values in Table 4-1). However, there is one exception that *Rt* value of sample D5L10 is larger than that of sample D10L10. Samples with $D=20\ \mu\text{m}$ have the highest *Ra* amongst all samples. Sample D20L40 has the highest *Ra* value in all samples.

Fig. 4-6 shows the roughness data for sample D5L5. The histogram curve [Fig. 4-6 (d)] confirms that the average roughness of this sample is around zero and there is a normal distribution of roughness on the surface. The black curve is the

height distribution from the test and the red curve is the normal distribution of the black curve. The 3D roughness image and histogram of sample D5L20 [Fig. 4-7 (a) and (d)] is very similar to sample D5L5. A uniform roughness and normal distribution in histogram is observed. In X and Y profiles [Fig. 4-7 (b) and (c)] the distance between peaks and valleys are larger than that of sample D5L5 which is due to larger hole distance in sample D5L20. The histogram curve of sample D10L20 is a bit different from samples D5L5 and D5L20 [Fig. 4-8 (d)]. In this histogram it is possible to observe some points with height of around -1.75 or 1.6 μm but in samples D5L5 and D5L20 these heights were zero. This is because of higher roughness in this sample compared with samples D5L5 and D5L20. Sample D20L20 seems to be the same as sample D10L20 [Fig. 4-9]. In sample D20L20, the histogram curve has a normal distribution. The 3D roughness image of this sample does not show any hole clearly, which is the result of hole overlaps. The 3D roughness image of sample D20L40 depicts a uniform and well patterned surface on this sample [Fig. 4-10 (a)]. The histogram curve shows that the number of points with highest or lowest height is significant and the distribution is normal [Fig. 4-10 (d)].

Table 4-1. The roughness values from profilometry test for all samples

Sample codes	Roughness values									
	X profile (μm)					Y profile (μm)				
	Rq	Ra	Rt	Rp	Rv	Rq	Ra	Rt	Rp	Rv
D5L5	0.34	0.27	2.14	1.07	-1.07	0.32	0.25	2.02	1.00	-1.02
D5L10	0.58	0.48	3.06	1.27	-1.49	0.56	0.44	3.10	1.67	-1.42
D5L20	0.26	0.20	1.81	0.90	-0.91	0.26	0.20	1.70	0.81	-0.89
D10L10	0.37	0.30	2.28	1.16	-1.12	0.32	0.23	2.30	1.23	-1.07
D10L20	0.76	0.65	3.32	1.48	-1.84	0.68	0.56	3.27	1.54	-1.73
D10L30	0.64	0.52	3.51	1.72	-1.78	0.66	0.54	3.47	1.60	-1.86
D20L20	1.02	0.80	5.11	2.04	-3.07	0.86	0.70	4.03	1.47	-2.56
D20L30	0.95	0.73	5.87	3.24	-2.62	0.78	0.58	4.57	2.15	-2.41
D20L40	1.19	1.06	4.39	1.51	-2.88	1.14	0.96	4.3	1.5	-2.79

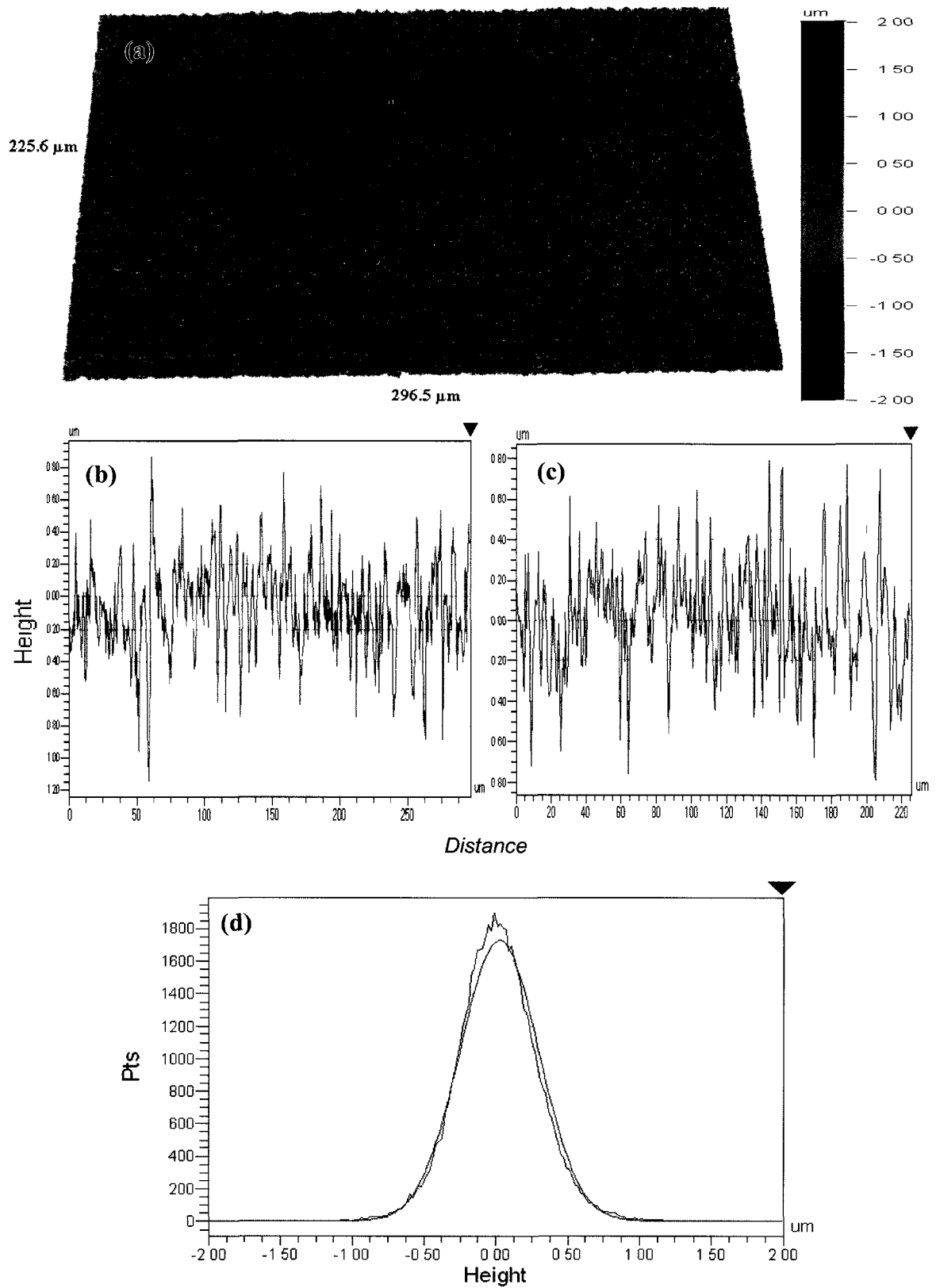


Fig. 4-6. Sample D5L5 (a) 3D roughness, (b) X-profile, (c) Y-profile and (d) histogram curve.

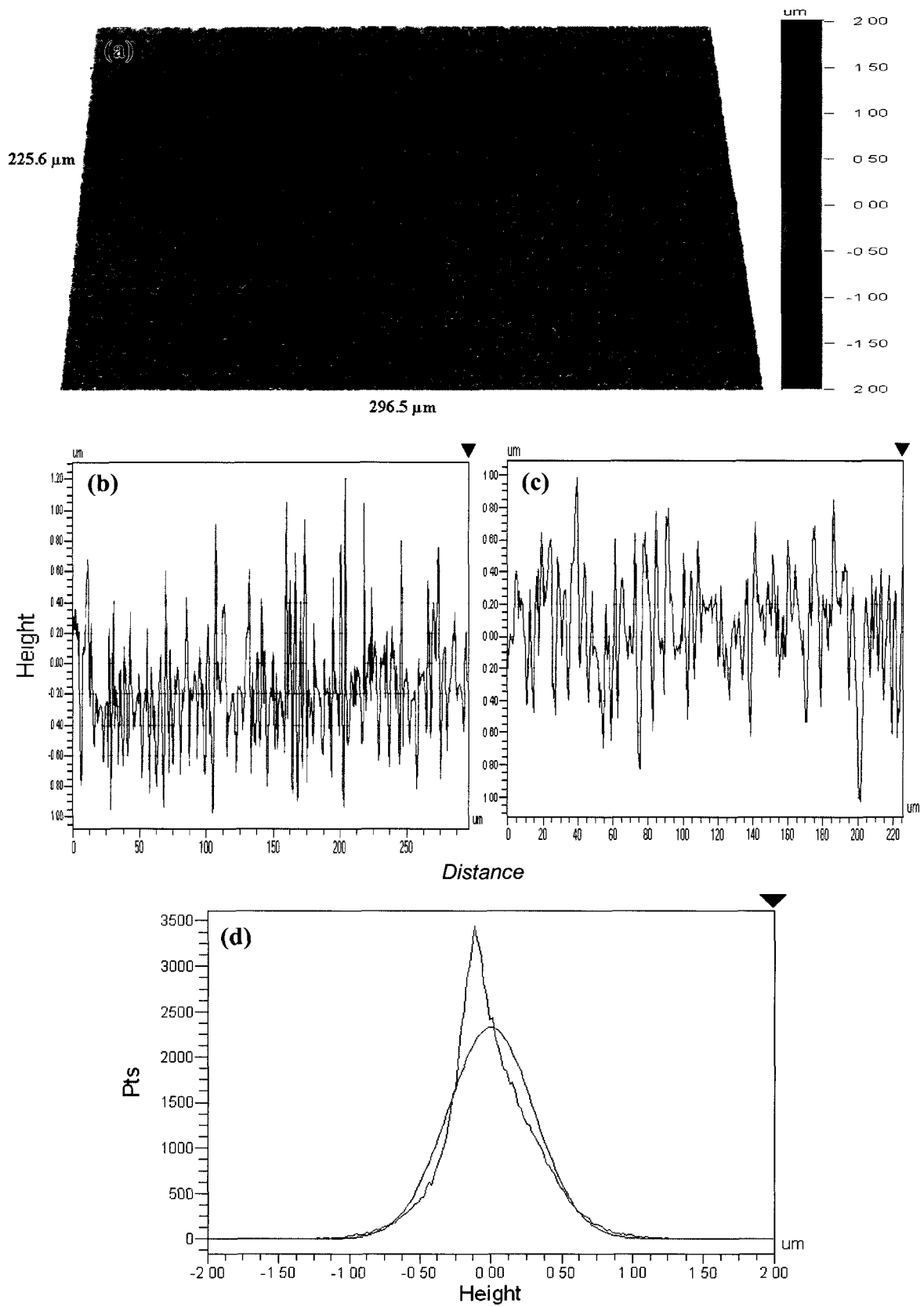


Fig. 4-7. Sample D5L20 (a) 3D roughness, (b) X-profile, (c) Y-profile and (d) histogram curve.

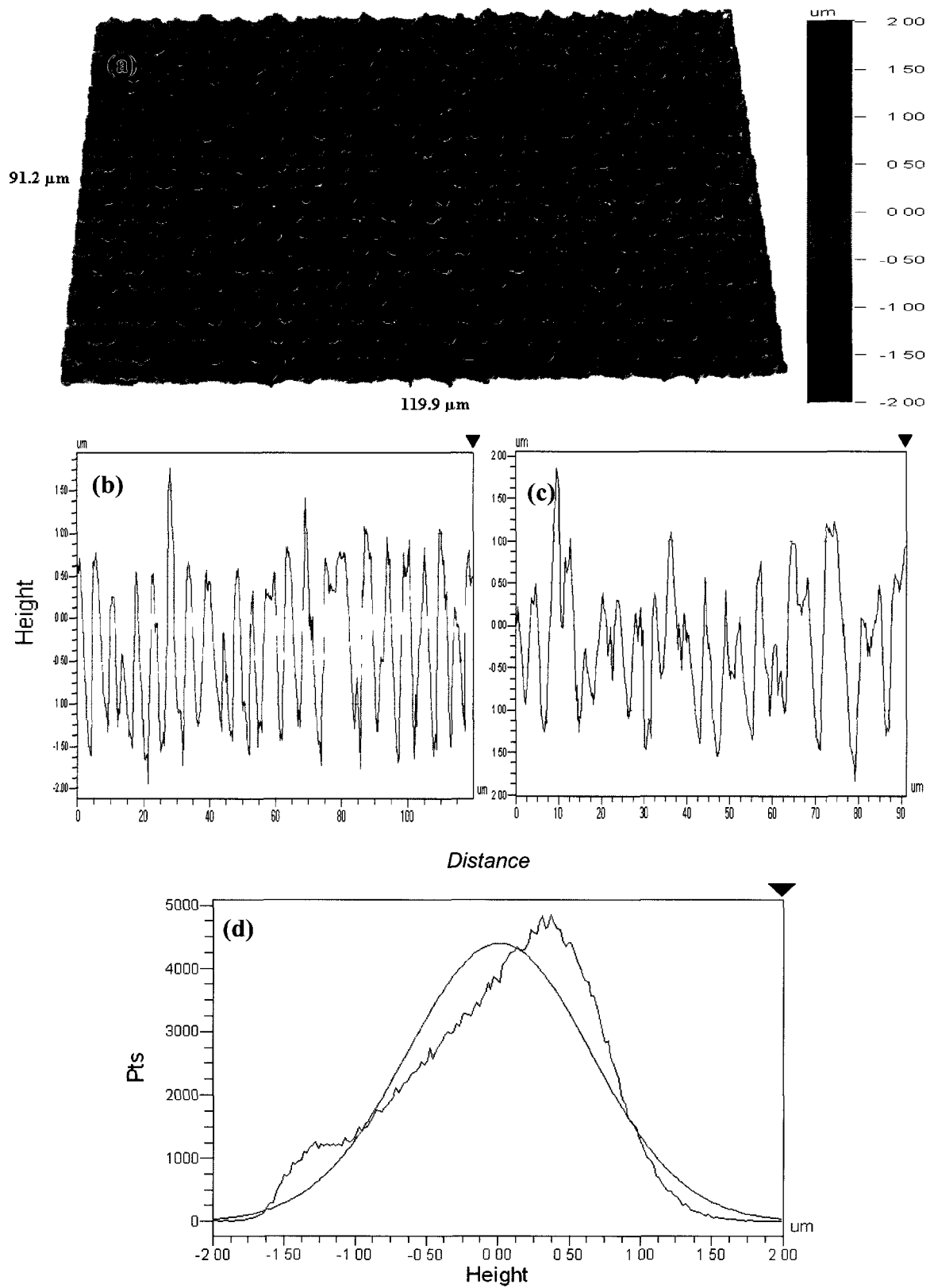


Fig. 4-8. Sample D10L20 (a) 3D roughness, (b) X-profile, (c) Y-profile and (d) histogram curve.

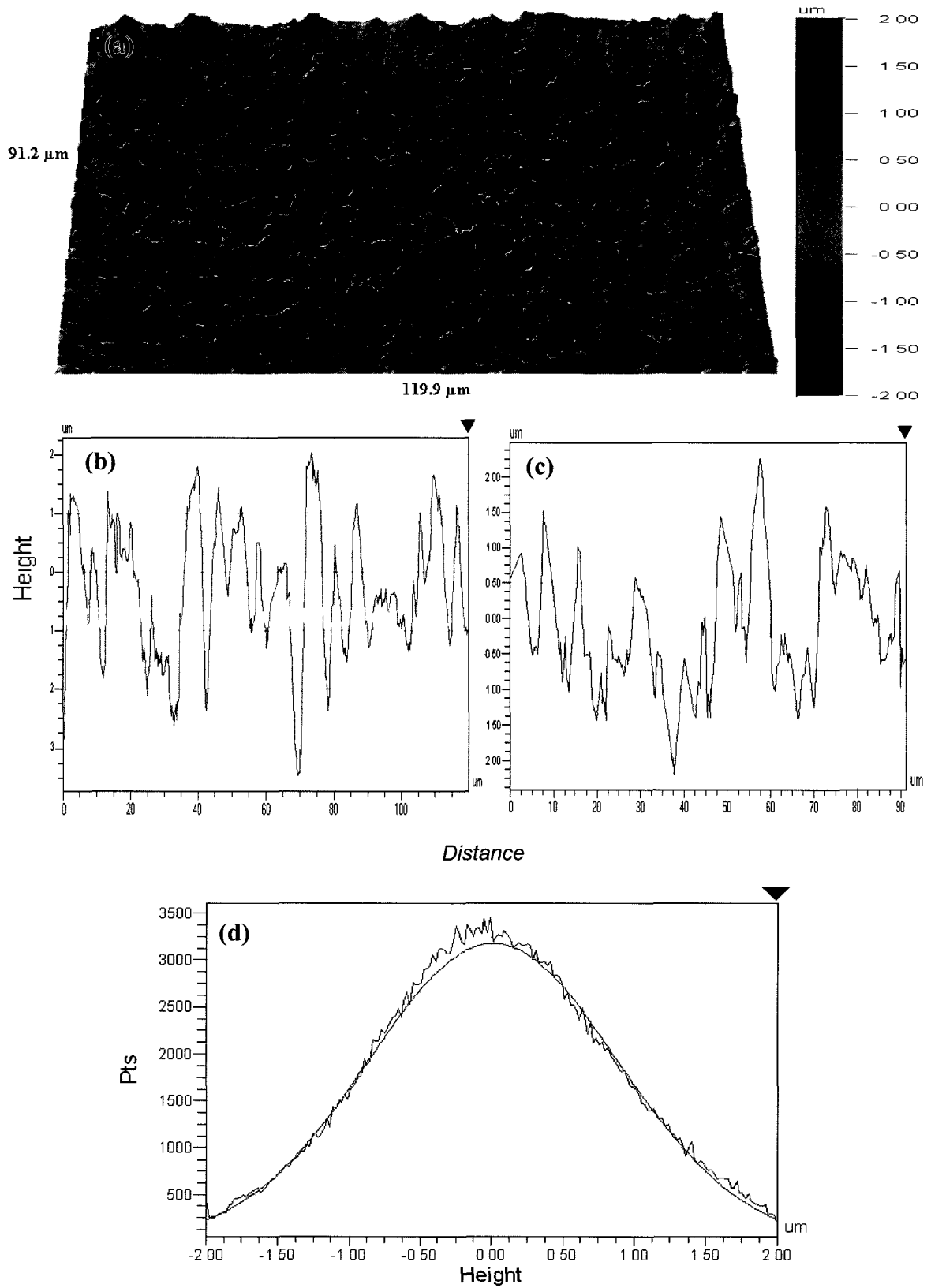


Fig. 4-9. Sample D20L20 (a) 3D roughness, (b) X-profile, (c) Y-profile and (d) histogram curve.

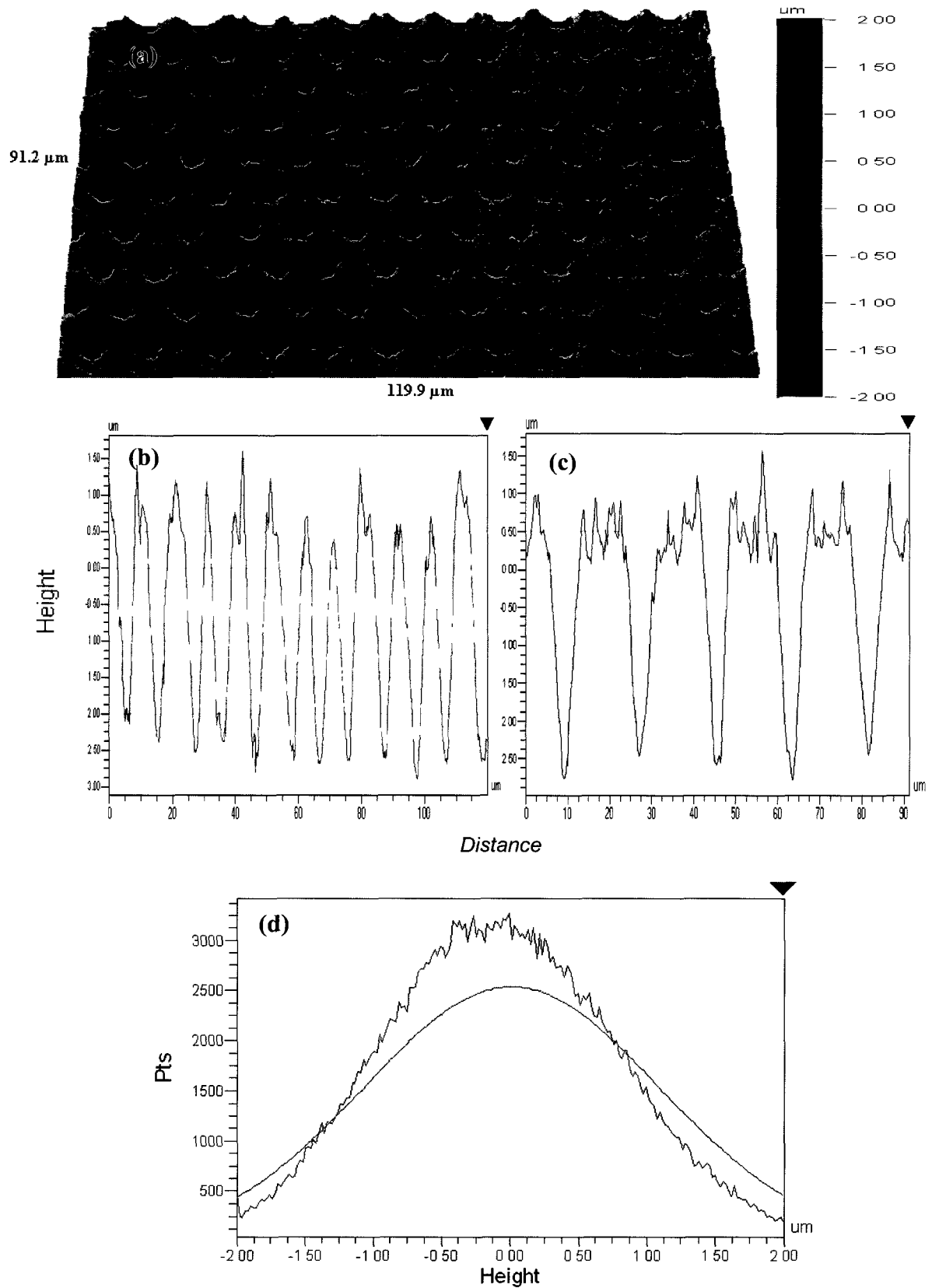


Fig. 4-10. Sample D20L40 (a) 3D roughness, (b) X-profile, (c) Y-profile and (d) histogram curve.

4.4. Corrosion tests

Tables 4-2 to 4-4 present the calculated corrosion data from each of the three corrosion tests. Fig. 4-11 shows the potentiodynamic corrosion curves of sample REF. Two tests were done on fresh samples to ensure repeatability of the conditions. It is observed that the cathodic and anodic sides of both curves are very similar and there is little difference between their corrosion potentials (E_{corr}) and corrosion current densities (I_{corr}). The main difference between these two REF samples is observed in the passive regions. In the first test the passive region ranges from 0.35 to 0.75 V but in the second test it ranges from 0.45 to 0.75 V. The reason is that in each corrosion test a fresh 0.5M H_2SO_4 was used, so the passive regions are slightly different.

Fig. 4-12 shows three corrosion curves of sample D5L5. The first test curve has a passive region approximately from 0.25 to 0.77 V. It seems that the passive layer became unstable around 0.90 V and the corrosion rate increased after this voltage. In the second test curve, the E_{corr} increased and the I_{corr} decreased (see Table 4-3) which is a sign of a stable layer's formed in the first test. The passive region in the second test was shorter and narrower (0.4-0.68 V) compared to the first one. The third test showed that corrosion rate is decreasing (lower I_{corr} and higher E_{corr}). However in the third test, it is observed that the surface of the sample was severely corroded compared to the previous tests and a corrosion resistant layer was deposited. Fig. 4-21 (a) shows the current density (I_{corr}) and polarization (R_p) values of three corrosion tests for sample D5L5. As I_{corr} decreased the polarization increased. This shows that there is an increase in corrosion resistance due to development of the corroded layer on the surface after the first test. Fig. 4-21 (b) shows that the E_{corr} is almost unchanged in the second and the third corrosion tests. Fig. 4-31 shows the surface of sample D5L5 after each corrosion test. The surface damage became worse after each corrosion test, the amount of corrosion is more and the corroded layer is probably thicker. So the layer protected the sample from further corrosion in the third test and the polarization resistance increased dramatically.

In sample D5L10, no passive region is observed during the first test (Fig. 4-13) but after the second test a short region was formed around 0.2 V which is probably a passive region. Finally, after the third test a stable passive region appeared in the curve and remained without any change up to the end of the test (see the third curve). It seems that in this sample's passive layer was formed later than that of sample D5L5 because in the second test the I_{corr} increased (but E_{corr} increased too) and after the third test the I_{corr} decreased compared with previous tests (see the related values in Tables 4-2 to 4-4).

Sample D5L20 differs from the other two in this set of samples (Fig. 4-14). In this sample there is a passive region in both first and second tests. The cathodic and anodic slopes are very similar in both curves. In the first test a passive region was approximately formed between 0.3 and 0.63 V and then the curve went through a transpassive region and the corrosion rate increased. In the second test, the passive region had some fluctuations or instabilities. Probably, in this region the passive layer was frequently broken and re-passivated, so the E_{corr} and I_{corr} are fluctuating on that region. The E_{corr} and I_{corr} are close to each other in both tests (Tables 4-2 and 4-3). In the third test, many fluctuations were observed in the cathodic to anodic transient area which is most probably due to a stable passive layer formed in the past tests. This layer caused a significant decrease in the I_{corr} (Table 4-4). Fig. 4-22 (a) shows the I_{corr} and R_p from three corrosion tests for sample D5L20. In these curves the I_{corr} is decreasing and R_p is increasing which is the expected behavior. I_{corr} did not change greatly in the first two corrosion tests and the R_p increased slightly, but after the third test the magnitude of I_{corr} decreased and R_p increased significantly which is due to a stable passive layer in the third test (SEM images show the changing trend, Fig. 4-33). Fig. 4-22 (b) confirms that corrosion started sooner in the third test. This is because the surface was corroded from previous tests and it was susceptible to be corroded sooner, but the I_{corr} is low because there was a passive layer on the surface coming from previous tests.

Fig. 4-15 shows the corrosion curves for sample D10L10. Generally in this sample the E_{corr} remained almost constant and the I_{corr} decreased. As

observed, there is a passive region in both first and second tests around 0.85 V. This passive region is more extended in the second test and it seems the passivity stabled up to the end of the test. In the third test, the I_{corr} decreased remarkably but because of the curve shape it was not possible to calculate the real value.

Sample D10L20 (Fig. 4-16) has some similarity with sample D5L10 in terms of the passive region. In both samples, no passive region is observed in the first test. In the second test there are many fluctuations in the curve and it can be concluded that it resembles a passive region but its shape differs from the other samples and common passive regions. If it was a passive layer, most likely the layer was not stable enough and as a result in the third test, the magnitude of I_{corr} increased significantly.

Sample D10L30 shows that after each corrosion test the sample became more resistant to corrosion (Fig. 4-17). In this sample, the passive region was present in the second test. The I_{corr} slightly decreased between 0.42 to 0.58 V, however, the decrease was not large. In fact, it seems that the passive layer did not remain as stable as in other tests. In the third test the curve looks like the second curve of sample D10L20 with many fluctuations. In this case calculation of the I_{corr} was not possible due to the curve shape.

The corrosion curves of sample D20L20 are plotted in Fig. 4-18. The first curve shows a stable and long passive region from 0.0 V up to the test finish. In this region the I_{corr} is constant or decreasing. This condition is favorable for corrosion resistance. After the second test, it is observed that the I_{corr} decreased by about two orders of magnitude and the E_{corr} was unchanged compared with the first test values (Tables 4-2 and 4-3). It is worth mentioning that the I_{corr} of the first test ($0.4076 \mu\text{A}/\text{cm}^2$) was lower (better) than that of sample REF ($0.5141 \mu\text{A}/\text{cm}^2$). In the third test, it is thought that the passive layer did not have a protective property as in previous tests and, as a result, I_{corr} increased (Table 4-3).

Sample D20L30 had a very similar corrosion behavior to sample D10L20 (Fig. 4-19). In the first test there was no passive region and the magnitude of I_{corr} was

relatively high. In the second test the magnitude of I_{corr} dramatically decreased and the cathodic and anodic sides showed considerable fluctuations. In this curve, no corrosion parameters were obtained but it is evident that the magnitude of current density was very low. In the third test the corrosion rate increased. This is probably because any instability on the corroded surface can accelerate the corrosion rate.

Sample D20L40 had the best corrosion behavior after the first test of all the samples. Fig. 4-20 presents the corrosion curves for this sample. There is a shift in both cathodic and anodic sides of the first curve. In the anodic side the curve moved almost vertically after that shift (around -0.2 V) and a passive-like region was formed which was stable to the test finish. The I_{corr} was the lowest ($0.03 \mu\text{A}/\text{cm}^2$) of all samples and even better than sample REF. However, the E_{corr} was not the most noble (the highest). After the second test the sample still had a very good combination of I_{corr} and E_{corr} (Table 4-2). Finally after the third test I_{corr} increased but E_{corr} remained almost constant. No passive region was obtained in the third test. Fig. 4-23 (a) shows the I_{corr} and R_p values for all corrosion tests. After the first test, the I_{corr} and R_p increased. Usually the R_p value changes inversely with I_{corr} . This means that if I_{corr} increases, R_p decreases and vice versa. In this sample after the first test both values (I_{corr} and R_p) increased. The reason could be that some other factors such as the Tafel slopes affect R_p (see Eq. 3-1). However, after the third test, I_{corr} increased significantly and R_p decreased dramatically which shows the expected trend. So, it can be said that the passive layer formed in the first corrosion test, was stable in the second test because the magnitude of I_{corr} and E_{corr} [Fig. 4-23 (b)] only slightly changed, but after the third corrosion test the surface was severely damaged. SEM images (Fig. 4-39) show this process visually.

Table 4-2. The corrosion data for all samples after the first test

Sample codes	β_a (mV)	β_c (mV)	I_{corr} ($\mu A/cm^2$)		E_{corr} (mV)		R_p ($\Omega \cdot cm^2$)	
			Value	Rank	Value	Rank	Value	Rank
REF	45.5	-294	0.5141	3	-90.8	1	32956.8	4
D5L5	89.9	-158.9	16.56	9	-295.10	6	1507.5	9
D5L10	123.6	-157.8	6.976	6	-307.5	9	4319.8	7
D5L20	160.6	-118.2	0.6153	4	-262.8	4	48112.2	3
D10L10	111.6	-348.2	62.51	10	-200.5	2	587.8	10
D10L20	201.9	-204.9	7.3	7	-312.4	10	6056.8	6
D10L30	131.1	-149.2	6.191	5	-306.2	8	6594.7	5
D20L20	115.9	-78.6	0.4076	2	-305.7	7	49960.2	2
D20L30	101.9	-293.5	11.49	8	-262.7	3	2705.0	8
D20L40	85.7	-100.8	0.030	1	-280.6	5	671295	1

Table 4-3. The corrosion data for all samples after the second test

Sample codes	β_a (mV)	β_c (mV)	I_{corr} ($\mu A/cm^2$)		E_{corr} (mV)		R_p ($\Omega \cdot cm^2$)	
			Value	Rank	Value	Rank	Value	Rank
REF	-	-	-	-	-	-	-	-
D5L5	58.2	-179.4	0.340	3	-154.2	1	56194.2	4
D5L10	-	-	-	-	-	-	-	-
D5L20	68.1	-180.1	0.379	4	-182.7	2	56640.8	3
D10L10	110.3	-164.8	0.781	6	-242.7	3	36784.3	6
D10L20	-	-	-	-	-	-	-	-
D10L30	128.5	-130.5	0.746	5	-295.5	6	37735.2	5
D20L20	132.1	-187.0	0.006	1	-288.0	5	5609685	1
D20L30	-	-	-	-	-	-	-	-
D20L40	260.2	-275.6	0.048	2	-283.2	4	1212312	2

Table 4-4. The corrosion data for all samples after the third test

Sample codes	β_a (mV)	β_c (mV)	I_{corr} ($\mu A/cm^2$)		E_{corr} (mV)		R_p ($\Omega \cdot cm^2$)	
			Value	Rank	Value	Rank	Value	Rank
REF	-	-	-	-	-	-	-	-
D5L5	200.2	-260.4	0.032	2	-159.7	1	969872	2
D5L10	61.5	-183.4	0.218	3	-199.5	3	85368.4	4
D5L20	41.3	-280.5	0.01	1	-325.6	6	1655197	1
D10L10	-	-	-	-	-	-	-	-
D10L20	101.7	-264.0	0.268	4	-265.6	4	89338.7	3
D10L30	-	-	-	-	-	-	-	-
D20L20	278.5	-300.7	1.327	7	-328.7	7	33479.2	6
D20L30	73.3	-202.4	0.396	5	-183.2	2	58417.7	5
D20L40	108.7	-262.1	1.155	6	-273.9	5	22756.2	7

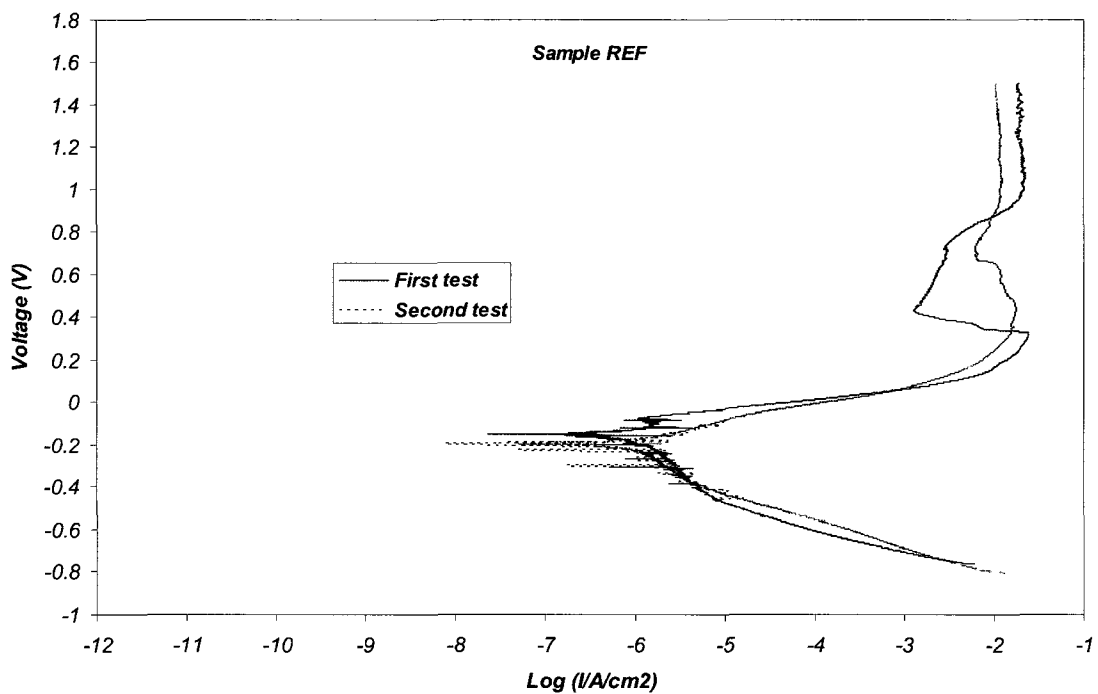


Fig. 4-11. Potentiodynamic corrosion curves for sample REF in 0.5M H₂SO₄.

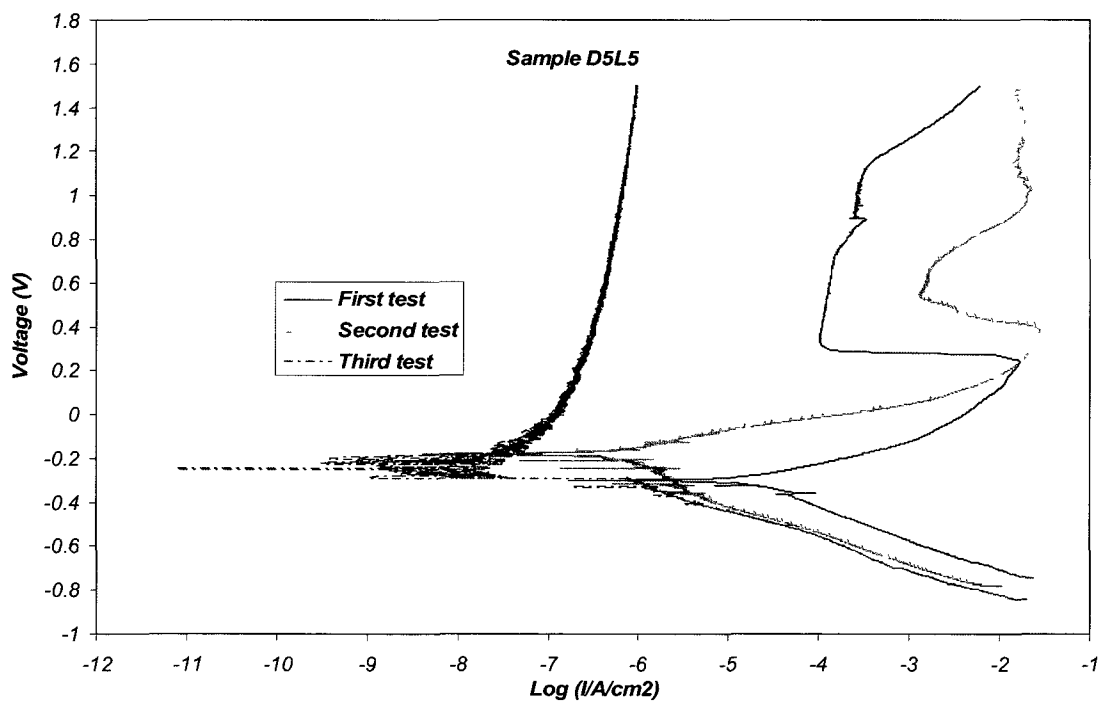


Fig. 4-12. Potentiodynamic corrosion curves for sample D5L5 in 0.5M H₂SO₄ after different tests.

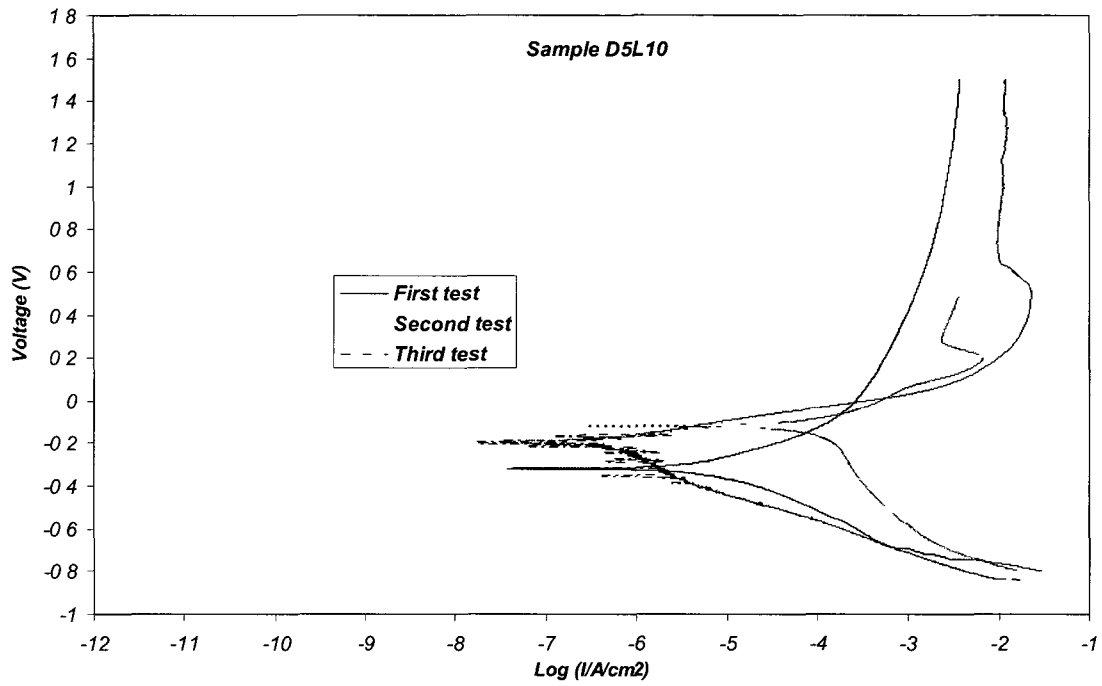


Fig. 4-13. Potentiodynamic corrosion curves for sample D5L10 in 0.5M H₂SO₄ after different tests.

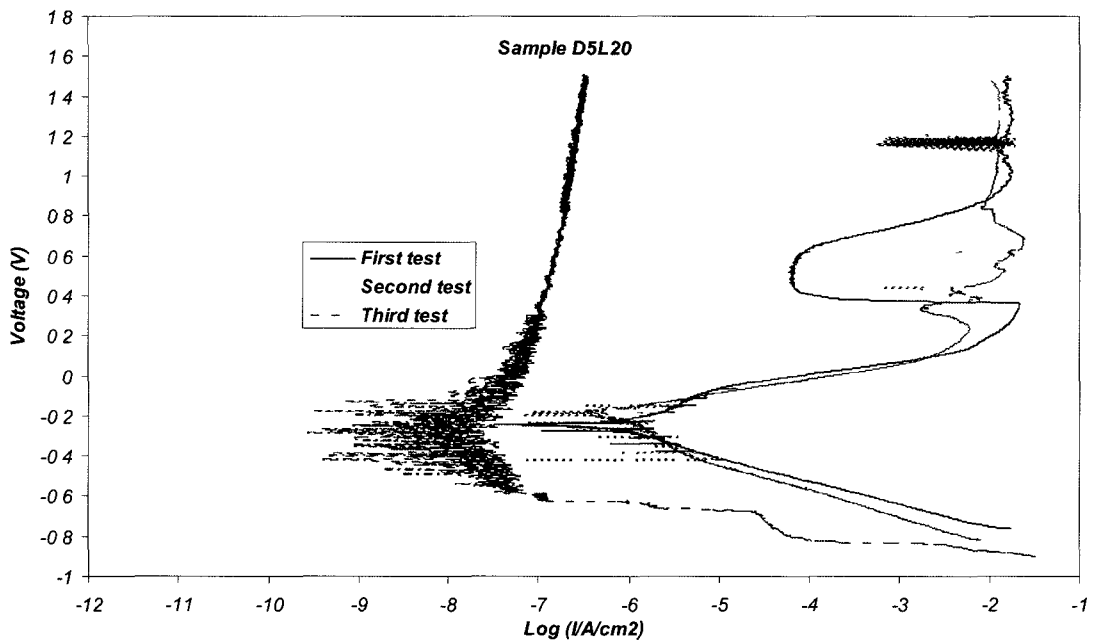


Fig. 4-14. Potentiodynamic corrosion curves for sample D5L20 in 0.5M H₂SO₄ after different tests.

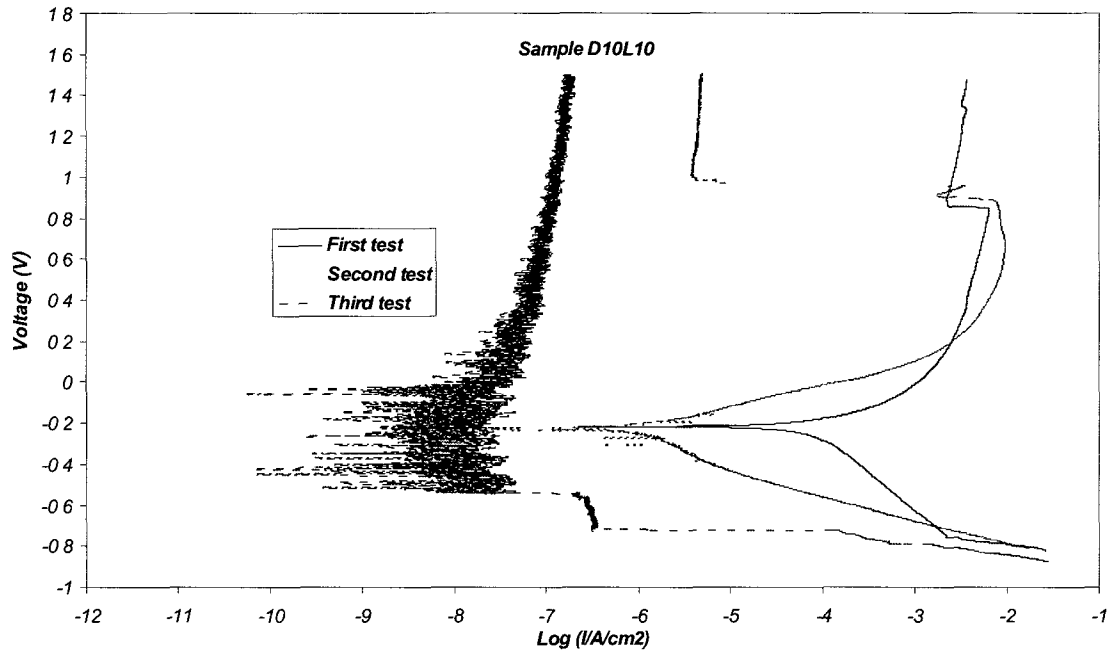


Fig. 4-15. Potentiodynamic corrosion curves for sample D10L10 in 0.5M H₂SO₄ after different tests.

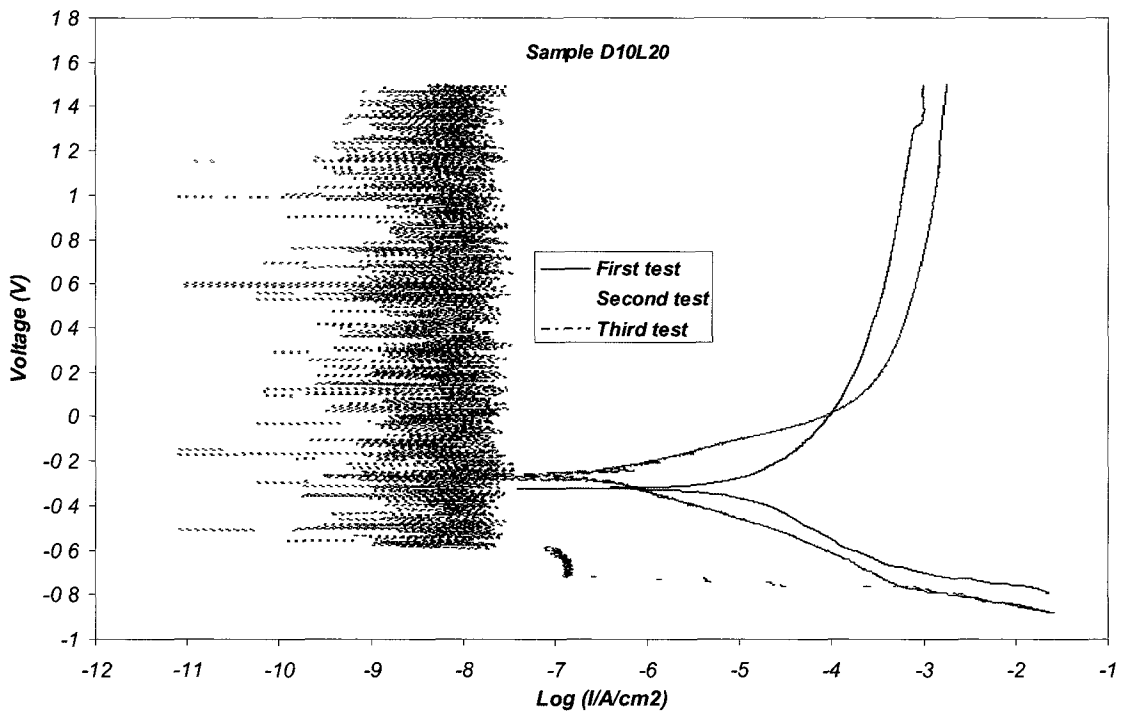


Fig. 4-16. Potentiodynamic corrosion curves for sample D10L20 in 0.5M H₂SO₄ after different tests

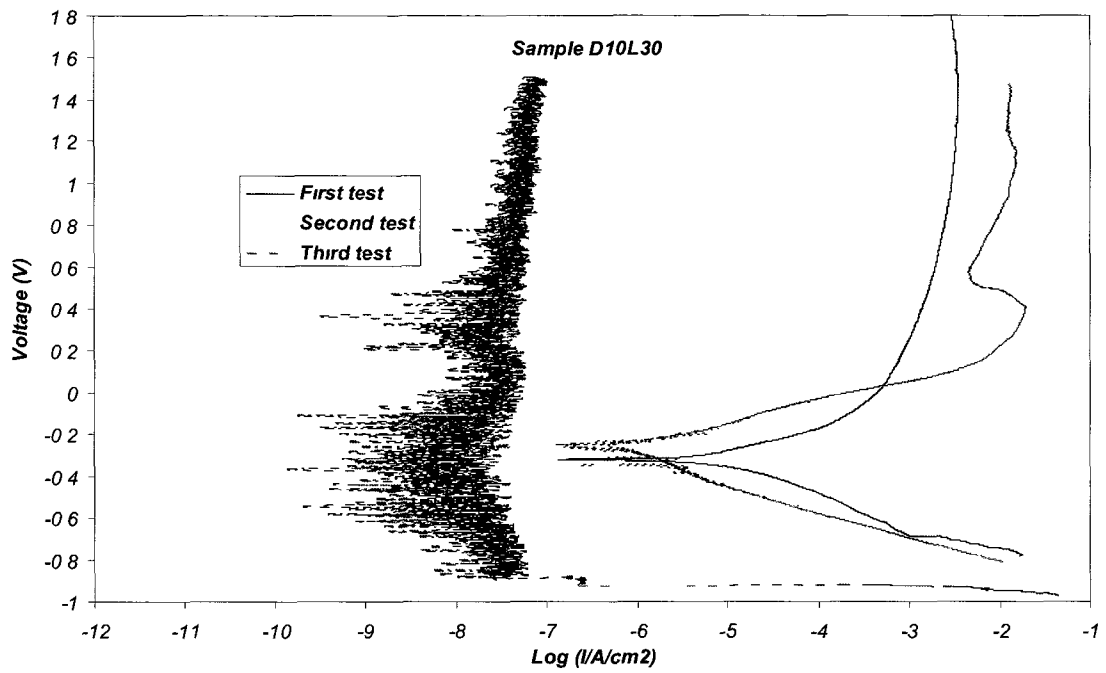


Fig. 4-17. Potentiodynamic corrosion curves for sample D10L30 in 0.5M H₂SO₄ after different tests.

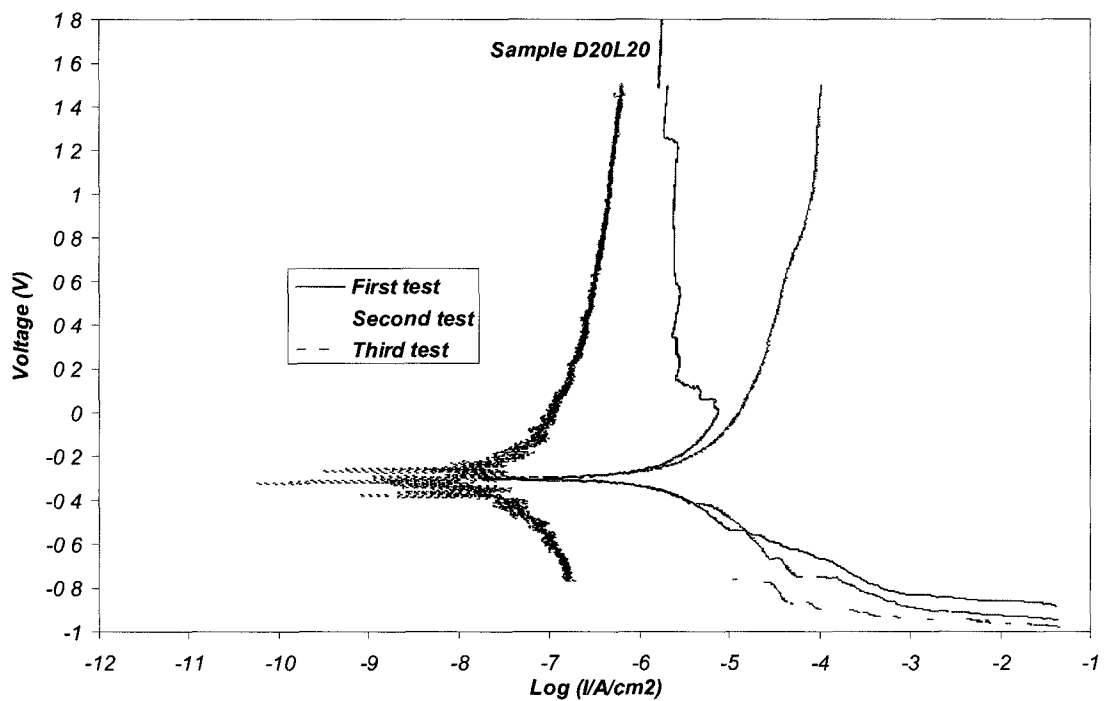


Fig. 4-18. Potentiodynamic corrosion curves for sample D20L20 in 0.5M H₂SO₄ after different tests

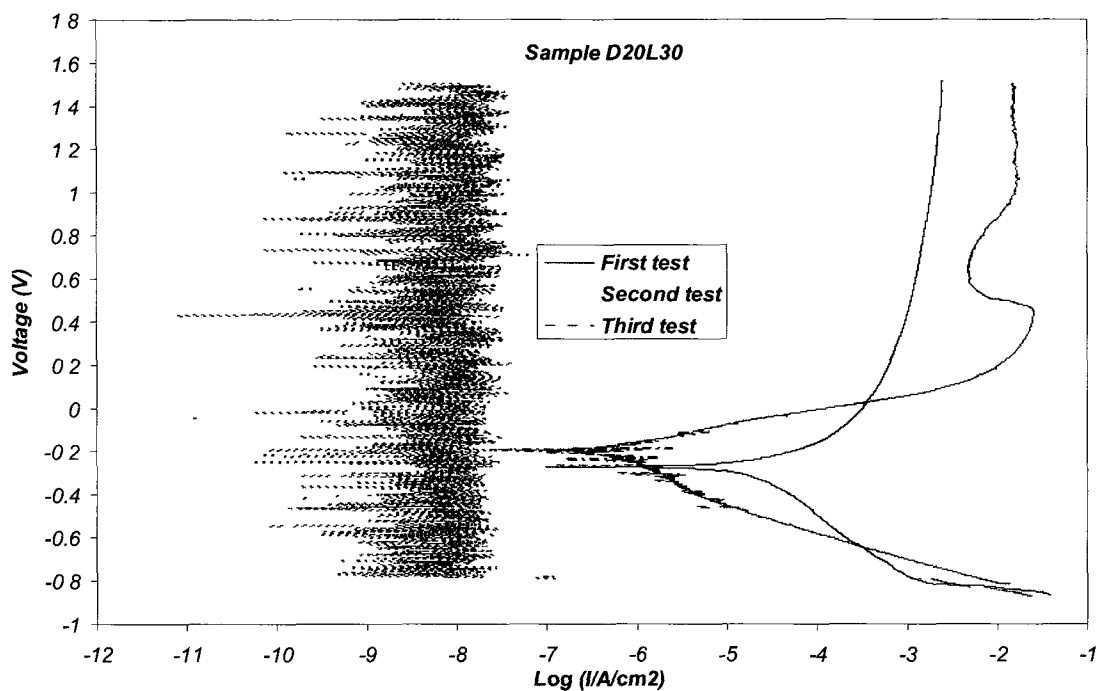


Fig. 4-19. Potentiodynamic corrosion curves for sample D20L30 in 0.5M H_2SO_4 after different tests.

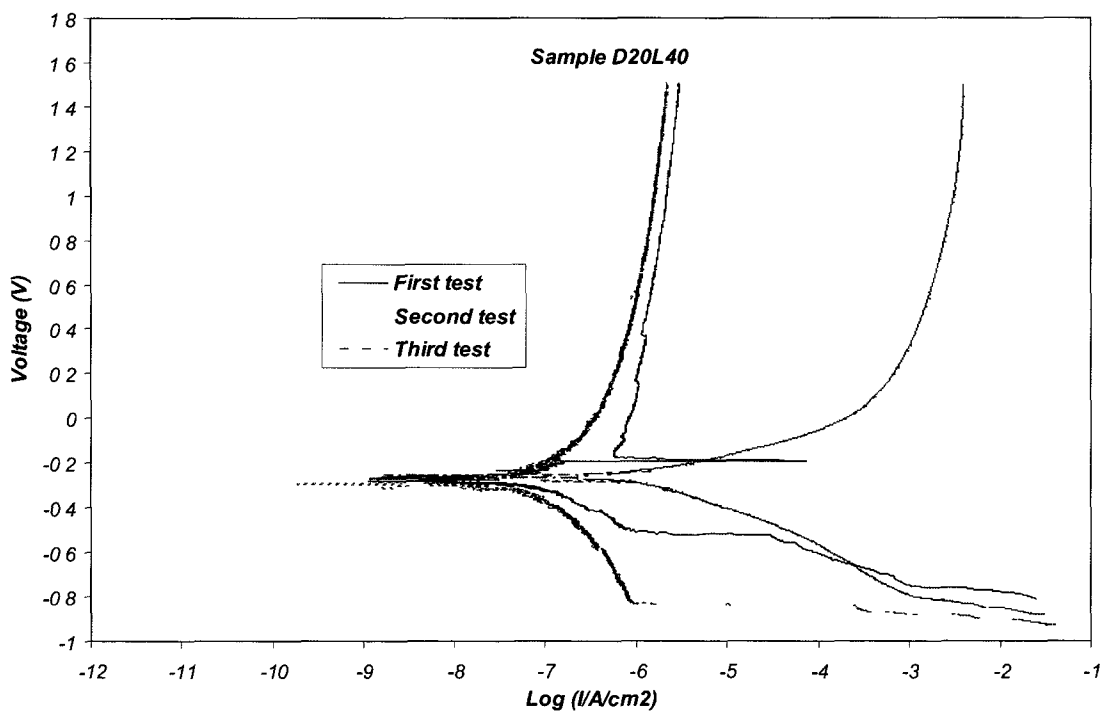


Fig. 4-20. Potentiodynamic corrosion curves for sample D20L40 in 0.5M H_2SO_4 after different tests.

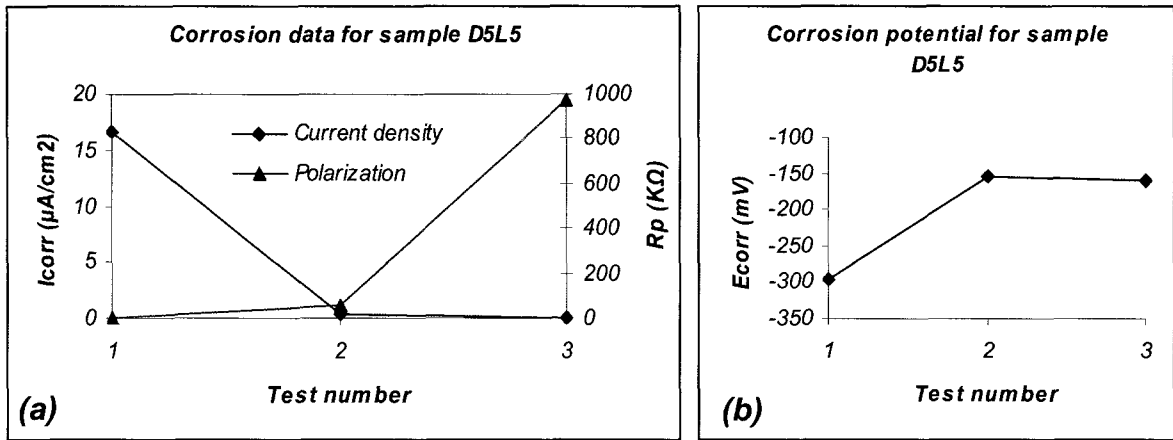


Fig. 4-21. Corrosion data of sample D5L5 (a) Icorr and Rp curves, (b) Ecorr curve.

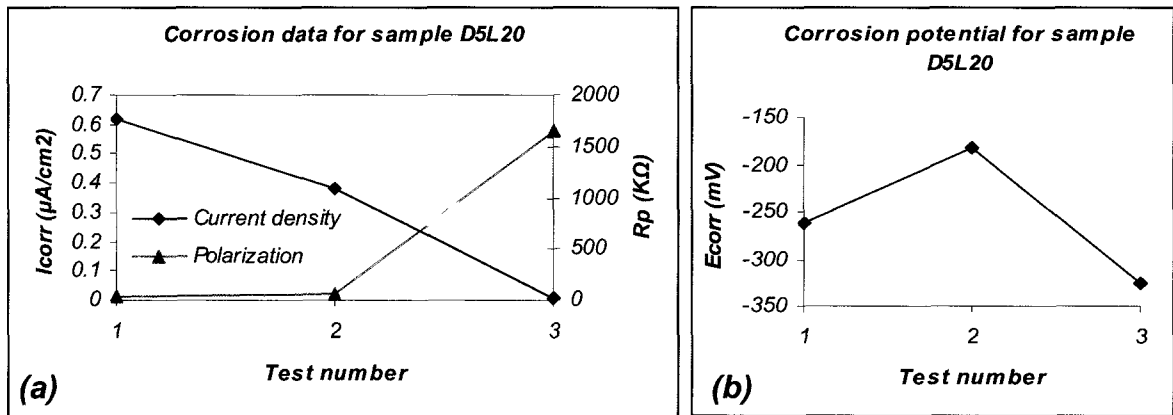


Fig. 4-22. Corrosion data of sample D5L20 (a) Icorr and Rp curves, (b) Ecorr curve.

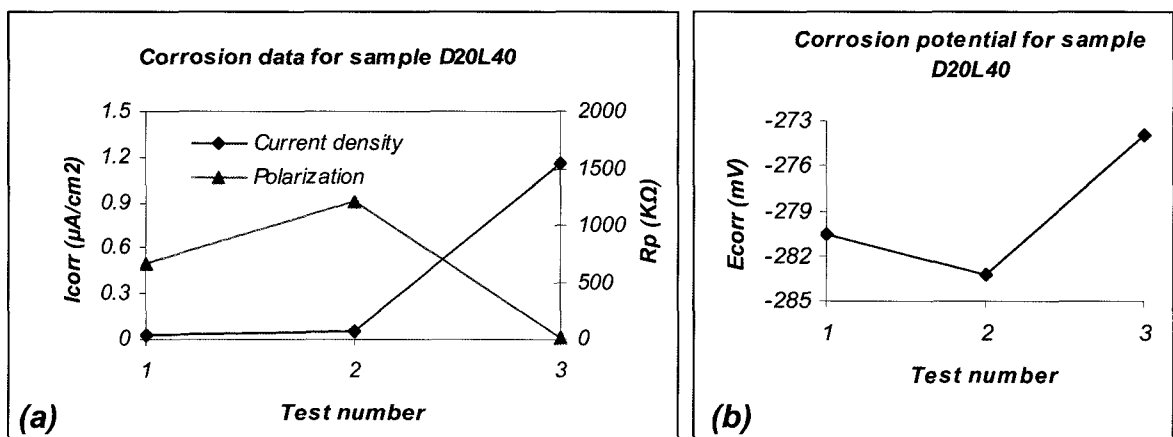


Fig. 4-23. Corrosion data of sample D20L40 (a) Icorr and Rp curves, (b) Ecorr curve.

Table 4-5 ascendingly ranks I_{corr} values for all samples after the first test. In this table there are some ratios or parameters namely (Ra/D) , (Ra/D) and $(D/L)^2$ defined. These parameters have been defined because it is predicted that there is a dependency between the hole diameter, the hole distance between and the surface roughness. In addition, in other research [22,23,61] such parameters as the distance and height of surface pattern constituents (asperity height) have been studied. Those three ratios were defined to investigate the dependency of the I_{corr} and the E_{corr} on them. According to this ranking it can be concluded that there are two groups. First group includes samples D20L40 to D20L20 and the second one starts from sample D5L20 to sample D10L10. In both groups by increasing the $(D/L)^2$ parameter, I_{corr} also increases. In other words, by increasing the parameter the corrosion resistance is weakening. Fig. 4-24 can give more information about the mentioned trend. In this Figure I_{corr} was plotted versus hole diameter for the samples with the same ratio of $(D/L)^2=1$ with sample REF. It is observed that samples with $D=5$ and $20 \mu\text{m}$ had lower I_{corr} compared with sample with $D=10 \mu\text{m}$. The observed values in the graph shows that probably decreasing the hole size (D) less than $5 \mu\text{m}$ (toward nano scale size) or increasing the hole size larger than $20 \mu\text{m}$ can decrease I_{corr} further which is promising for corrosion resistance. If this is right, the hole size will be in the range of nanoscale (for smaller D) or in smooth or flat scale (for larger D). This trend is also seen for samples with $(D/L)^2=0.25$ (Fig. 4-25). Regarding $(D/L)^2$ ratio, there are two possibilities to have lower value. First increasing the hole distance (L) and second decreasing the hole diameter D . The former means going toward small scales such as nanoscale and the later induces a smooth surface.

Regarding Ra/D and Ra/D parameters, no constant trend is observed. This shows that the well known parameters characteristics for randomly distributed roughness do not represent artificially patterned surfaces. The better alternative is to consider other surface parameters such as D and L . Fig. 4-28 shows I_{corr} values versus roughness of samples before the corrosion tests. As seen, there is no clear trend between all samples and the curve is ascending or descending in different parts. Comparison between this curve and the $(D/L)^2$ ratio (Table 4-5)

confirms that the trend in I_{corr} values versus the ratio is more clear than that of roughness. In fact, for roughness no general conclusion can be made.

Table 4-6 descendingly ranks E_{corr} values for all samples after the first test. In this table there is no clear trend in the behavior of the defined parameters as E_{corr} increases. For example, from sample D10L10 to sample D5L20, $(D/L)^2$ parameter decreased and after that increased. This is repeated for other parameters as well. However, for samples with the same hole diameter (D) it is seen that by increasing Ra/D parameter the E_{corr} decreased (compare in Table 4-6). This means that the greater the roughness, the lower the corrosion potential. The only exception in this trend is sample D20L40 which has higher E_{corr} . Fig. 4-29 shows all E_{corr} values versus the roughness of initial samples before the corrosion tests. Although there is no ascending or descending trend, the E_{corr} values are decreasing as roughness increases. This is in good agreement with previous finding of other researchers [24-26]. However, it is obvious the roughness can not be the only factor to affect the E_{corr} value. For example, sample D10L10 has higher (better for corrosion resistance) E_{corr} compared to sample D5L5, while it is rougher. In both samples, the D and L values are different and it seems they have a significant effect on the E_{corr} value. Figs. 4-26 and 4-27 present the E_{corr} of samples with $(D/L)^2=1$ and $(D/L)^2=0.25$, respectively. A comparison between these curves confirms that for samples with $(D/L)^2=0.25$, E_{corr} values are in good agreement with the relevant I_{corr} values (Fig. 4-25). It means that the sample which had the lowest I_{corr} showed the highest E_{corr} . This is the best combination of I_{corr} and E_{corr} for better corrosion resistance. In contrast, the set of samples with $(D/L)^2=1$ showed that the sample with the lowest I_{corr} did not have the highest E_{corr} . Samples D20L40 and D20L20 had better (lower) I_{corr} values compared with sample REF and others. Sample REF had the best E_{corr} (highest) amongst all and samples D20L30, D5L20 and D20L40 ranked in next places.

Table 4-5. Dependence of I_{corr} of all samples and different parameters after the first test.

Sample (ranking) ascendingly		I_{corr} ($\mu A/cm^2$)	X direction			Y direction		
			Ra/D	Ra/L	(D/L) ²	Ra/D	Ra/L	
1	D20L40	0.03	0.050	0.025	0.25	I	0.050	0.050
2	D20L20	0.4076	0.040	0.040	1		0.035	0.035
3	D5L20	0.6153	0.040	0.010	0.062		0.040	0.010
4	D10L30	6.191	0.052	0.017	0.108	II	0.108	0.036
5	D5L10	6.976	0.096	0.048	0.25		0.088	0.044
6	D10L20	7.3	0.065	0.032	0.25		0.056	0.028
7	D20L30	11.49	0.036	0.024	0.435		0.029	0.019
8	D5L5	16.56	0.054	0.054	1		0.050	0.050
9	D10L10	62.51	0.030	0.030	1		0.023	0.023

Table 4-6. Dependence of E_{corr} of all samples and different parameters after the first test.

Sample (ranking) descendingly		E_{corr} (mV)	X direction			Y direction	
			Ra/D	Ra/L	(D/L) ²	Ra/D	Ra/L
1	D10L10	-200.5	0.030	0.030	1	0.023	0.023
2	D20L30	-262.7	0.036	0.024	0.435	0.029	0.019
3	D5L20	-262.8	0.040	0.010	0.062	0.040	0.010
4	D20L40	-280.6	0.050	0.025	0.25	0.050	0.050
5	D5L5	-295.1	0.054	0.054	1	0.050	0.050
6	D20L20	-305.7	0.040	0.040	1	0.035	0.035
7	D10L30	-306.2	0.052	0.017	0.108	0.108	0.036
8	D5L10	-307.5	0.096	0.048	0.25	0.088	0.044
9	D10L20	-312.4	0.065	0.032	0.25	0.056	0.028

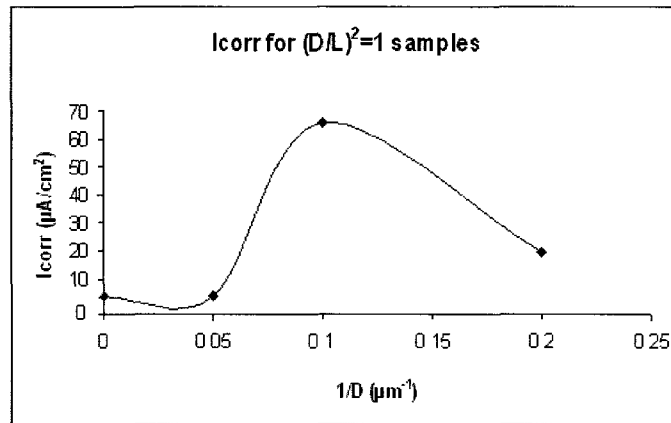


Fig. 4-24. The I_{corr} values versus hole diameters (D) for all samples with $(D/L)^2=1$ and sample REF $(D/L)^2=0$ after the first corrosion test.

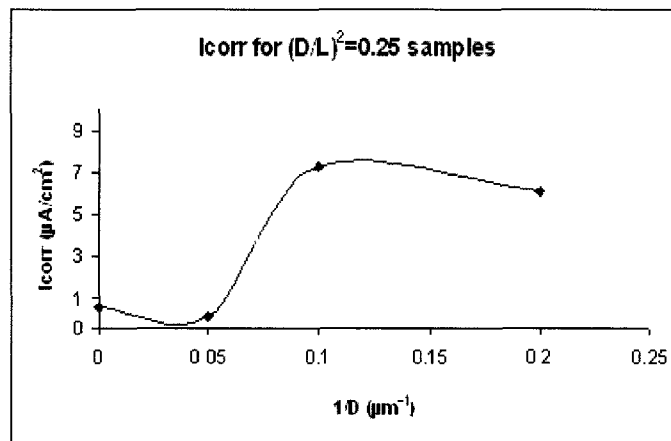


Fig. 4-25. The I_{corr} values versus hole diameters (D) for all samples with $(D/L)^2=0.25$ and sample REF $(D/L)^2=0$ after the first corrosion test.

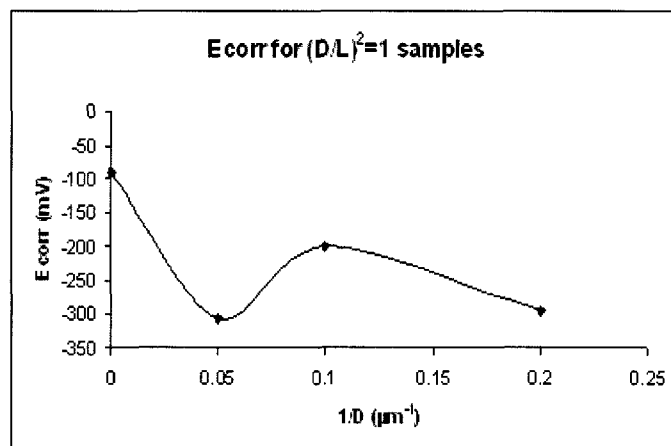


Fig. 4-26. The E_{corr} values versus hole diameters (D) for all samples with $(D/L)^2=1$ and sample REF $(D/L)^2=0$ after the first corrosion test.

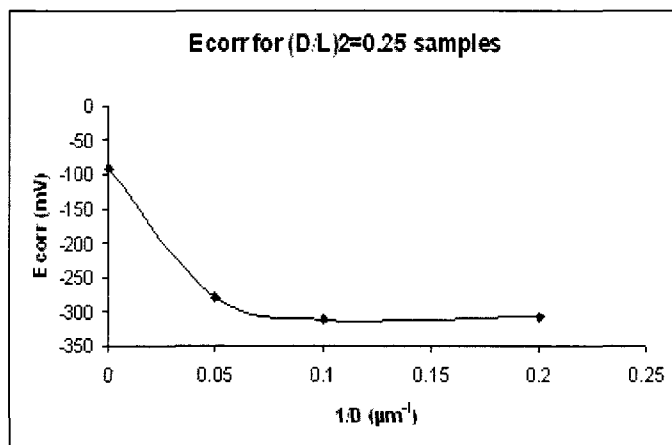


Fig. 4-27. The E_{corr} values versus hole diameters (D) for all samples with $(D/L)^2=0.25$ and sample REF.

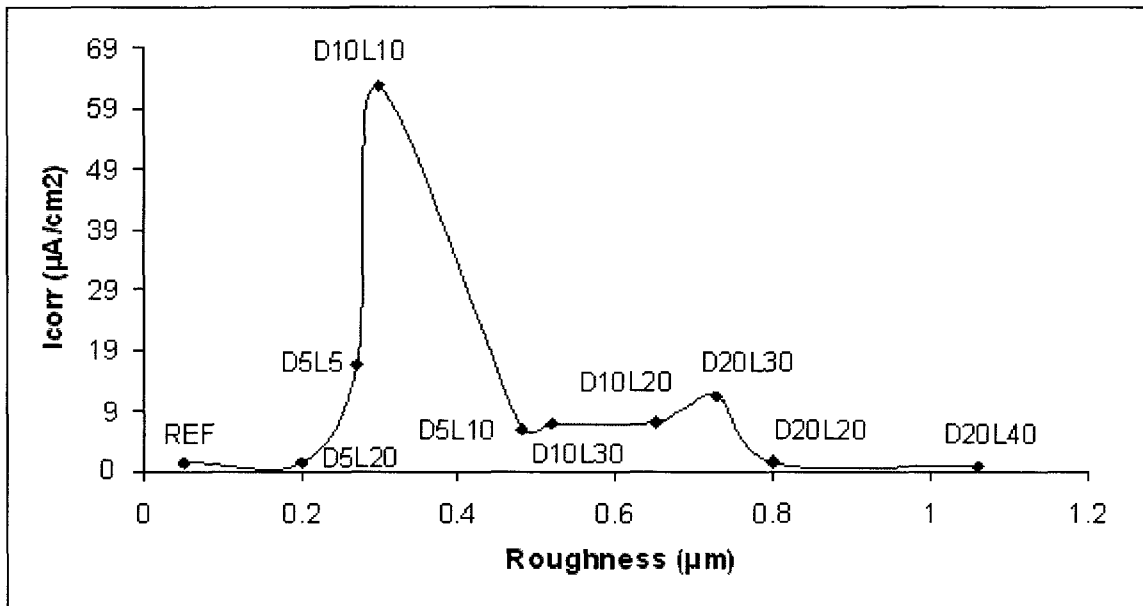


Fig. 4-28. Icorr values for all samples versus roughness.

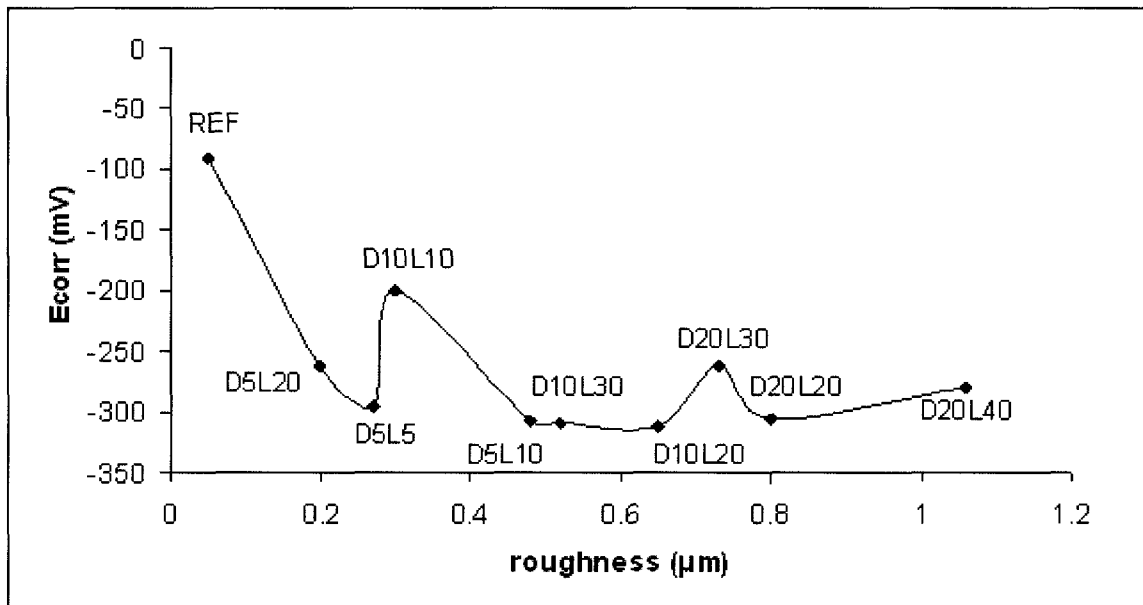


Fig. 4-29. Ecorr values for all samples versus roughness.

4.5. SEM images after corrosion tests

Fig. 4-30 shows the SEM images of sample REF after one corrosion test. As it can be observed, there are some severe, local corroded areas: See Fig. 4-30 (b) for magnified view. It is evident that those areas were formed by coalescence of small pits or holes. Sample REF had a severe local corrosion and unacceptable surface condition after the corrosion test.

Sample D5L5 corroded surface is shown in Fig. 4-31. This figure contains three corroded surfaces from the three corrosion tests. After the first test there is no sign of any severe corrosion [see Fig. 4-31 (a) and (b)]. The second test destroyed the patterning. The third test result is similar to the second one [Fig. 4-31 (e) and (f)].

Comparing corroded surfaces of samples D5L10 (Fig. 4-32) and D5L5 does not show any large differences. The patterning degradation is similar in both cases. The I_{corr} of sample D5L10 is in the middle of corrosion current density ranking (see Table 4-5) and the surface condition after the first test is not significantly damaged [(a) and (b)]. In the second and third tests the surface destruction became worse and worse and the pattern was fully removed.

The corroded surfaces of sample D5L20 are presented in Fig. 2-33. In the first test a local corroded area was observed [(a) and (b)]. Based on values of I_{corr} , the surface of this sample (ranked 3rd) should be in good condition. The damage was confined to a small area and did not affect the whole surface. The surface after the second and the third tests showed huge corroded areas and the surface had a wave-like appearance.

Sample D10L10 showed a severe corroded appearance (Fig. 4-34). After the first test the surface has a porous structure [(a) and (b)] and after the second test the surface changed significantly and any patterning was completely removed [(c) and (d)]. After the third test the corroded regions are deeper than samples of $D=5\mu\text{m}$ and also the depth of different regions are different [(e) and (f)]. According to I_{corr} of this sample there is a good agreement between corrosion current density and the surface condition especially after the first test.

Sample D10L20 SEM images are presented in Fig. 4-35. The patterned surface was slightly changed after the first test [Fig. 4-35 (a)]. Some small corroded areas (maybe pits) are observed in the holes [Fig. 4-35 (b)]. This sample was gradually damaged from the first test to the last test [follow images from (b) to (d) to (f)]. It is evident that the inside of the hole was partially corroded in the first test and in the third one the hole was overally corroded and the shape was affected. The I_{corr} value for this sample was in the middle of the rankings.

Sample D10L30 was similar to sample D10L20, but with the difference that after the first test the whole surface was corroded [Fig. 4-36 (a) and (b)]. It is difficult to distinguish between a hole and its surrounding flat area after the first corrosion test and in the next test the surface is completely destroyed. In the third test, there are heavily corroded areas.

Surface images of sample D20L20 are presented in Fig. 4-37. This sample showed good appearance after all tests. The first corroded surface (a) showed almost no change compared to the original sample. In addition, in the following tests the sample had approximately the same appearance. The surface of this sample confirms low magnitude of I_{corr} (better than sample REF) in the tests. It seems that the passive layer formed in the first test was stable and protected the surface in subsequent corrosion tests compared to any passive behavior noted in polarization curves.

Sample D20L30 [Fig. 4-38] showed almost the same behavior as samples D10L10 and D10L20. After the initial corrosion test, corroded areas appeared on the sample surface. In the following tests, the corrosion became progressively worse. Some severe deep corroded areas were created on the surface and any patterning could no longer be seen [Fig. 4-38 (e) and (f)].

Sample D20L40 exhibited the best amount of patterning degradation. Comparing the original sample and after the first corrosion test there was no obvious change either inside or outside the holes [Figs 4-39 (a) and 4-4 (f)]. The I_{corr} was the lowest of all samples. After the second corrosion test there was some surface damage but the pattern was well defined. Finally, after the third corrosion test the surface was damaged but the pattern was not fully degraded.

In summary, it can be said that in most samples the surface appearances was in good agreement with calculated I_{corr} values. Samples D20L20 and D20L40 had the lowest surface degradation after the first test.

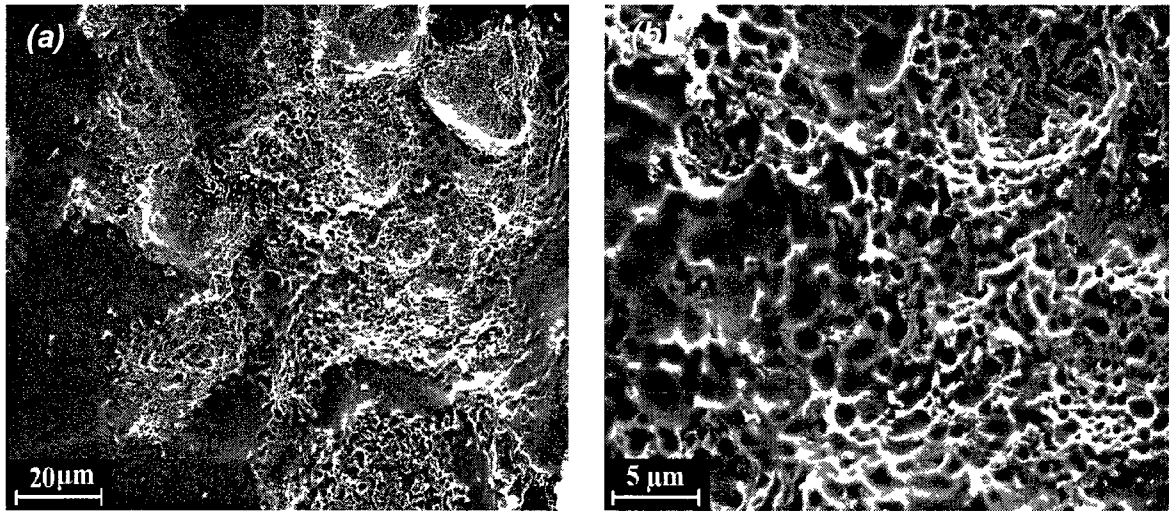


Fig. 4-30. The SEM micrographs of sample REF after the first corrosion test.

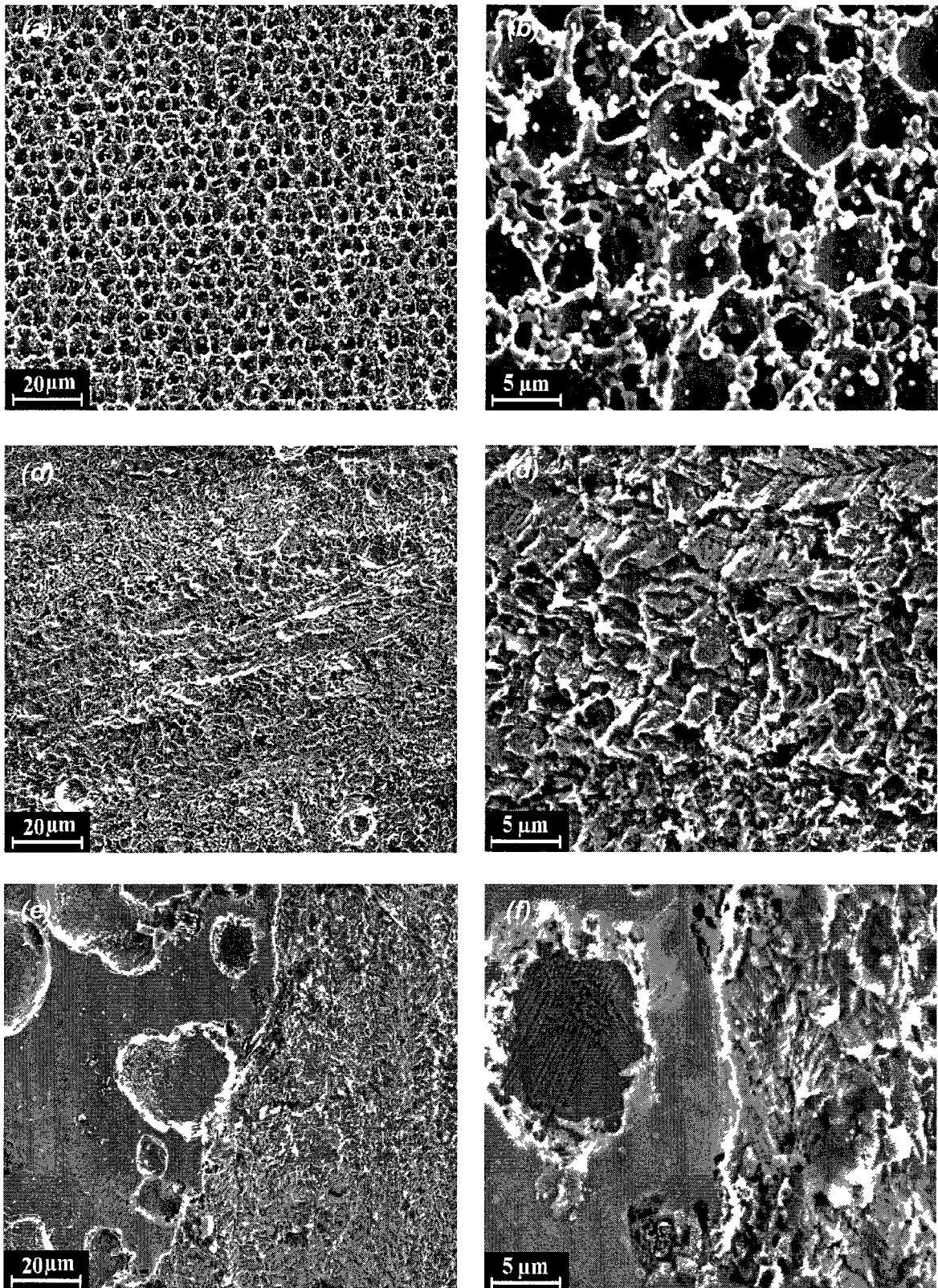


Fig 4-31 The SEM micrographs of sample D5L5 after (a) and (b) the first, (c) and (d) the second, (e) and (f) the third corrosion tests in 0.5M H₂SO₄

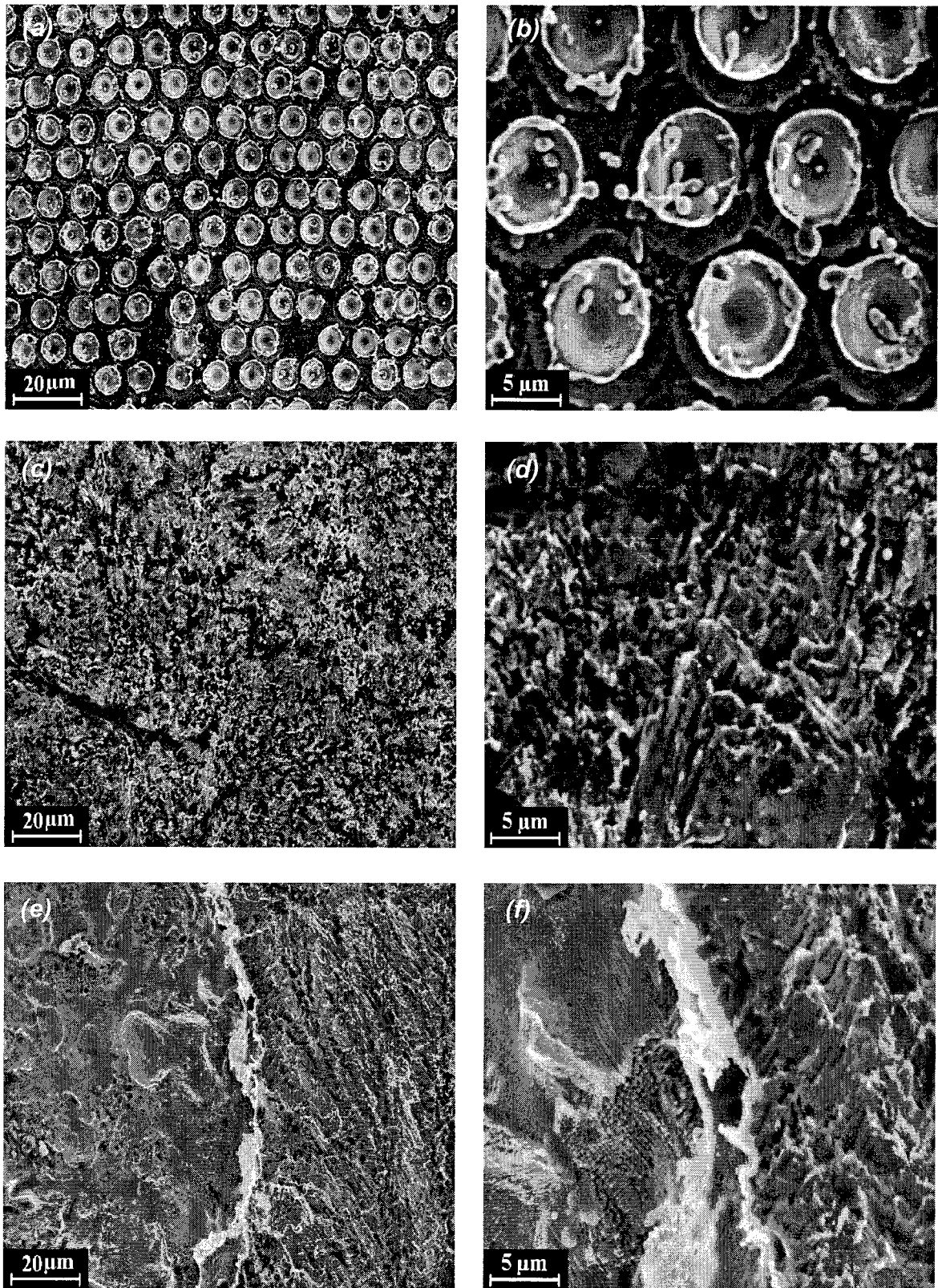


Fig. 4-32. The SEM micrographs of sample D5L10 after: (a) and (b) the first; (c) and (d) the second; (e) and (f) the third corrosion tests in 0.5M H_2SO_4 .

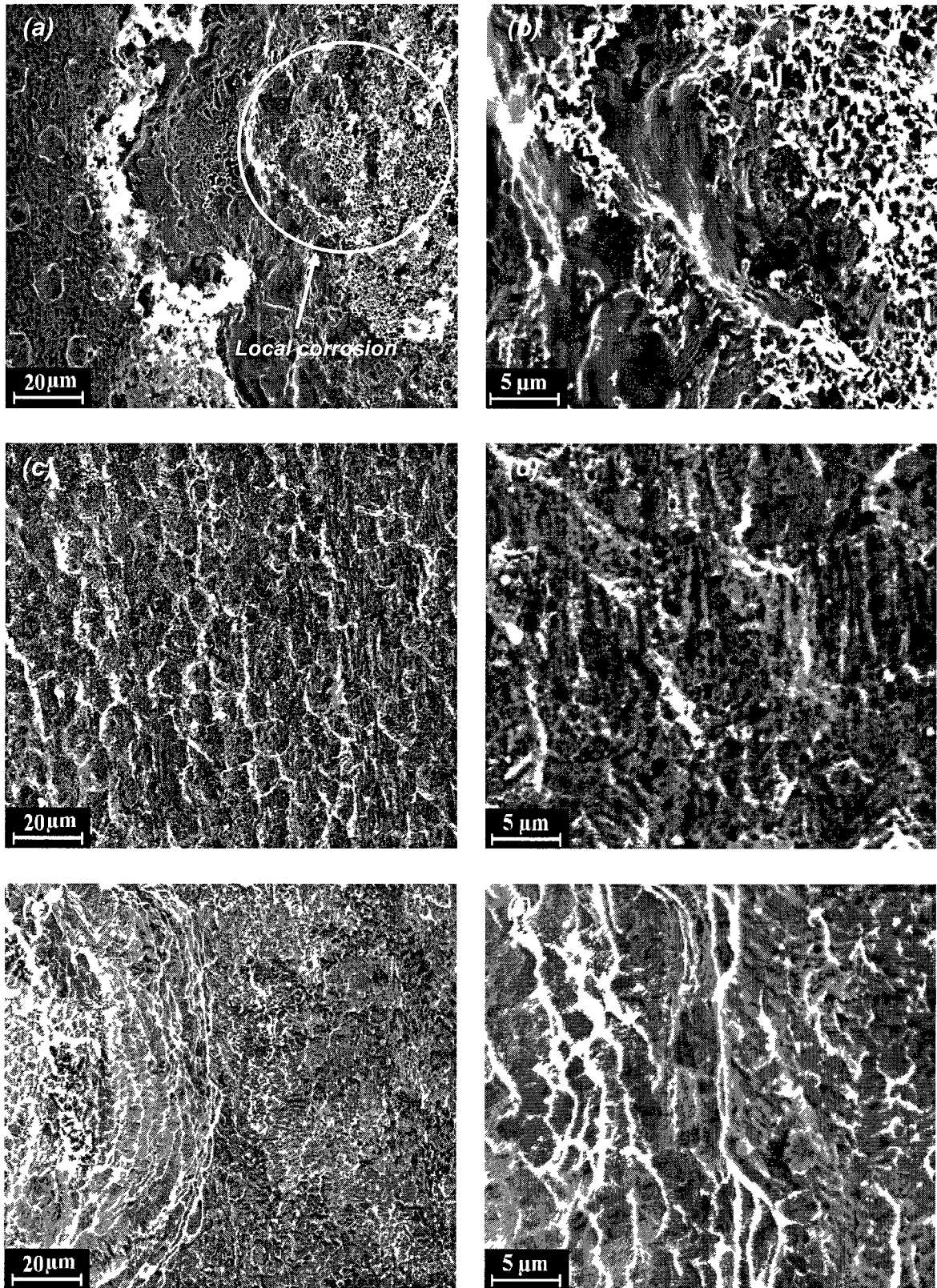


Fig 4-33 The SEM micrographs of sample D5L20 after (a) and (b) the first, (c) and (d) the second; (e) and (f) the third corrosion tests in 0.5M H₂SO₄

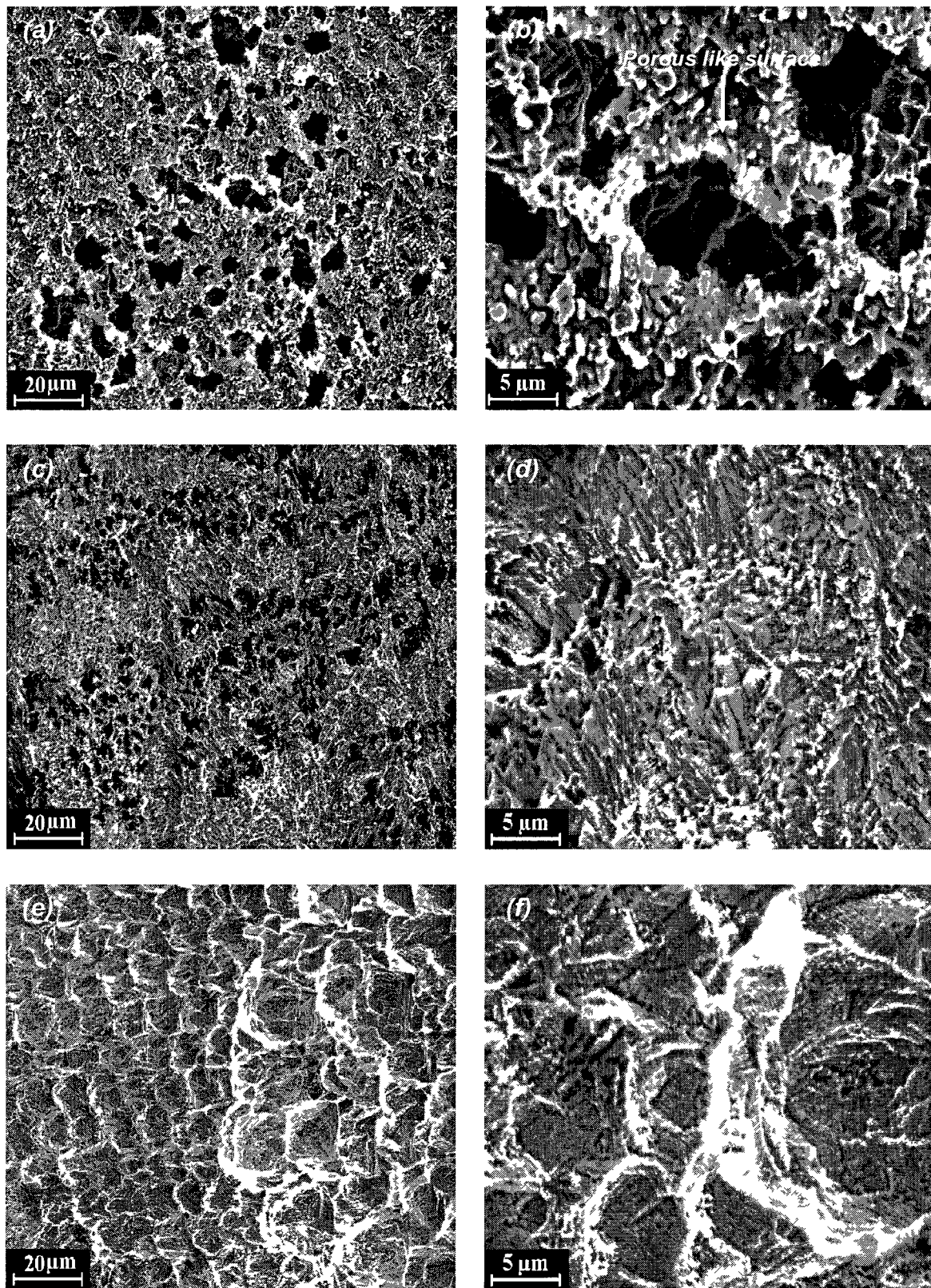


Fig 4-34 The SEM micrographs of sample D10L10 after (a) and (b) the first, (c) and (d) the second, (e) and (f) the third corrosion tests in 0.5M H₂SO₄

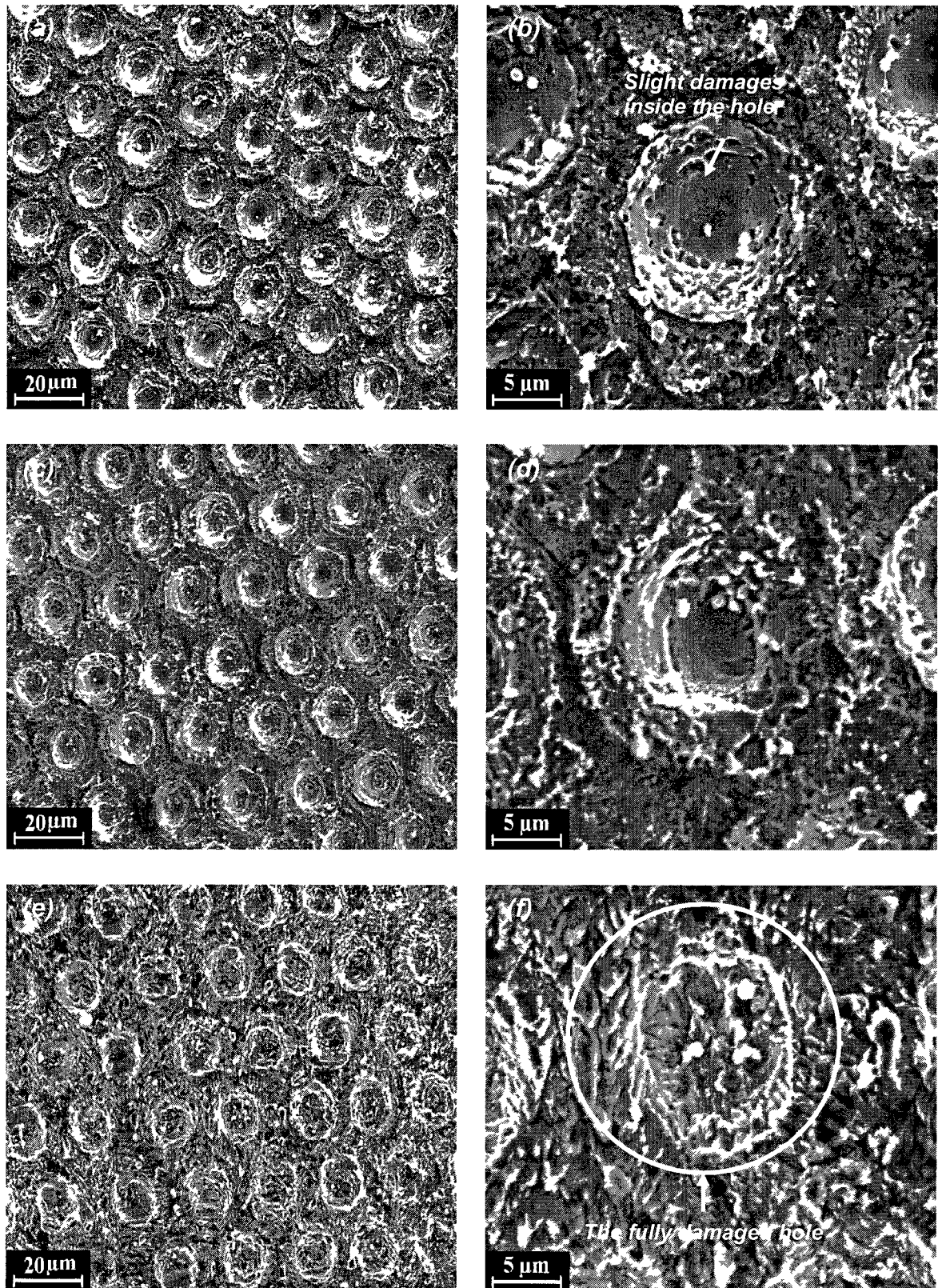


Fig 4-35 The SEM micrographs of sample D10L20 after (a) and (b) the first, (c) and (d) the second, (e) and (f) the third corrosion tests in 0.5M H_2SO_4

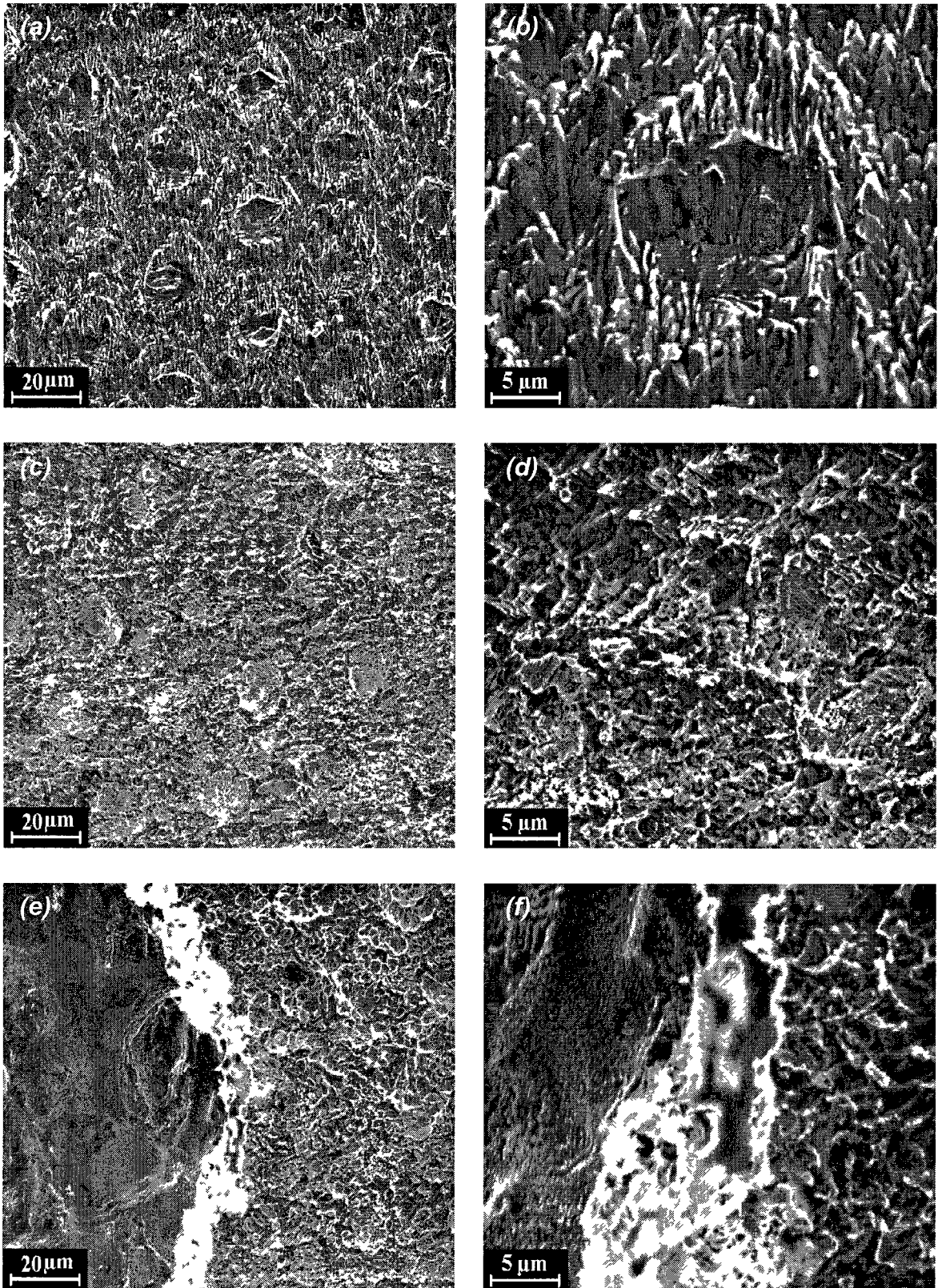


Fig 4-36 The SEM micrographs of sample D10L30 after (a) and (b) the first; (c) and (d) the second, (e) and (f) the third corrosion tests in 0.5M H₂SO₄

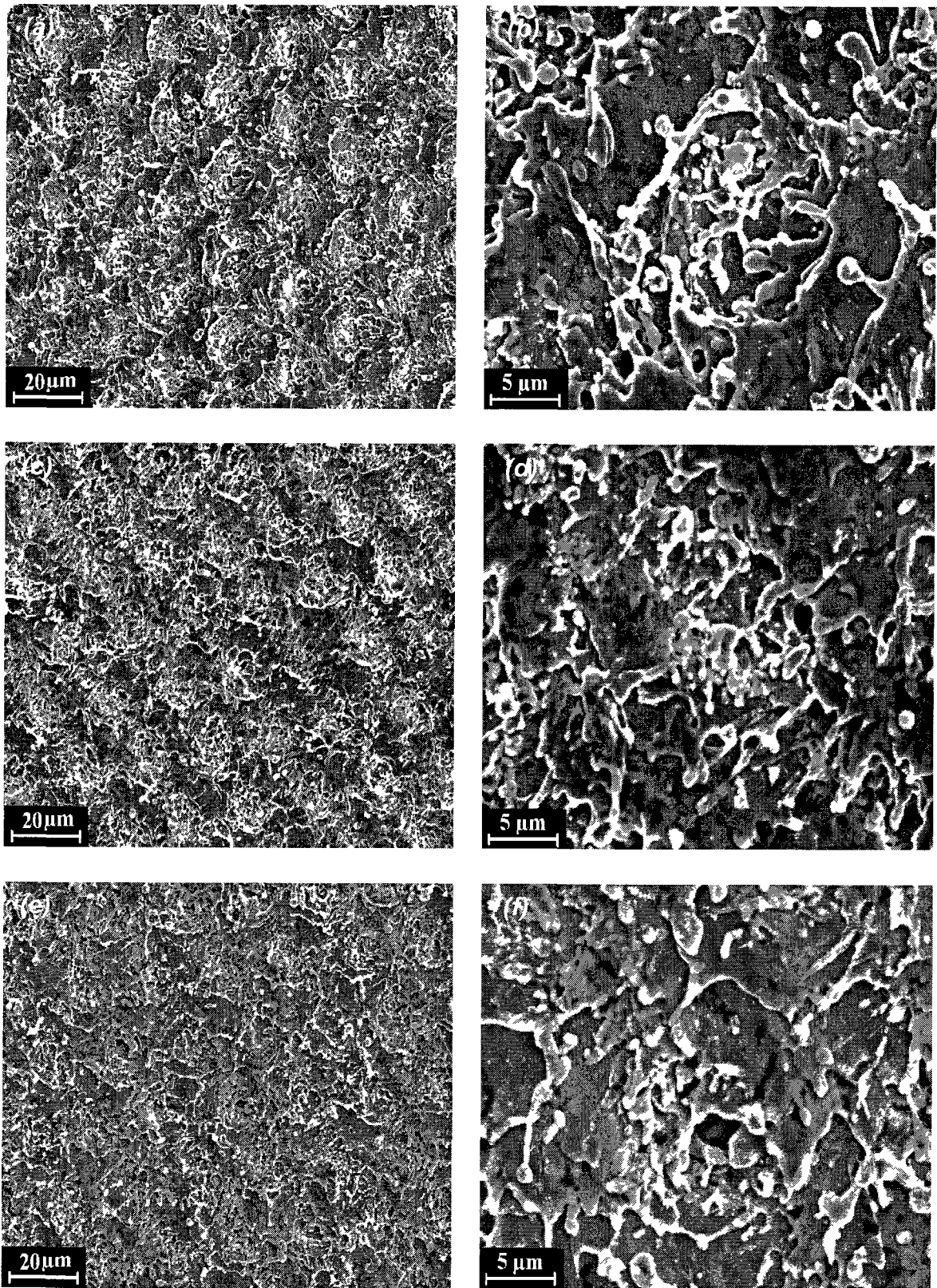


Fig 4-37 The SEM micrographs of sample D20L20 after (a) and (b) the first; (c) and (d) the second, (e) and (f) the third corrosion tests in 0.5M H₂SO₄.

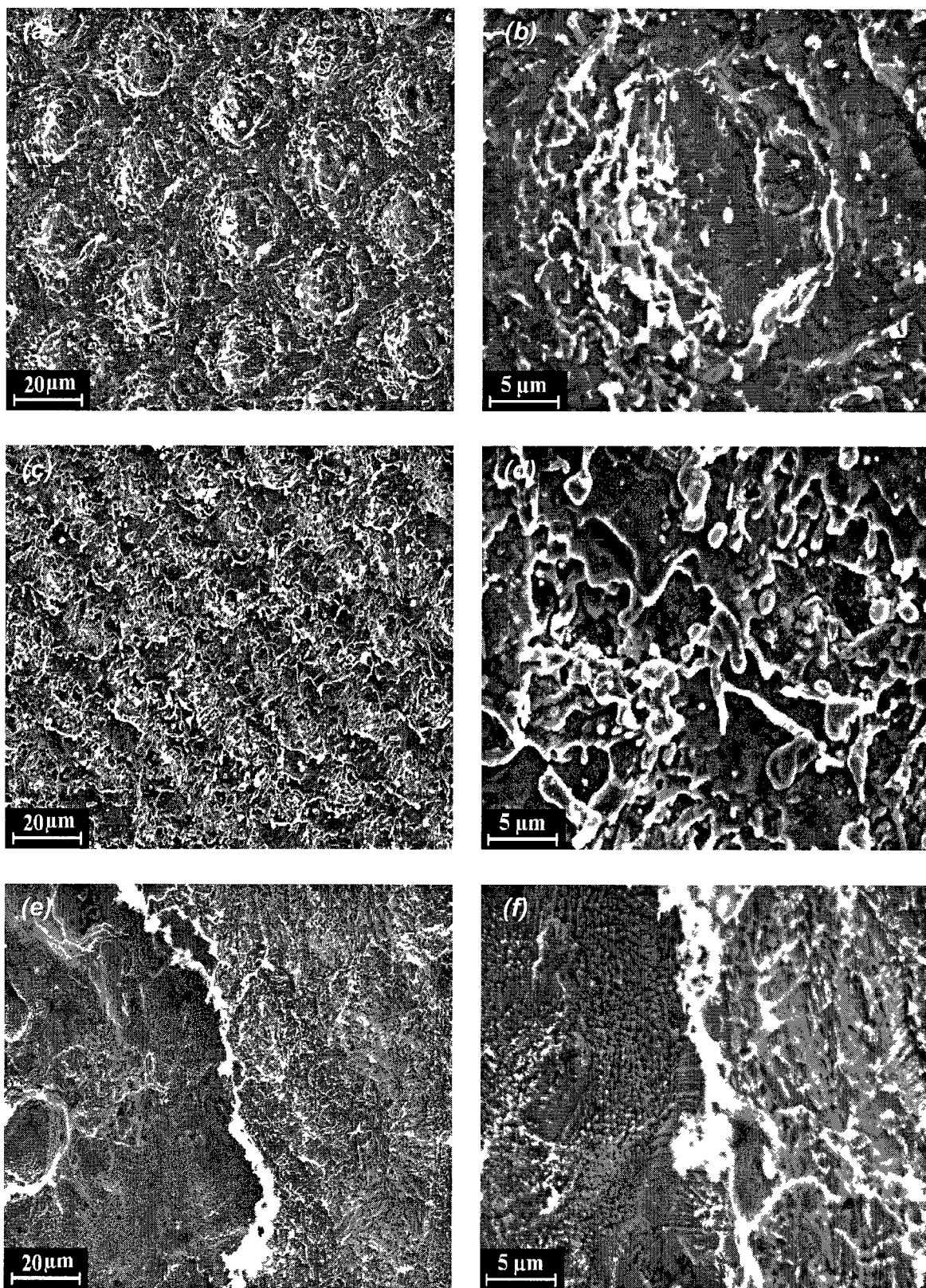


Fig 4-38 The SEM micrographs of sample D20L30 after (a) and (b) the first; (c) and (d) the second, (e) and (f) the third corrosion tests in 0.5M H₂SO₄

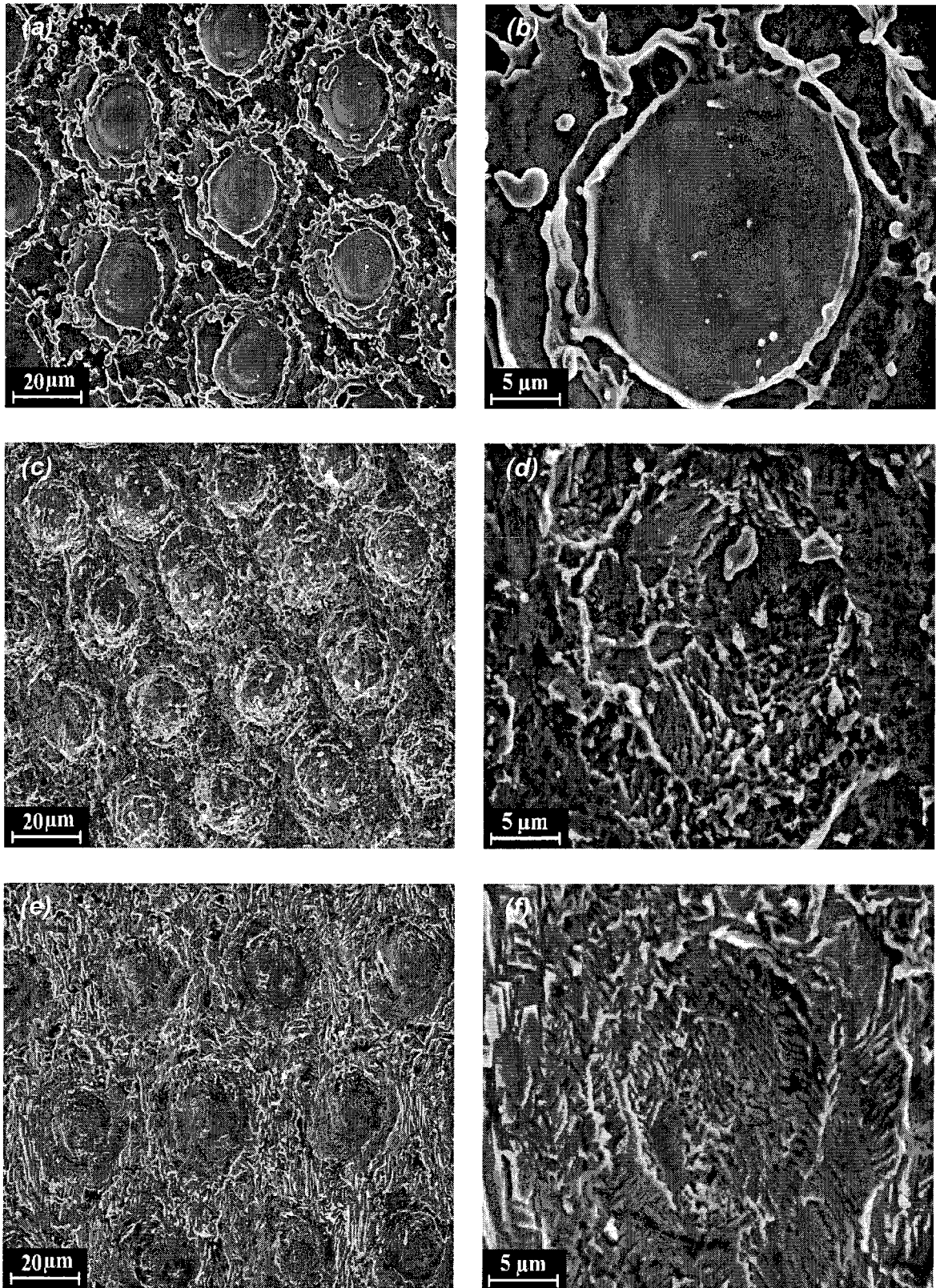


Fig. 4-39. The SEM micrographs of sample D20L40 after: (a) and (b) the first; (c) and (d) the second; (e) and (f) the third corrosion tests in 0.5M H₂SO₄.

4.6. Roughness after corrosion tests

Table 4-7 presents the roughness values of all samples after the second corrosion test. A comparison between all values shows that for some samples the roughness increased and for the others decreased. The highest and lowest Ra were observed for samples D10L20 (sample D20L40 before corrosion tests) and D5L10 (sample D5L5 before corrosion tests), respectively. Generally there was no clear trend or dependency in roughness changes after corrosion tests.

Fig. 4-40 shows the roughness data for sample D5L5. The 3D image of this sample shows a local severely corroded area (the blue area). As it is observed the height distribution is less uniform compared to that of the initial sample (see Fig. 4-6). The histogram curve in Fig. 4-40 is a bit shifted to the right side in comparison to that of initial sample. This confirms the average roughness was increased due to corrosion phenomena after two corrosion tests.

The roughness data of sample D5L20 are presented in Fig. 4-41. Again in this sample the roughness increased compared to the initial state. Local blue and red areas show non uniform areas on the surface as a result of the corrosion tests. In the histogram curve, the average roughness did not change much compared with the initial sample (Fig. 4-7) but the distribution was extended which is due to increase in height or depth at different places on the surface. Sample D10L20 is similar to samples D5L5 and D5L20, but its histogram curves [Fig. 4-42 (d)] is a bit different from the initial one [Fig. 4-8 (d)]. In the histogram curve there is a horizontal part but this part is much shorter in the curve before corrosion tests. This proves that due to corrosion reactions a larger area of the sample was attacked by corrosive components, the surface was damaged and as a result the surface is rougher.

Comparing the histogram curves of samples D20L20 before [Fig. 4-9 (d)] and after corrosion tests [Fig. 4-43 (d)] gives some useful information about the sample. In the 3D images there is no large difference in their surface appearance (good agreement with the SEM images). It seems both surfaces are almost identical. This is in a good agreement with the Icorr values. This sample has a very low Icorr (lower than sample REF). The histograms are similar and there is

just a little shift toward down for the curve after the second corrosion test. This means the sample had a good corrosion resistance and its surface resisted the corrosive medium well.

Sample D20L40 has a similar behavior to sample D20L20. The 3D images are similar and no sign of severe corrosion is observable. The histogram curves show that the average roughness is still close to zero after two corrosion tests. Some irregularities in the histogram curves after the second test maybe refer to some local corroded areas [see Figs. 4-44 and 4-10 (d)].

Table 4-7. The roughness value obtained from profilometry for some corroded samples

Sample codes	Roughness values									
	X direction					Y direction				
	Rq	Ra	Rt	Rp	Rv	Rq	Ra	Rt	Rp	Rv
D5L5	0.81	0.58	4.50	1.63	-2.87	0.42	0.34	2.39	1.49	0.89
D5L10	0.44	0.35	2.73	1.14	-1.58	0.48	0.38	2.81	1.34	-1.46
D5L20	0.72	0.57	3.84	1.73	-2.10	0.85	0.69	4.42	1.84	-2.57
D10L10	0.75	0.60	4.08	1.87	-2.21	0.74	0.6	3.76	1.47	-2.28
D10L20	1.18	1.07	4.20	1.36	-2.84	1.04	0.87	4.15	1.25	-2.9
D10L30	0.61	0.48	3.57	1.52	-2.05	0.60	0.47	3.61	1.71	-1.90
D20L20	0.74	0.62	3.62	1.37	-2.24	0.78	0.62	3.91	1.85	-2.05
D20L30	1.07	0.85	5.06	1.92	-3.14	1.14	0.98	4.97	1.85	-3.11
D20L40	0.92	0.71	4.71	1.64	-3.06	0.91	0.66	4.77	1.79	-2.98

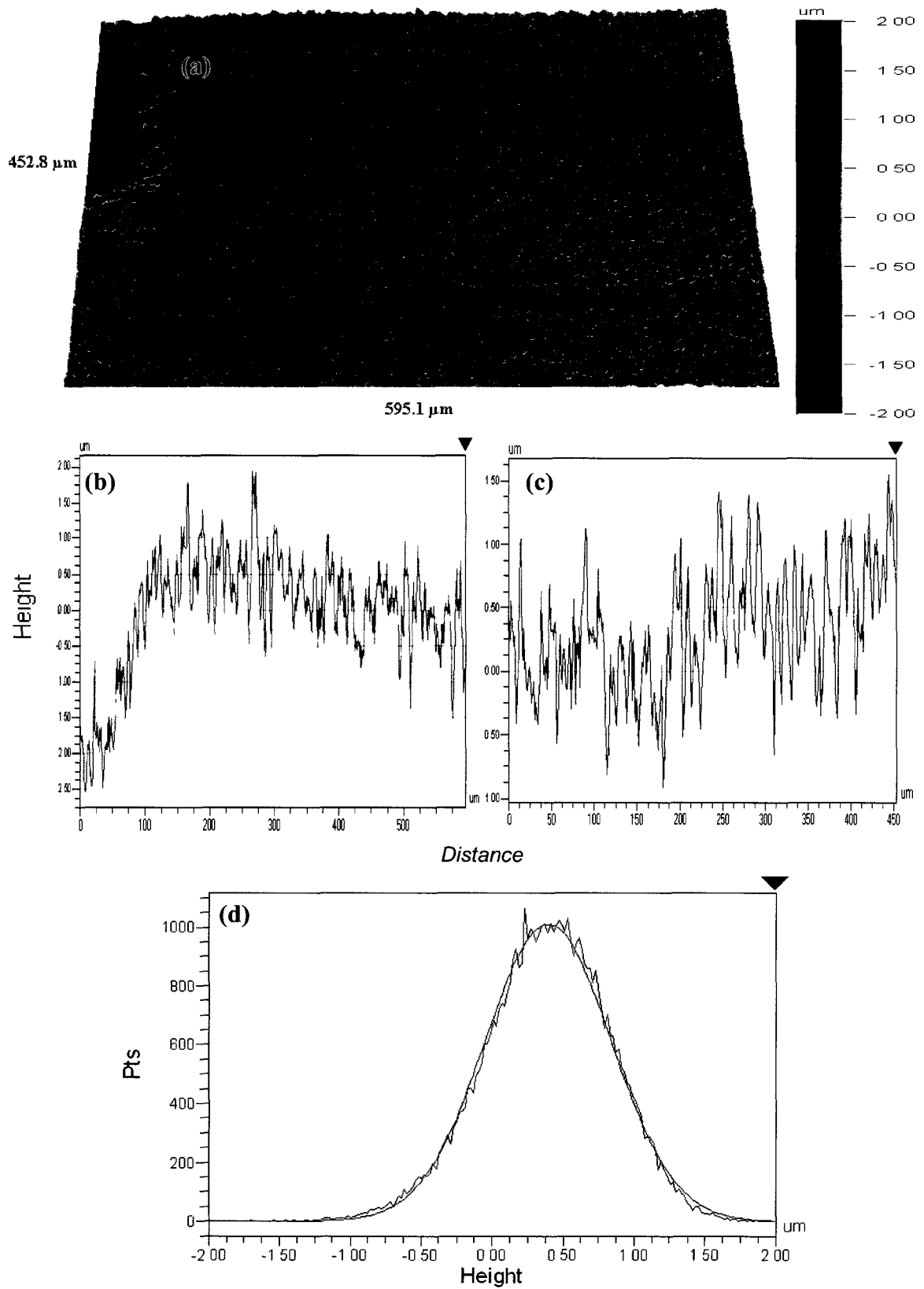


Fig. 4-40. Sample D5L5 (a) 3D roughness, (b) X-profile, (c) Y-profile and (d) histogram curve after the second corrosion test.

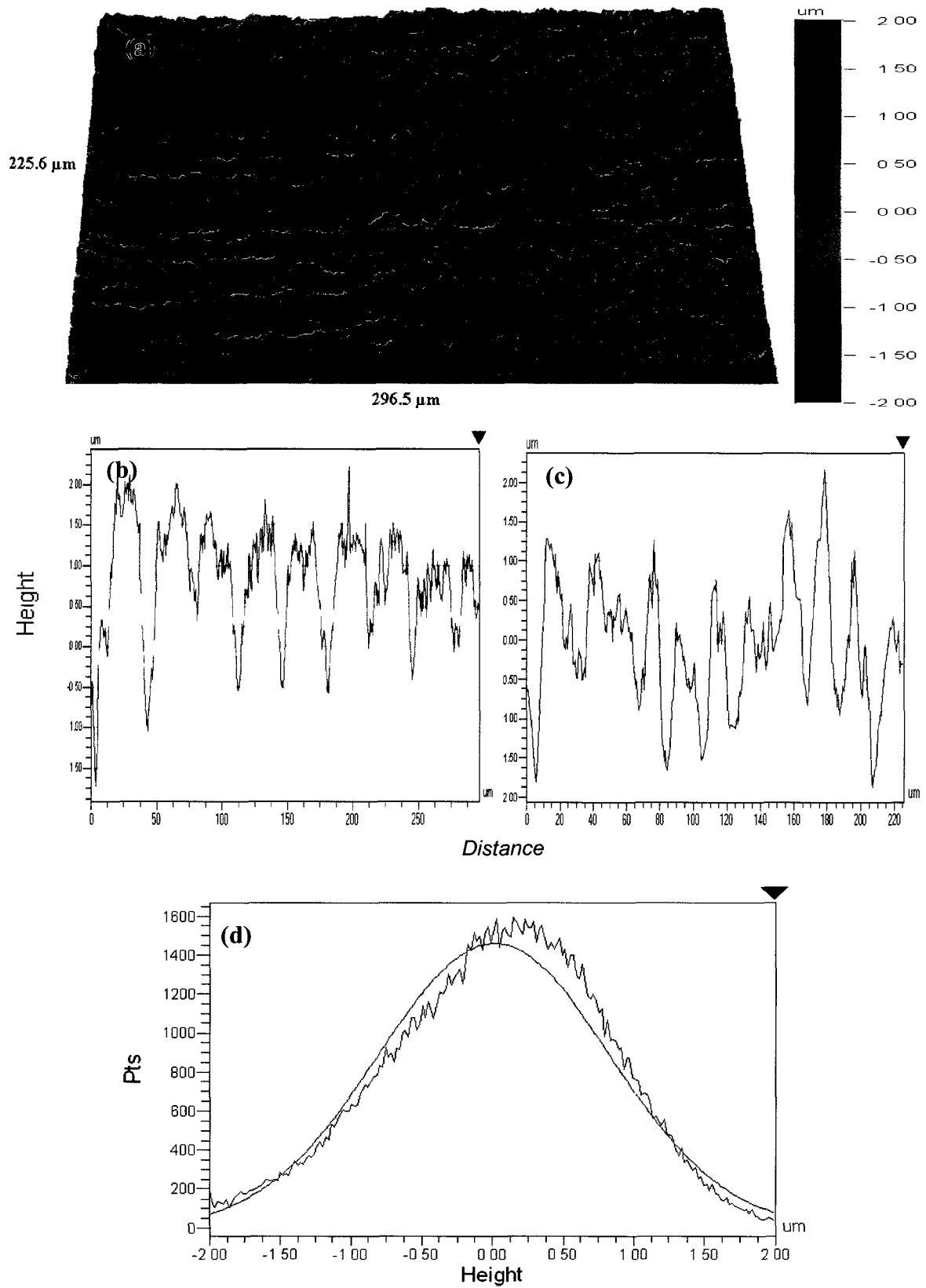


Fig. 4-41. Sample D5L20 (a) 3D roughness, (b) X-profile, (c) Y-profile and (d) histogram curve after the second corrosion test.

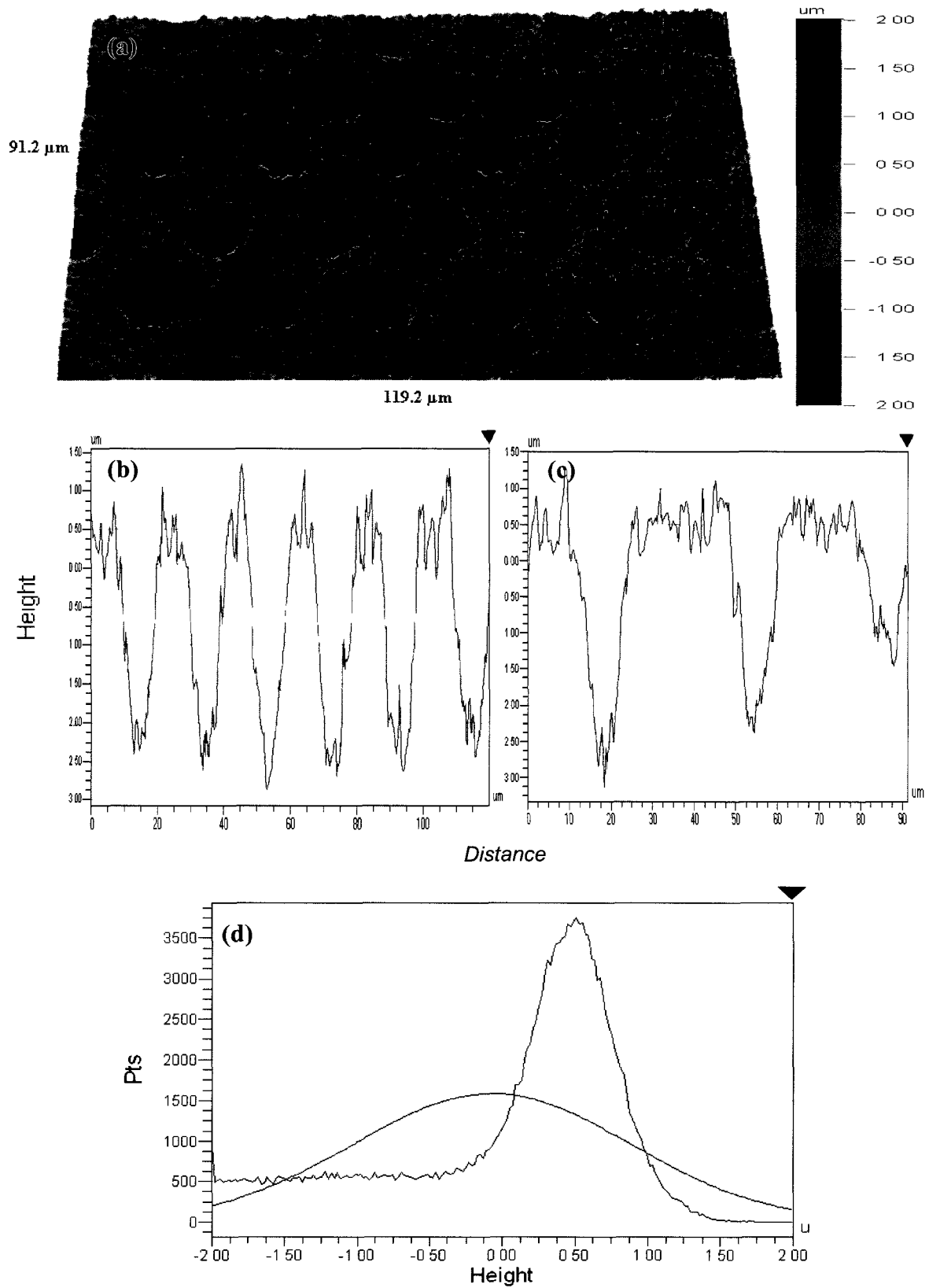


Fig. 4-42. Sample D10L20 (a) 3D roughness, (b) X-profile, (c) Y-profile and (d) histogram curve after the second corrosion test.

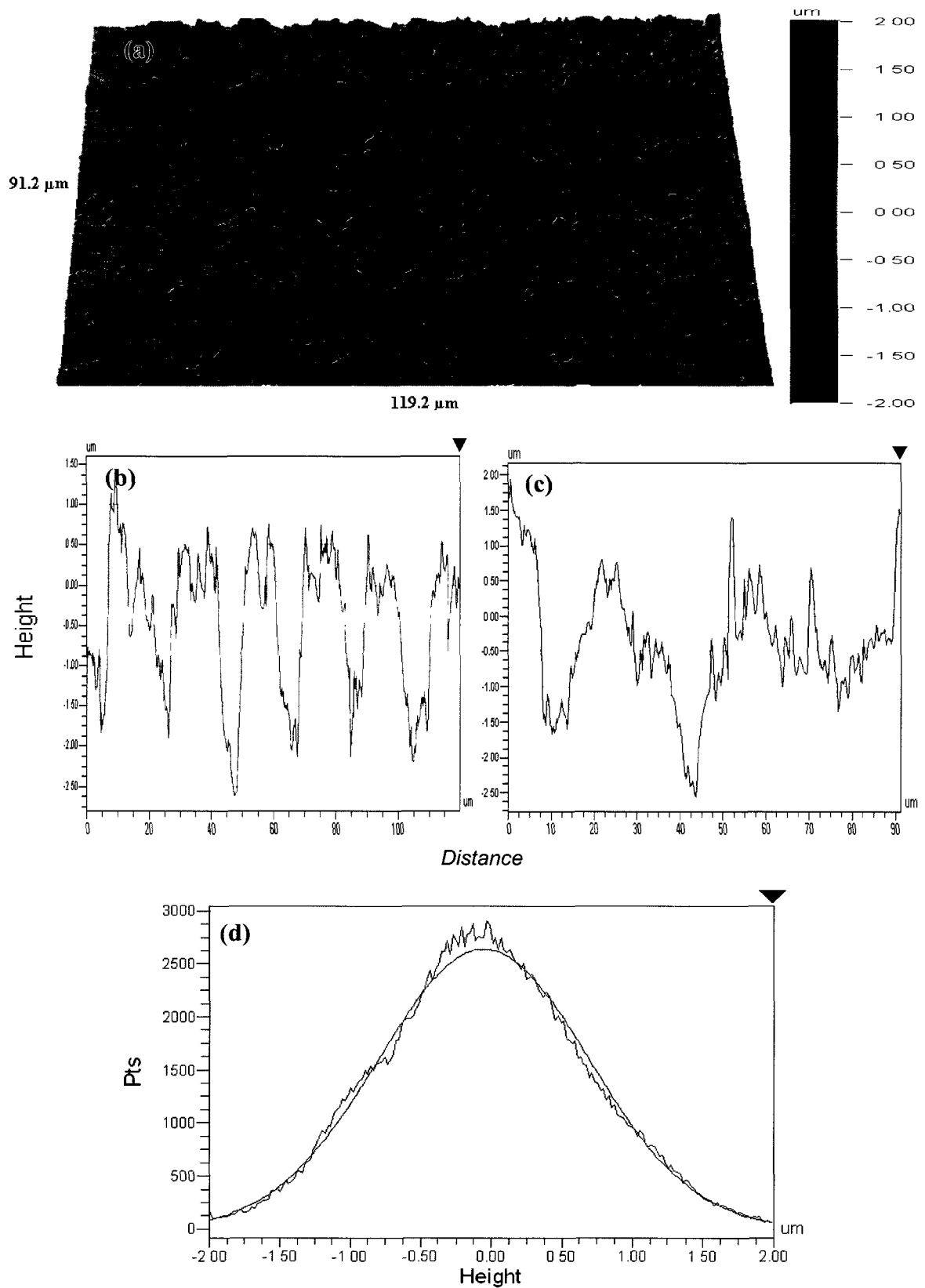


Fig. 4-43. Sample D20L20 (a) 3D roughness, (b) X-profile, (c) Y-profile and (d) histogram curve after the second corrosion test.

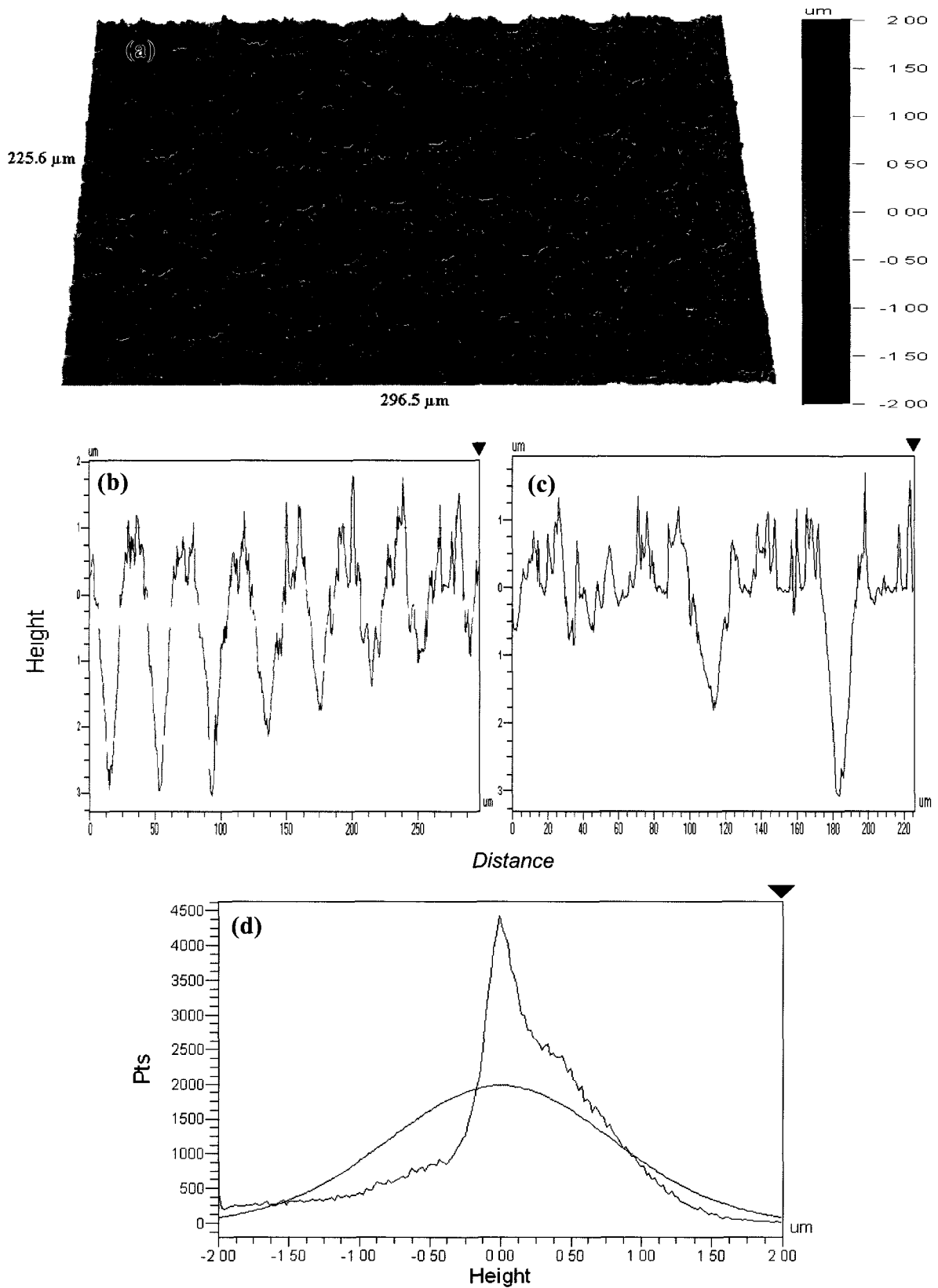


Fig. 4-44. Sample D20L40 (a) 3D roughness, (b) X-profile, (c) Y-profile and (d) histogram curve after the second corrosion test.

4.7. EDS after the first corrosion test

In the corrosive environment of this research there were some ions such as H^+ , SO_4^{2-} , O^{2-} and Ni ions. Some questions could arise as to which ion is reduced and which one is oxidized while corrosion or what compound would be the corrosion product? Regarding all EDS spectra it is understood that there is no sulfur peak in the spectra. So it can be said that after corrosion no $NiSO_4$ was formed on the surface. In addition, $NiSO_4$ is highly soluble in water. In turn, oxygen peak was observed and its amount was different in some cases. Generally it seems that an oxide layer was formed on the corroded surfaces during the corrosion tests. Another point refers to the ratio of Ni/O (the most intense Ni peak to the oxygen peak). Comparing sample REF in both conditions before the test [Fig. 4-5 (a)] and after the first test [Fig. 4-45 (a)] shows that there is a small change in the ratio. The EDS spectra of sample D5L20 on the surface [Fig. 4-45 (b)] and in the pit [Fig. 4-45 (c)] does not show any significant difference. The Ni/O ratio is different in sample D20L40 before and after the corrosion test [Fig. 4-45 (d) and Fig. 4-5 (e)]. This shows more oxygen, due to corrosion, in the corroded sample rather than the initial sample. Also it is seen that the amount of oxygen inside the hole [Fig. 4-45 (e)] is less than that on the surface. This could be supporting evidence to suggest corrosion into the holes is less than in the surrounding areas in this sample.

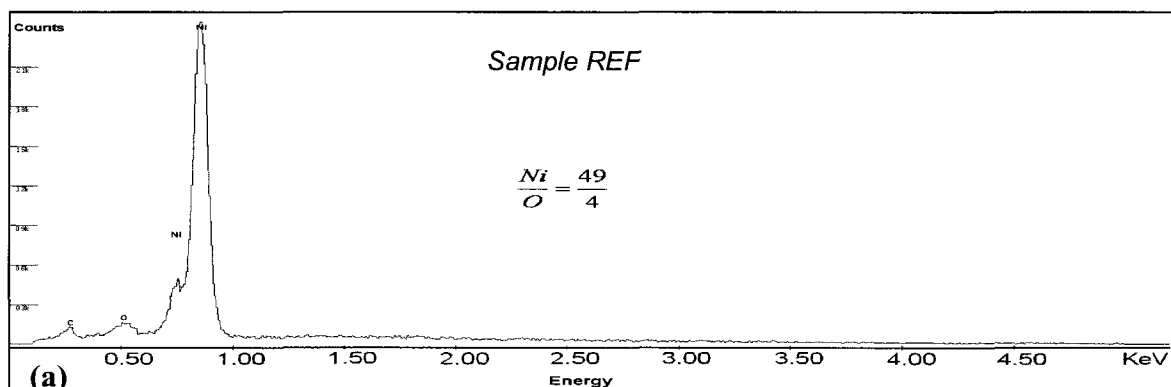
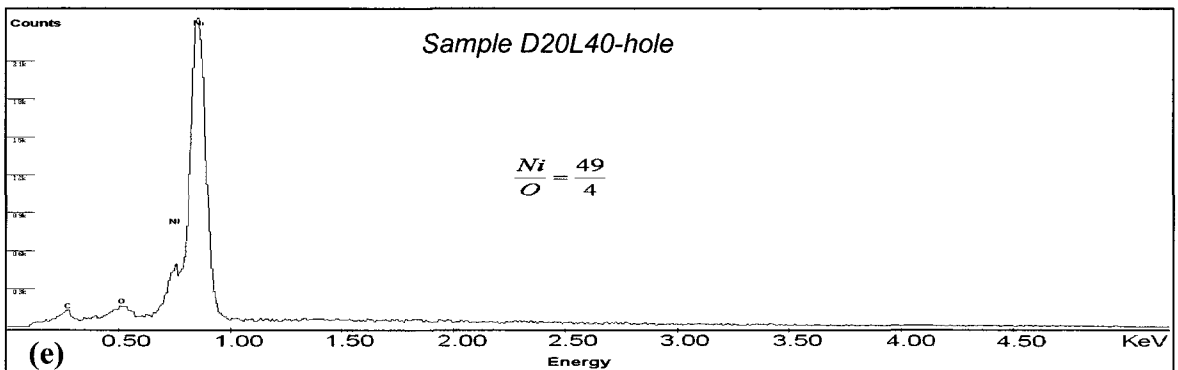
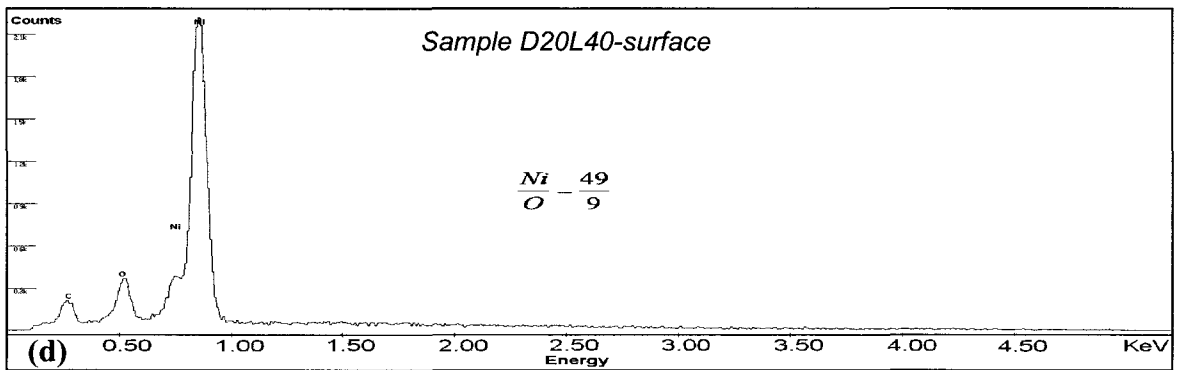
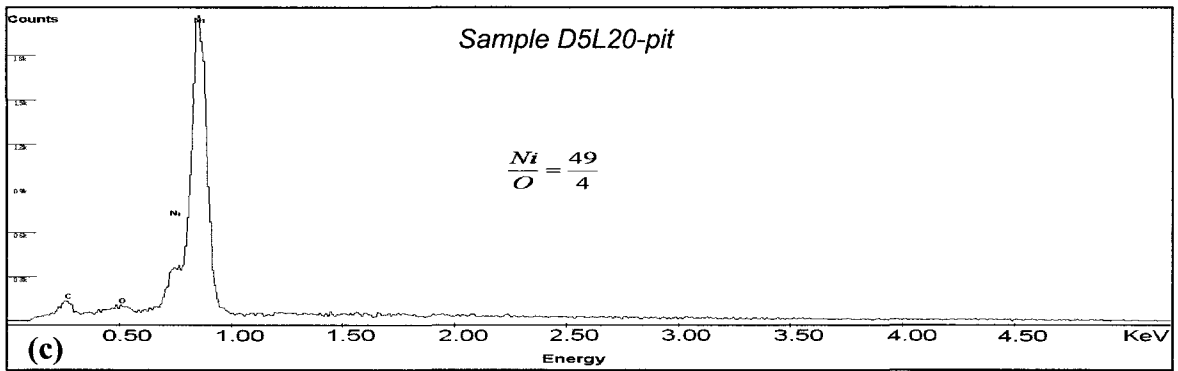
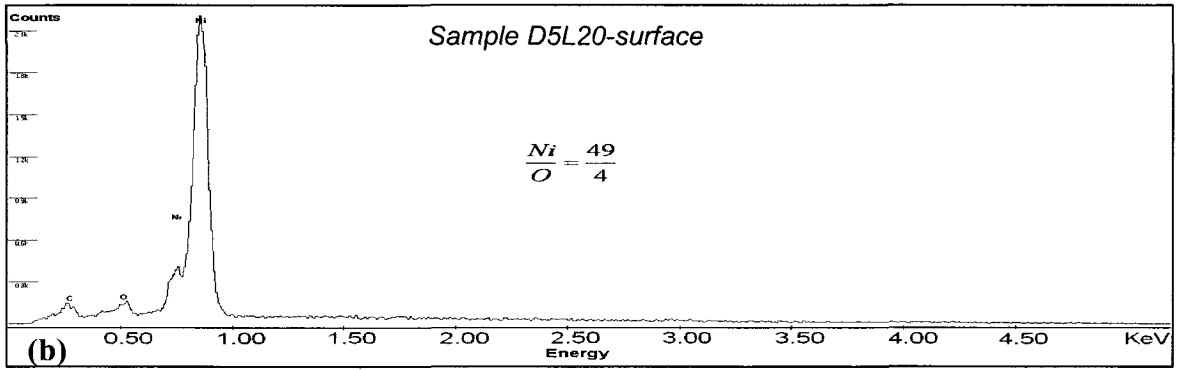


Fig. 4-45. EDS analysis spectra of samples (a) REF, (b) D5L20; surface, (c) D5L20; pit, (d) D20L40; surface, and (e) D20L40; hole (continued).



5. Conclusions

According to this research following conclusions can be drawn:

1. After the first corrosion test using the dynamic polarization method it was seen that samples D20L40 ($I_{corr} = 0.03 \mu A/cm^2$) and D20L20 ($I_{corr} = 0.4076 \mu A/cm^2$) have the lowest (the best) I_{corr} among all samples even better than sample REF ($0.5141 \mu A/cm^2$).

2. There is a trend or dependency between $(\frac{D}{L})^2$ ratio, hole size (D) and I_{corr} .

The higher the $(\frac{D}{L})^2$ ratio, the higher the I_{corr} . As a result it is better to have lower $(\frac{D}{L})^2$ ratio for better corrosion resistance. It is expected that smaller hole diameter (nano size) will decrease the I_{corr} which increases the corrosion resistance.

3. No special trend or dependency was seen between I_{corr} and other parameters, $\frac{R_a}{D}$ and $\frac{R_a}{L}$. After the second and the third corrosion tests, I_{corr} for most of samples were lower than sample REF because of previously formed passive layers. In fact, those tests are useful to find the general corrosion trend (especially passivity) of patterned samples.

4. Passive regions were observed in most of samples but mainly in the second corrosion tests.

5. E_{corr} of all patterned samples was lower than that of sample REF in all the tests. It means that sample REF had the highest (the best) E_{corr} in all samples. There was no clear trend or dependency between E_{corr} and the calculated parameters, $(\frac{D}{L})^2$, $\frac{R_a}{D}$ and $\frac{R_a}{L}$.

6. SEM images showed that after the first test some local corroded regions were created on surfaces but in the samples with the lowest I_{corr} there was slight change in surface (Samples D20L40 and D20L20). This confirms that the amount of corroded nickel after the first test was small. After the second and the third

tests the surfaces were severely corroded and local heavily corroded areas were observed in most of samples.

7. EDS analysis showed that the corroded layer is nickel oxide rather than nickel sulfate.

5.1. Recommendations for future research:

It is predicted that the following considerations can be useful for completion of this research or development of this subject.

- Using hole sizes smaller (less than 5 μm , toward nanoscale) or larger ($>20 \mu\text{m}$) can help define whether a general trend between I_{corr} , E_{corr} and $(\frac{D}{L})^2$. Also, using multiple samples can help define any relationships.
- According to previous research on hydrophobic surfaces, different surface pattern shapes affect the hydrophobic properties significantly. Thus, it is recommended to examine other hole shapes or other patterns on the nickel surface.
- Use a smaller laser pulse duration to create deeper holes, e.g. femtosecond pulse duration. Using this laser type can decrease the amount of splashes and it is possible to have a very well defined pattern on the surface. Also, since the depth of the holes can greatly affect the hydrophobic properties, varying depth holes should be examined.
- Measurement of water contact angle on the patterned surface using a specially designed optical microscope to find out whether the surface is initially hydrophobic or hydrophilic and also after surface patterning.
- Surface patterning on other metals or alloys, especially stainless steels. Stainless steels are one of the most applicable alloys with good anti corrosion properties and ability to produce passive layers on the surface to resist corrosion.

References:

- [1] K. Sasaki and G. T. Burstein, "The generation of surface roughness during slurry erosion-corrosion and its effect on the pitting potential", *Corrosion Science*, Vol. 38, No. 12, 1996, pp. 2111-2120.
- [2] T. Hong and M. Nagumo, "Effect of surface roughness on early stages of pitting corrosion of type 301 stainless steel", *Corrosion Science*, Vol. 39, No. 9, 1997, pp. 1665-1672.
- [3] M.H. Moayed, N.J. Laycock and R.C. Newman, "Dependence of the critical pitting temperature on surface roughness", *Corrosion Science*, Vol. 45, 2003, pp. 1203-1216.
- [4] M. Shafiei and A. T. Alpas, "Nanocrystalline nickel films with lotus leaf texture for superhydrophobic and low friction surfaces", *Applied Surface Science* Vol. 256, 2009, pp. 710-719.
- [5] W. Barthlott and C. Neinhuis, "Purity of the sacred lotus, or escape from contamination in biological surfaces", *Planta*, Vol. 202, 1997, pp. 1-8.
- [6] S.J. Lee, C.H. Huang, J.J. Lai and Y.P. Chen, "Corrosion-resistant component for PEM fuel cells", *Journal of Power Sources*, Vol. 131, 2004, pp. 162-168.
- [7] T. Liu, Y. Yin and L. Dong, "New application of the underwater superhydrophobic surface in the corrosion protection", *Advanced Materials Research*, Vols. 79-82, 2009, PP 1115-1118.
- [8] S. M. Lee, D. J. Oh, I. D. Jung, K. M. Bae, P. G. Jung, K. H. Chung, Seung-J. Cho and J. S. Ko, "Fabrication of nickel micromesh sheets and evaluation of their water-repellent and waterproof abilities", *International Journal of Precision Engineering and Manufacturing*, Vol. 10, No. 3, 2009, pp. 161-166.
- [9] J. T. Han, Y. Jang, D. Y. Lee, J. H. Park, S. H. Song, D. Y. Banb and K. Cho, "Fabrication of a bionic superhydrophobic metal surface by sulfur-induced morphological development", *Journal of Materials Chemistry*, Vol. 15, 2005, pp. 3089-3092.
- [10] M. Jin, X. Feng, J. Xi, J. Zhai, K. Cho, L. Feng and L. Jiang, "Super-Hydrophobic PDMS Surface with Ultra-Low Adhesive Force", *Macromolecular Rapid communications*, Vol. 26, 2005, pp. 1805-1809.
- [11] I. A. Larmour, G. C. Saunders and S. E. J. Bell, "Assessment of roughness and chemical modification in determining the hydrophobic properties of metals", *New Journal of Chemistry*, Vol. 32, 2008, pp. 1215-1220.

- [12] B. Wu, M. Zhou, J. Li, X. Ye, G. Li and L. Cai, "Superhydrophobic surfaces fabricated by microstructuring of stainless steel using a femtosecond laser", *Applied Surface Science*, Vol. 256, 2009, pp. 61–66.
- [13] T. Liu, S. Chen, S. Cheng, J. Tian, X. Chang, Y. Yin, "Corrosion behavior of super-hydrophobic surface on copper in seawater", *Electrochimica Acta*, Vol. 52, 2007, pp. 8003–8007.
- [14] T. Liu, Y. Yin, S. Chen, X. Chang, S. Cheng, "Super-hydrophobic surfaces improve corrosion resistance of copper in seawater", *Electrochimica Acta*, Vol. 52, 2007, pp. 3709–3713.
- [15] P. M. Barkhudarov, P. B. Shah, E. B. Watkins, D. A. Doshi, C. J. Brinker and J. Majewski, "Corrosion inhibition using superhydrophobic films", *Corrosion Science*, Vol. 50, 2008, pp. 897–902.
- [16] T. Liu, Y. Yin, L. Li, "Inhibition microbial adherence of superhydrophobic surface on aluminum in seawater", *Advanced Materilas Research*, Vols. 79-82, 2009, pp 1123-1126.
- [17] Y. Yin, T. Liu, S. Chen, T. Liu and S. Cheng, "Structure stability and corrosion inhibition of super-hydrophobic film on aluminum in seawater", *Applied Surface Science*, Vol. 255, 2008, pp. 2978–2984.
- [18] T. He, Y. Wang, Y. Zhang, Q. lv, T. Xu and T. Liu, "Super-hydrophobic surface treatment as corrosion protection for aluminum in seawater", *Corrosion Science*, Vol. 51, 2009, pp. 1757–1761.
- [19] M. Zhou, H.F. Yang, B.J. Li, J. Dai, J.K. Di, E.L. Zhao and L. Cai, "Forming mechanisms and wettability of double-scale structures fabricated by femtosecond laser", *Applied Physics A*, Vol. 94, 2009, pp. 571–576.
- [20] W. K. Cho, S. Park, S. Jon and I. S. Choi, "Water-repellent coating: formation of polymeric self-assembled monolayers on nanostructured surfaces", *Nanotechnology*, Vol. 18, No. 395602, 2007, pp. 1-7.
- [21] L. Zhu and Y. Jin, "A novel method to fabricate water-soluble hydrophobic agent and super-hydrophobic film on pretreated metals", *Applied Surface Science*, Vol. 253, 2007, pp. 3432–3439.
- [22] A. Tuteja, W. Choi, G. H. McKinley, R. E. Cohen, and M. F. Rubner, "Design parameters for superhydrophobicity and superoleophobicity", *MRS Bulletin*, Vol. 33, 2008, pp 752-758.

- [23] A. Tuteja, W. Choi, M. Ma, J. M. Mabry, S. A. Mazzella, G. C. Rutledge, G. H. McKinley, R. E. Cohen, "Designing superoleophobic surfaces", *Science*, Vol. 318, 2007, pp 1678-1622.
- [24] A. Shahryari, W. Kamal and S. Omanovic, "The effect of surface roughness on the efficiency of the cyclic potentiodynamic passivation (CPP) method in the improvement of general and pitting corrosion resistance of 316LVM stainless steel", *Materials Letters*, Vol. 62, 2008, pp. 3906–3909.
- [25] Y.X. Qiao, Y.G. Zheng, P.C. Okafor and W. Ke, "Electrochemical behaviour of high nitrogen bearing stainless steel in acidic chloride solution: Effects of oxygen, acid concentration and surface roughness", *Electrochimica Acta*, Vol. 54 2009, pp. 2298–2304.
- [26] S. Girija, U. K. Mudali, R.K. Dayal, B. Raj, "Surface protection of type 316LN in neutral chloride solution", *Materials Performance*, Vol. 48, No. 1, 2009, pp. 70-74.
- [27] S. M. Maeng, L. Axe, T. A. Tyson, L. Gladczuk and M. Sosnowski, "Corrosion behavior of magnetron sputtered α -Ta coatings on smooth and rough steel substrates", *Surface & Coatings Technology*, Vol. 200, 2006, pp. 5717–5724.
- [28] L. Bjornkist and I. Olefjord, "The electrochemistry of chromium in acidic chloride solutions: Anodic dissolution and passivation ", *Corrosion Science*, Vol. 32, 1991, pp. 231-242.
- [29] E. C. Elik , A.S. Demirkıran and E. Avci, "Effect of grit blasting of substrate on the corrosion behaviour of plasma-sprayed Al_2O_3 coatings", *Surface and Coatings Technology*, Vol. 16–119,1999, pp. 1061–1064.
- [30] G. T. Burstein and S. P. Vines, "Repetitive nucleation of corrosion pits on stainless steel and the effects of surface roughness", *Journal of The Electrochemical Society*, Vol. 148, No. 12, 2001, pp. B504-B516.
- [31] P. B. Srinivasan, J. Liang, C. Blawert, M. Stormer and W. Dietzel, "Effect of current density on the microstructure and corrosion behaviour of plasma electrolytic oxidation treated AM50 magnesium alloy", *Applied Surface Science*, Vol. 255, 2009, pp. 4212–4218.
- [32] A. Bai, "Optimization of anti-corrosion ability of micro-arc oxide coating on AZ91D alloy using experimental strategies", *Surface & Coatings Technology*, Vol. 204, 2010, pp. 1856–1862.

- [33] C. L. Chang, J. H. Chen, P. C. Tsai, W. Y. Ho and D. Y. Wang, "Synthesis and characterization of nano-composite Ti–Si–N hard coating by filtered cathodic arc deposition", *Surface & Coatings Technology*, Vol. 203, 2008, pp. 619–623.
- [34] A. Gajewski, "Contact angle and sessile drop diameter hysteresis on metal surfaces", *International Journal of Heat and Mass Transfer*, Vol. 51, 2008, pp. 4628–4636.
- [35] Y. T. Cheng, D. E. Rodak, C. A. Wong and C. A. Hayden, "Effects of micro- and nano-structures on the self-cleaning behaviour of lotus leaves", *Nanotechnology*, Vol. 17, 2006, pp. 1359–1362.
- [36] T. Liu, K. T. Lau, S. Chen, S. Cheng, Y. Yin, "Super-hydrophobic surfaces improve corrosion resistance of Fe₃Al-type intermetallic in seawater", *Advanced Materials Research*, Vols. 47-50, 2008, pp 173-176.
- [37] R. Wang and M. Kido, "Using atomic force microscope to observe nano-size water droplets on several materials surfaces and evaluate their wettabilities", *Science, Technology and Education of Microscopy*, pp. 10-16.
- [38] O. Kurtz, J. Barthelmes, F. L. Broc, T. Bilkay, M. Danker and R. Ruther, "Gold post-dip to improve corrosion-resistance properties", *Metalfinishing I*, 2009, pp. 24-30.
- [39] B. Shi, T. B. Kuhn, H. Liang and L. K. Duffy, "Tribochemical performance of cell-treated nickel matrix", *American Journal of Biotechnology and Biochemistry* 3, Vol. 3, 2007, pp 141-144.
- [40] Q. Pan, H. Jin, H. Wang, "Fabrication of superhydrophobic surfaces on interconnected Cu(OH)₂ nanowires via solution-immersion", *Nanotechnology*, Vol. 18, No. 355605, 2007, pp. 1-4.
- [41] W. Xi, Z. Qiao, C. Zhu, A. Jia and M. Li, "The preparation of lotus-like superhydrophobic copper surfaces by electroplating", *Applied Surface Science*, Vol. 255, 2009, pp. 4836–4839.
- [42] H. Zhu, S. Chen, Y. Chen, Z. Zhu and Y. Yin, "Investigation of the corrosion resistance of n-tetradecanoic acid and its hybrid film with bis-silane on copper surface in seawater", *Journal of Molecular Structure*, Vol. 928, 2009, pp. 40–45.
- [43] X. Wu and G. Shi, "Fabrication of a lotus-like micro–nanoscale binary structured surface and wettability modulation from superhydrophilic to superhydrophobic", *Nanotechnology*, Vol. 16, 2005, pp. 2056–2060.
- [44] W. Li, L. Zhu and H. Liu, "Preparation of hydrophobic anodic film on AZ91D magnesium alloy in silicate solution containing silica sol", *Surface & Coatings Technology*, Vol. 201, 2006, pp. 2573–2577.

- [45] R.D. Narhe, W. G. Viñnas and D.A. Beysens, "Water condensation on zinc surfaces treated by chemical bath deposition", *Applied Surface Science*, Vol. 256, 2010, pp. 4930–4933.
- [46] D. M. Spori, T. Drobek, S. Zürcher, M. Ochsner, C. Sprecher, A. Mühlebach and N. D. Spencer, "Beyond the Lotus Effect: Roughness Influences on Wetting over a Wide Surface-Energy Range", *Langmuir*, Vol. 24, 2008, pp. 5411-5417.
- [47] L. Y. L. Wu, A.M. Soutar and X.T. Zeng, "Increasing hydrophobicity of sol-gel hard coatings by chemical and morphological modifications", *Surface & Coatings Technology*, Vol. 198, 2005, pp. 420– 424.
- [48] G. X. Shen, R. G. Du, Y. C. Chen, C.J. Lin and D. Scantlebury, "Study on hydrophobic nano-titanium dioxide coatings for improvement in corrosion resistance of type 316L stainless steel", *Corrosion*, Vol. 61, 2005, pp 943-950.
- [49] M. Duarte, A. Lasagni, R. Giovanelli, J. Narciso, E. Louis and F. Mücklich, "Increasing lubricant film lifetime by grooving periodical patterns using laser interference metallurgy", *Advanced Engineering Materials*, Vol. 10, No. 6, 2008, pp. 554-558.
- [50] A. Lasagni, M. D'Alessandria, R. Giovanelli and F. Mücklich, "Advanced design of periodical architectures in bulk metals by means of laser interference metallurgy", *Applied Surface Science*, Vol. 254, 2007, pp. 930–936.
- [51] I. Yadroitsev, I. Shishkovsky, P. Bertrand, I. Smurov, "Manufacturing of fine-structured 3D porous filter elements by selective laser melting", *Applied Surface Science*, Vol. 255, 2009, pp. 5523–5527.
- [52] G. Dumitru, V. Romano, H.P. Weber, H. Haefke, Y. Gerbig and E. Pflüger, "Laser microstructuring of steel surfaces for tribological applications", *Applied Physics*, Vol. A 70, 2000, pp. 485–487.
- [53] P. G. Engleman, A. Kurella, A. Samant, C. A. Blue and N. B. Dahotre, "The application of laser-Induced multi-scale surface texturing", *Journal of Metals (JOM)*, Dec. 2005, pp. 46-50.
- [54] R. Lloyd, A. Abdolvand, M. Schmidt, P. Crouse, D. Whitehead, Z. Liu and L. Li, "Laser-assisted generation of self-assembled microstructures on stainless steel", *Applied Physics A*, Vol. 93, 2008, pp. 117–122.
- [55] cho D. Kim a, W. Hwang, H.C. Park and K.H. Lee, "Superhydrophobic nanostructures based on porous alumina", *Current Applied Physics*, Vol. 8, 2008, pp. 770–773.

[56] <http://web2.uwindsor.ca/wsgcms/Projects/Tribology/facilities.php>, August 12, 2010.

[57] M. G. Fontana and N. D. Greene, "Corrosion engineering", 2nd edition, McGraw Hill, 1978.

[58] D. E. Leyden, "Materials characterizations: X-ray spectroscopy", ASM Handbook, Vol. 10, 3rd edition, 1992, pp 82-101.

[59] G. W. Stachowiak, A. W. Batchelor, "Engineering tribology", 3rd edition, Elsevier, 2005.

[60] Wyko NT1100 software, Tucson, Arizona, 2002.

[61] C.W. Extrand, "Criteria for ultralyophobic surfaces", Langmuir, Vol. 20, 2004, pp 5013-5018.

VITA AUCTORIS

Majid Bigdeli Karimi was born in 1983 in Tehran, Iran. He graduated from Iran University of Science and Technology where he obtained a B.Sc. in Materials Engineering in 2005 and received a M.Sc. degree from Sharif University of Technology in Materials Science and Engineering in 2007. He is currently a candidate for the Master of Applied Science degree in Materials Engineering at the University of Windsor and hopes to graduate in summer 2010.